

DEFNE US

Reduction of Limited Angle Artifacts in Medical Tomography via Image Reconstruction

DEFNE US

Reduction of Limited Angle Artifacts in Medical Tomography via Image Reconstruction

ACADEMIC DISSERTATION

To be presented, with the permission of
the Faculty Council of Information Technology and Communication Sciences
of Tampere University,
for public discussion in the auditorium TB109,
of the Tietotalo building, Korkeakoulunkatu 1, Tampere,
on 08.02.2019, at 12 o'clock.

ACADEMIC DISSERTATION

Tampere University, Faculty of Information Technology and Communication Sciences

<i>Responsible supervisor and Custos</i>	Professor Ulla Ruotsalainen Tampere University Finland	
<i>Supervisor</i>	Associate Professor Sampsa Pursiainen Tampere University Finland	
<i>Pre-examiners</i>	Assistant Professor Nuno Matela Lisbon University Portugal	Associate Professor Martin S. Andersen Technical University of Denmark Denmark
<i>Opponents</i>	Chief Physicist Antti Sohlberg Joint Authority for Päijät-Häme Social and Healthcare Finland	Associate Professor Martin S. Andersen Technical University of Denmark Denmark

The originality of this thesis has been checked using the Turnitin OriginalityCheck service.

Copyright ©2019 Defne Us

Cover design: Roihu Inc.

ISBN 978-952-03-0963-3 (print)
ISBN 978-952-03-0964-0 (pdf)
ISSN 2489-9860 (print)
ISSN 2490-0028 (pdf)
<http://urn.fi/URN:ISBN:978-952-03-0964-0>

PunaMusta Oy
Tampere 2019

Abstract

Artifacts are unwanted effects in tomographic images that do not reflect the nature of the object. Their widespread occurrence makes their reduction and if possible removal an important subject in the development of tomographic image reconstruction algorithms. Limited angle artifacts are caused by the limited angular measurements, constraining the available tomographic information. This thesis focuses on reducing these artifacts via image reconstruction in two cases of incomplete measurements from: (1) the gaps left after the removal of high density objects such as dental fillings, screws and implants in computed tomography (CT) and (2) partial ring scanner configurations in positron emission tomography (PET). In order to include knowledge about the measurement and noise, prior terms were used within the reconstruction methods. Careful consideration was given to the trade-off between image blurring and noise reduction upon reconstruction of low-dose measurements.

Development of reconstruction methods is an incremental process starting with testing on simple phantoms towards more clinically relevant ones by modeling the respective physical processes involved. In this work, phantoms were constructed to ensure that the proposed reconstruction methods addressed to the limited angle problem. The reconstructed images were assessed qualitatively and quantitatively in terms of noise reduction, edge sharpness and contrast recovery.

Maximum *a posteriori* (MAP) estimation with median root prior (MRP) was selected for the reconstruction of limited angle measurements. MAP with MRP successfully reduced the artifacts caused by limited angle data in various datasets, tested with the reconstruction of both list-mode and projection data. In all cases, its performance was found to be superior to conventional reconstruction methods such as total-variation (TV) prior, maximum likelihood expectation maximization (MLEM) and filtered back-projection (FBP). MAP with MRP was also more robust with respect to parameter selection than MAP with TV prior.

This thesis demonstrates the wide-range applicability of MAP with MRP in medical tomography, especially in low-dose imaging. Furthermore, we emphasize the importance of developing and testing reconstruction methods with application-specific phantoms, together with the properties and limitations of the measurements in mind.

To my grandfather, Dr. Necdet Tuna

Preface

This study was carried out during 2013-2018 at Tampere University of Technology (TUT) with the financial support of the graduate school of Tampere University of Technology and Academy of Finland at Laboratories of Signal Processing and Mathematics.

I would like to express my sincere gratitude to Prof. Ulla Ruotsalainen for her guidance and support throughout my work. She has encouraged me to find my research questions and helped me sort the good ideas from the bad. It has been an honor to work by her side for the past 6 years and I am grateful for everything she has taught me both in and out of research. Assoc. Prof. Sampsa Pursiainen has opened me a window to the world of mathematics and its importance in understanding the assumptions we make when using engineering approaches to solve problems. Special thanks to Prof. Peter Dendooven for helping me to tackle real-life questions in my work and do meaningful research by offering his knowledge on the physical and clinical aspects of my research. He has also showed genuine interest in my progress, keeping a close eye for the potential obstacles in my way and offered solutions. I would like to thank my pre-reviewers Assoc. Prof. Martin Andersen and Asst. Prof. Nuno Matela for their valuable feedback on my thesis, whose questions and comments enabled me to create a more coherent narrative. I'm also thankful to my opponents, Chief Physicist Antti Sohlberg and Assoc. Prof. Martin Andersen. I am grateful to Uygur Tuna for introducing me to the Methods and Models for Biological Signals and Images (M2oBSI) group through my masters thesis. My colleagues have contributed with fruitful discussions and much needed coffee breaks. The secretaries and other staff members helped me efficiently navigate through the system.

My family and friends have been the pillars of my life. They have encouraged me with their love throughout my work and helped me to have a life outside of it as well. The distances between us might be long, but our hearts will always stay close.

Tampere, November 2018

Defne Us

Contents

Abstract	i
Preface	v
Contents	vii
Acronyms	x
Nomenclature	xi
List of Publications	xii
Author contribution	xii
1 Introduction	1
1.1 Background	1
1.2 Objectives	2
2 Data Acquisition	4
2.1 Positron emission tomography	4
2.2 Computed tomography	7
2.3 Sources of artifacts	8
3 Image Reconstruction	12
3.1 Analytical reconstruction methods	13
3.2 Iterative reconstruction methods	14
3.3 Use of priors in reconstruction	20
3.4 List-mode data reconstruction	22
4 Evaluation Criteria	24
4.1 Assessing overall image quality	24
4.2 Region of interest analysis	25
4.3 Evaluation of the edges	26
5 Artifact Reduction in CT	27
5.1 Review of previous work	27
5.2 Methods	28
5.3 Dataset preparation	30
5.4 Results	32
5.5 Discussion	34

6	Artifact Reduction in PET: A Scanner Design	37
6.1	Review of previous work	37
6.2	Methods	39
6.3	Experimental setup	40
6.4	Simulation setup	40
6.5	Results	41
6.6	Discussion	41
7	Artifact Reduction in PET: A Reconstruction Method	43
7.1	Review of previous work	43
7.2	Methods	43
7.3	Dataset preparation	44
7.4	Results	45
7.5	Discussion	50
8	Conclusion	52
	Bibliography	54
	Publications	63

Acronyms

1D, 2D, 3D	One, two, three dimensional
ACF	Attenuation correction factor
amMAPEM	Adaptive multiresolution MAPEM
ART	Algebraic reconstruction technique
ASD-POCS	Adaptive-steepest-descent-projection-onto-convex-sets
AX-PET	Axial positron emission tomograph
Bq	Becquerel
CBCT	Cone beam computed tomography
CG	Conjugate gradient
CoV	Coefficient of variation
CRT	Coincidence resolving time
CT	Computed tomography
DOI	Depth of interaction
DT-CWT	Dual-tree complex wavelet transform
ET	Emission tomography
FBP	Filtered backprojection
FOV	Field-of-view
FWHM	Full-width-half-maximum
Gate	Geant4 Application in tomographic reconstruction
HU	Hounsfield units
LOR	Line of response
LS	Least-squares methods
LYSO	Yttrium-doped lutetium oxyorthosilicate
MAP	Maximum <i>a-posteriori</i>
MAPEM	Maximum <i>a-posteriori</i> expectation maximization
MAR	Metal artifact reduction
ML	Maximum likelihood
MLEM	Maximum likelihood expectation maximization
MRI	Magnetic resonance imaging
MRP	Median root prior
MRTV-CG	Multiresolution conjugate gradient with total variation penalty
MSE	Mean squared error
NMI	Normalized mutual information
OSEM	Ordered subsets expectation maximization
OSL	One step late
PEM	Positron emission mammography
PET	Positron emission tomography
ROI	Region of interest
sMAPEM	Sequential MAPEM
SPECT	Single photon emission computed tomography
SSIM	Structural similarity index
TOF	Time of flight
TV	Total variation
WLS	Wavelength shifter

Nomenclature

a_{ij}	System matrix or projection operator
\mathbf{A}	2D matrix containing all a_{ij}
\mathbf{A}^+	Moore-Penrose approximation for inverse of \mathbf{A}
\mathbf{A}^T	Transpose of \mathbf{A}
b	Slope of the sigmoid fit
β	Penalty weight in iterative reconstruction
c	Speed of light
\mathbf{D}	Derivative of the total variation norm
Δd	Distance between center of FOV and the annihilation location
$E(\cdot)$	Expectation
e	Residual error
Γ_ℓ	Weighting matrix for LS solution
$H(a)$	Shannon entropy of image a
h_0	The 50% location of the sigmoid fit
I	Number of measurements/projections
I_{in}	Initial beam intensity in CT
I_{out}	Measured beam intensity in CT
J	Number of bins in the image
$L(\mathbf{x})$	Log-posterior probability function
M_j	Median filtered image
μ	Attenuation coefficient in X-ray CT
μ_{ROI}	Mean intensity value within a region-of-interest
η	Additive noise term
p_i	Projection at location i
\mathbf{p}	Projection vector consisting of all p_i s
$\hat{\mathbf{p}}$	Estimated projection vector
$P(x)$	Probability distribution of x
s	Distance of an event from the scanner center, axis parallel to detectors
σ_{ROI}	Standard deviation of intensity values within a region-of-interest
θ	Angle of the LOR with the scanner center
t	Axis perpendicular to the detector
t_1, t_2	Arrival times of pair of annihilation photons at the detectors
$U(x)$	Prior term in MAP
\mathbf{W}	Weight of the LS solution
\mathbf{x}_j^k	Spatial domain image at k^{th} iteration
\mathbf{x}	Image vector consisting of all x_i s
$\hat{\mathbf{x}}$	The estimate of image \mathbf{x}
x, y, z	Cartesian coordinates

List of Publications

- I U. Tuna*, D. Us*, U. Ruotsalainen, "Metal Artifact Reduction Based on Multi-Level Sinogram Segmentation and Sequentially Applied MAP-EM Reconstruction Method," *2013 IEEE Nuclear Science Symposium and Medical Imaging Conference Record (NSS/MIC)*, pp. 3412–3414 Nov. 2013, Seoul, South Korea (*equal contribution).
- II D. Us, A. Moreno-Galera, S. Nazari-Farsani, K. Palovuori, H. Kosola, T. Zedda, U. Ruotsalainen, "AvanTomography: A Compact Module for Positron Emission Mammography," *IEEE International Symposium on Medical Measurements and Applications, MeMeA 2015 - Proceedings*, pp. 52–57, May 2015, Turin, Italy.
- III D. Us, E. Acar, U. Ruotsalainen, "Metal Artifact Reduction Based on Automated Sinogram Segmentation and Adaptive Multiresolution MAP Reconstruction Method," *2015 IEEE Nuclear Science Symposium and Medical Imaging Conference Record (NSS/MIC)*, pp. 1–5, Nov 2015, San Diego, USA.
- IV D. Us, K. Brzezinski, T. Buitenhuis, P. Dendooven, U. Ruotsalainen, "Evaluation of median root prior for robust in-beam PET reconstruction," *IEEE Transactions on Radiation and Plasma Medical Sciences*, vol. 2, no. 5, pp. 1–9, 2018.
- V D. Us, U. Ruotsalainen, S. Pursiainen, "Combining Dual-Tree Complex Wavelets and Multiresolution in Iterative CBCT reconstruction with Application to Metal Artifact Reduction," *submitted to BMC Biomedical Engineering Online*, July 2018.

Author contribution

In this thesis, previously unpublished results are presented as an extension of the work in P II. These results include the reconstruction of the Monte Carlo simulation of the same setup with a simple phantom, which was carried out under the supervision of the author. For a fair comparison of reconstruction methods suggested for reduction of metal artifacts in P I, P III and P V, the same jaw phantom was used for all reconstruction methods and the quantitative results are presented according to these reconstructions.

- I U. Tuna*, D. Us*, U. Ruotsalainen, "Metal Artifact Reduction Based on Multi-Level Sinogram Segmentation and Sequentially Applied MAP-EM Reconstruction Method," *2013 IEEE Nuclear Science Symposium and Medical Imaging Conference Record (NSS/MIC)*, pp. 3412–3414, Nov. 2013, Seoul, South Korea (*equal contribution).

The author developed the segmentation method and the jaw phantom used in this work. The reconstruction work with sMAPEM was carried out by U. Tuna.

- II D. Us, A. Moreno-Galera, S. Nazari-Farsani, K. Palovuori, H. Kosola, T. Zedda, U. Ruotsalainen, "AvanTomography: A Compact Module for Positron Emission Mammography," *IEEE International Symposium on Medical Measurements and Applications, MeMeA 2015 - Proceedings*, pp. 52–57, May 2015, Turin, Italy.

As the main responsible, the author designed the study and wrote the article. She supervised the work and took part in the measurements.

- III D. Us, E. Acar, U. Ruotsalainen, "Metal Artifact Reduction Based on Automated Sinogram Segmentation and Adaptive Multiresolution MAP Reconstruction Method," *2015 IEEE Nuclear Science Symposium and Medical Imaging Conference Record (NSS/MIC)*, pp. 1–5, Nov 2015, San Diego, USA.

The author developed the segmentation method and the phantoms used in the paper. The reconstruction of data was carried out by E. Acar. The evaluation and presentation of the results were done by the author as well as writing the manuscript.

- IV D. Us, K. Brzezinski, T. Buitenhuis, P. Dendooven, U. Ruotsalainen, "Evaluation of median root prior for robust in-beam PET reconstruction," *IEEE Transactions on Radiation and Plasma Medical Sciences*, vol. 2, no. 5, pp. 1–9, 2018.

The author developed the reconstruction method, designed and conducted the simulations for the simple phantom, and wrote the manuscript. The data for the realistic patient treatment was provided by P. Dendooven and his colleagues from University of Groningen, which were then reconstructed and evaluated by the author.

- V D. Us, U. Ruotsalainen, S. Pursiainen, "Combining Dual-Tree Complex Wavelets and Multiresolution in Iterative CBCT reconstruction with Application to Metal Artifact Reduction," *submitted to BMC Biomedical Engineering Online*, July 2018.

The author was responsible for the preparation of the dataset with polychromatic spectrum, as well as the adaptation of the reconstruction method into the field of dental CT and the incorporation of the filtering in the wavelet domain via complex dual wavelet transform. The paper structure and the design of the experiments were prepared in collaboration with S. Pursiainen.

1 Introduction

1.1 Background

Medical devices in the field of radiation imaging utilize the interaction between radiation and the body to non-invasively visualize structures and processes inside an organism. Radiation imaging can be seen as a combination of three main components [1]:

Source of radiation is introduced to an object to measure a certain property. If the measured radiation is transmitted by an external source through the object, it is called transmission imaging (Figure 1.1a). X-ray computed tomography (CT), angiography and radiography are some examples of imaging modalities that utilize transmission of radiation. If radiation is emitted from within the object during measurement, the imaging method is called emission imaging (Figure 1.1b). Positron emission tomography (PET) and single photon emission computed tomography (SPECT) are examples of modalities that use emission of radiation. A third possibility is that the radiation source outside the object transmits the radiation to the object and the scattered radiation is measured, then it is referred as scatter imaging (Figure 1.1c).

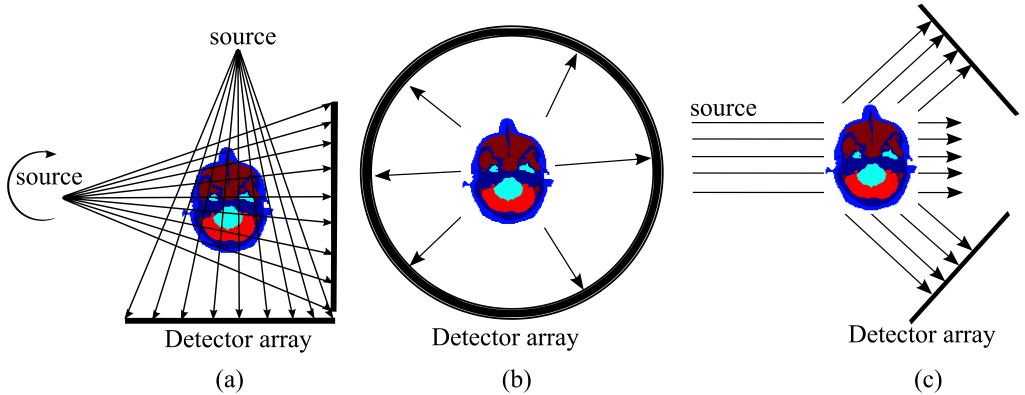


Figure 1.1: Tomographic imaging methods. (a) Transmission tomography, (b) Emission tomography, (c) Scatter tomography.

Transport of radiation from the source to the object defines the physical interaction between the radiation and the object. The result of this interaction produces the information about the object. The transport process is not discussed in the context of this thesis. **Detectors** record the intensity of radiation that leaves the object and reaches designated locations [1]. They convert the energy of the stopped photons into an electrical signal or charge. The detector system is specific to the radiation source and transport.

The level of efficiency of a detector determines how much of the radiation that reaches the detector, is stopped and recorded. The detector systems for different sources of radiation are briefly described in this work.

This thesis focuses on the characterization of imaging methods based on their source of radiation, specifically tomographic data obtained from transmission and emission of radiation. Transmission tomography measures the attenuation of radiation, which originates from an external source outside the patient, and provides slice-by-slice information on anatomical structures. The radiation source (X-rays, neutrons or gamma rays) penetrates through the object and the rays are attenuated according to the tissue density along their trajectories. The attenuated radiation from the transmission is measured and information about the structural density inside the object is calculated by comparing the radiation intensity at the source and at the detector. CT uses X-rays as the source of radiation, which is rotated around the object to obtain multiple views from different angles for tomographic imaging. Details on the physics and properties of CT are explained further in Chapter 2.2.

Emission tomography (ET), also called nuclear imaging, maps the distribution of emitted radiation, creating a functional image of the biochemical process within the body. In ET, molecules are labeled with radioactive molecules with short half-lives, which are injected into the bloodstream of the patient. The molecules are metabolized in the body and the scanner measures the metabolization of the radioactive labeled molecules in the body. In PET, when an unstable positron from the radioactive label interacts with a nearby electron, both positron and electron are annihilated, emitting a pair of high energy (511 keV) photons. The photons from the annihilation travel in opposite directions along a straight line and hit the detectors in the scanner, creating the physical basis of ET measurements. PET is a commonly used ET modality in cancer detection where the consumption of radioactive labeled sugar by a tumor is measured. Other application areas of PET include cardiac imaging, blood flow and volume imaging, neurochemistry and radiation therapy [2, 3]. Tomographic data in PET is obtained by a ring of detectors around the patient. Some of the most common positron emitters (radioactive labels) used in PET include ^{15}O , ^{18}O , ^{13}N , ^{11}C and ^{18}F .

Measurement from a single angle in tomographic imaging is called a projection. Projections acquired from multiple angles need to be transformed into anatomically relevant images via image reconstruction. New reconstruction methods are constantly proposed or existing ones are improved in the direction of the developments in medical imaging.

1.2 Objectives

This thesis investigates methods for (1) tomographic imaging with low-dose radiation, (2) reconstruction of data from multimodality imaging, and (3) reduction of artifacts upon reconstruction of incomplete data.

1. Demand for lower radiation doses in medical imaging has increased as the effects of radiation on the human body are explored further. The generic noise reduction algorithms that are developed for high-dose imaging can result in distortion or blurring of the anatomical borders in low-dose settings. One way to prevent this distortion is to incorporate our knowledge on noise and data into the reconstruction via prior functions to reduce the noise without leading to erroneous estimation of image borders. However, the heavy penalization needed for reduction of noise often blurs of the edges

of the structures in the images, making the selection of the prior function an important component of reconstruction. That is why P I, P III, P IV and P V study various ways and functions to incorporate a priori information into the image reconstruction. In ET, it is also possible to reduce the noise by increasing the sensitivity of the scanner, which is examined in P II. P I – P V study the effects of noise on projection data and propose methods for its reduction.

2. Multimodality or fusion imaging refers to the combination of different imaging modalities to obtain more information about the human body. For instance, fusion of CT and PET complements the structural information from CT with information on the biochemical processes from PET, leading to a more complete picture of the disease for better diagnostics [4]. Information from one modality can also be used to compensate for the disadvantages of another. For example, the high image quality of CT improves the low spatial resolution of a PET image. CT is also used for attenuation correction of PET images. Another example of multimodality imaging is the use of PET for the imaging of secondary radiation in proton therapy to ensure the delivery of the proton beam to the correct location. Such multimodality alternatives bring up new challenges for hardware designs as well as the reconstruction methods. The reconstruction of PET data obtained from proton therapy constitutes a challenge for image reconstruction due to its very low count rate and the use of scanners with limited angular coverage. P IV is focused on reconstruction of low-count PET data to monitor the treatment area in proton therapy.
3. Artifacts are undesired effects on medical images and they can be related to noise, limitations of the system design or the measurement protocol. They prevent the correct interpretation of the acquired measurements. Limited angle measurements are one of the causes of such artifacts. They can cause elongation of the object or create streak-type artifacts when the reconstruction methods cannot handle incomplete data. Although artifact reduction methods have been around for a long time for high activity/dose images in PET and CT, reconstruction methods for low dose measurements have only become popular in the past decade (a collection of recent research on low-dose CT and PET reconstruction can be found in [5] and [6], respectively). This is partly because the low radiation dose protocols are still relatively new in imaging. Another reason is the noisy images produced from low dose imaging add another level of difficulty in the development of algorithms [6]. The reduction of limited angle artifacts is covered in P I – P V.

This thesis addresses the abovementioned issues by proposing various methods to reduce noise and remove artifacts in the reconstructed images, providing more accurate images from low dose/activity CT and PET measurements. More specifically, P I, P III and P V propose penalized reconstruction methods for reducing the artifacts caused by high density objects in low dose CT. For PET, limited angle artifacts are tackled by improving the sensitivity of the scanner (P II) and implementing a penalized reconstruction method (P IV).

2 Data Acquisition

2.1 Positron emission tomography

PET measures pairs of photons emitted from a subject. Each photon in the pair travels in opposite direction and is stopped approximately at the same time (nanoseconds apart) by detectors at opposite sides of a PET scanner. A detected pair of photons is called an event. Events in PET fall into one of 4 categories: (1) True coincidences, (2) Random coincidences (randoms), (3) Scattered coincidences and (4) Multiple coincidences. All event types are depicted in Figure 2.1.

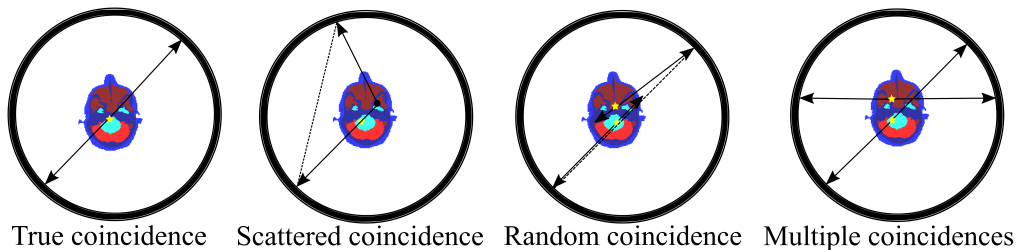


Figure 2.1: Coincidence event types in PET. The dashed lines represent the events recorded by the detector array.

Most PET scanners are designed in the form of ring(s) consisting crystal blocks, which are very dense materials capable of stopping the photons emitted from an object. The crystal blocks are coupled with detectors that convert the energy of the stopped photon into electrical signals to be sent to a computer. The linear trajectory of an event, called a line-of-response (LOR), is traced and the point of interaction is calculated to estimate the emission point of the photons.

When a photon hits a crystal and is detected by the detector array, attributes such as the coordinates of the hit, exact energy of the photon and its arrival time can be recorded. One can record such properties for each event into a matrix, in which each detector pair is represented with a bin. There are as many bins as the number of possible detector pairs. The storage of events in bins is called histogramming and is commonly used in tomographic imaging to store the acquired data. Let the measurement be represented in histogram domain as $p(s, \theta)$, where s is the distance of an event from the scanner center and θ is the angle of the line that connects the location of the event to the center of the scanner. The location of an event with x and y coordinates, $f(x, y)$ is mapped onto a measurement bin, $p(s, \theta)$, as follows:

$$s = x\cos(\theta) + y\sin(\theta), t = -x\sin(\theta) + y\cos(\theta), \quad (2.1)$$

where s is on an axis parallel to the detector array and t is the axis orthogonal to it. The interpretation of an object's image into a set of line integrals is called Radon transform [7]. In PET, line integrals are obtained by summing the events along the line into a bin in the projection domain. The angle θ of each LOR makes it possible to collect the LORs with the same angle into 2D matrices called sinograms. In a sinogram, one dimension represents the angle of the LOR and bins of the second dimension represents a detector pair positioned at a certain angle. All the counts detected by a detector pair are collected into the same bin in the sinogram. This approach simplifies the data storage and processing. However, the low photon density in PET often means that most of the detector bins are empty, creating an inefficient way of data storage with multiple empty bins in the matrix. The binning of the events can also cause loss of spatial resolution as the bin size is often larger than the width of the LOR.

Another way to store data without compromising the acquisition accuracy is to collect features of each event in a list. Considering that the number of measured events in PET is around 20-50 million stored within 75-200 million bins, storing data in a list rather than in a matrix is more efficient [8]. It is also more accurate as no event is binned together [9]. Additionally, if the PET scanner is capable of recording arrival times of individual photons in a photon pair, this information can also be easily stored in the list-mode format.

2.1.1 Performance measures in PET

Parameters used during evaluation of PET scanner performance are highlighted here, as they are important for the interpretation of the results in P II.

Spatial resolution determines the minimum object size that can be detected by a PET system. To measure the spatial resolution, generally two point or line sources are placed next to each other. The distance at which the two sources are indistinguishable gives the spatial resolution. As the details of x - y coordinate are more important than z direction, the sampling rate is higher in transaxial (x - y) plane than it is in the axial (z) direction. Due to crystal orientation and variations in data sampling in different planes, transaxial and axial spatial resolutions are usually given separately for each system. The unit of spatial resolution is often in full-width-half-maximum (FWHM), which is related to the standard deviation of the Gaussian curve fitted around the source image.

Energy resolution is the system's ability to distinguish photons with different energies. In PET, the photons with 511 keV have a clearly defined peak on the energy spectrum, as well as smaller peaks indicating any internal radiation coming from the crystals. It is important for the PET scanners to have a distinct 511 keV peak, which does not overlap with the Compton peak formed by scattered events. Upon construction of the scanner, a one-time calibration is needed to have the same energy resolution at individual outputs from the photodetectors to correct for differences in electronics and detector nonlinearities. To do so, a measurement without any radioactivity is conducted to determine the level of intrinsic radioactivity of the crystals. Then, an experiment with a point source is conducted and the energy peaks are determined with Gaussian fits over the peaks on the charge spectrum. Mean charge values derived from the Gaussian fits in charge spectra of intrinsic radioactivity measurements of crystals and 511 keV measurements are then translated into their corresponding energy peak values and used for calibration of each detector channel.

Sensitivity of a PET scanner is measured through the percentage of emitted photons

detected by the scanner. In a PET scanner, the crystal orientation results in a trade-off between sensitivity and spatial resolution. Crystals with smaller cross-sections provide better spatial resolution but a decrease in cross section usually means less crystal mass. This translates into less stopping power for the emitted photons, resulting in lower sensitivity. Longer crystals with small cross sections don't solve the problem because it becomes more difficult and erroneous to determine the exact 3D location of the stopped photon within the crystal. Placing the PET scanner as close to the subject as possible can improve the sensitivity. This is partially because of the inverse-square law, which dictates that a physical intensity is proportional to the distance to the source of that intensity, and partially because less counts escape detection.

Time resolution is determined by the ability of the PET detectors in efficient differentiation of the arrival of two subsequent photon events. The time resolution depends on the decay time of the scintillation in the crystals and the processing time of the detectors and their associated electronics. It is measured between two detectors and reported as FWHM of the time difference between the arrivals of two photons emitted from the same event. The conventional PET systems achieve time resolution of 2 to 10 ns, meaning that any photon reaching detectors within that time window will be accepted to be from the same event [10].

Time-of-flight (TOF) information is based on the difference in arrival times of two photons from a single annihilation event. If the positron-electron interaction would happen at the center of the scanner, both photons would arrive at the contra-positioned detectors at the same time. This is seldom the case as the events often does not occur in the center of the scanner. An example of off-centered events is shown in Figure 2.2. The ability to measure time difference within picoseconds has become possible in the recent years thanks to the developments in photodetector and crystal technologies. The TOF is calculated according to the coincidence resolving time (CRT) of a PET system using the formula

$$\Delta d = \frac{t_1 - t_2}{2c}, \quad (2.2)$$

where Δd is the distance between the center of the scanner and the annihilation point, t_1 and t_2 are the arrival times of photons to the detectors, and c is the speed of light (See Figure 2.2a). For instance, a CRT of 400 ps results in a LOR length of 6 cm, whereas 200 ps CRT gives a 3 cm-long LOR. Considering that an average PET scanner for humans has a field-of-view (FOV) of 80 cm, the annihilation localization becomes more accurate with such timing information. Thanks to TOF information, it is now possible to achieve 500-700 ps timing resolution compared to 2-10 ns without TOF in commercial PET scanners [10]. The LORs are convolved with a 1D Gaussian curve to get a probability distribution around the annihilation point, which is depicted in Figure 2.2c.

2.1.2 Data corrections in PET

Attenuation correction is needed in PET because photons are attenuated within the object when they travel towards the detectors. The longer a photon travels within the object, the more it loses its energy. In the human body, the attenuation factor for a certain tissue can be calculated analytically, or more accurately, via CT values [1]. The reciprocal of the attenuation factor is multiplied with its corresponding LOR for correcting the effect of attenuation.

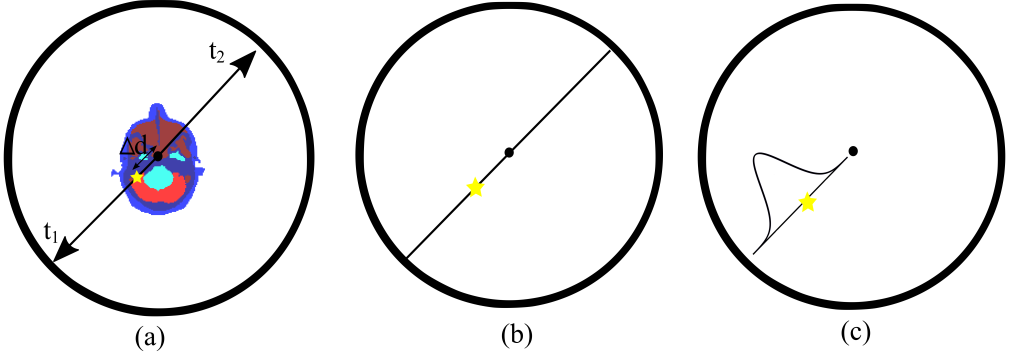


Figure 2.2: With TOF information, the time difference between arrival of two photons is used to determine the location of annihilation more precisely. (a) The arrival times, t_1 and t_2 , and the distance between the assumed and real annihilation points, Δd . (b) Without TOF, each point on the LOR has the same weight. (c) With TOF, each bin is weighted according to its proximity to the point of annihilation. Modified from [4].

Normalization refers to the compensation of various object- and scanner-dependent parameters. Most important one is the correction of sensitivity, which is highest at the center of the FOV along the axial direction, and it decreases towards the peripheries of the scanner. The coefficients for normalization can be calculated by generating sensitivity images analytically or with Monte Carlo simulations. As the sensitivity images follow the Poisson distribution of the measurement, it can be considered as a multiplicative correction term for the data. Other factors in normalization are the compensation of individual detector efficiencies, which is needed to obtain a uniform detection performance from the detectors, and spatial distortion [11].

Randoms and scatter correction are additive correction factors for scattered and random coincidences. As the size of the object increases, more photons are scattered. The scatter fraction can be up to 50 % of the total detected counts in 3D PET imaging and needs to be corrected for accurate reconstruction of measurements [12]. The number of random coincidences is proportional to the level of radioactivity of the source. Therefore, for low activity PET images, random coincidences may be ignored.

2.2 Computed tomography

In CT, a source transmits X-rays through the patient to produce a cross-sectional image of the body. Although X-rays can penetrate into the body, they lose intensity as they travel through it. The measured intensity I_{out} , and the initial intensity of a ray, I_{in} , are related with

$$I_{out} = I_{in} \cdot \exp\left(-\int_{s_0}^{s_1} \mu(s) ds\right), \quad (2.3)$$

where s is the ray traveling from s_0 to s_1 , and the attenuation coefficient is denoted with μ [13]. Higher density materials like bone, enamel or metal attenuate the rays more, therefore they have larger μ values. If l_{AC} is the line integral of the linear attenuation

coefficients along the ray's path (exponential term in Eq. (2.3)), then the attenuation coefficients can be calculated via Beer's law:

$$l_{AC} = \ln\left(\frac{I_{in}}{I_{out}}\right). \quad (2.4)$$

The map of attenuation coefficients leads to the CT image. The coordinates of the path connecting the X-ray source to the detector provide the 2D location of the beam in CT. However, the depth information (z coordinate) cannot be obtained solely from this line because the information acquired by the detector is a superimposition of all attenuation effects along the path of the beam. To determine the depth of the event, detectors are moved to a different position. The combination of information from several angles help constructing the depth of the event. At least 180 degrees need to be covered to obtain a reliable position. The X-ray source, or sometimes the subject, is rotated to acquire data from several angles. In the sinogram of CT, angles correspond to the position of the scanner and the rays detected at that angle are stored inside the bins at the corresponding angle. In the context of CT, values of $p(s, \theta)$ refer to the X-ray intensities at the detector at an angle θ . For a parallel beam CT, the trigonometric relationship between coordinate systems of (s, θ) and (x, y) is the same as in PET (see Eq (2.1)).

CT scanners can have different shapes of X-ray sources such as helical, fan-shaped, cone-shaped or parallel-shaped sources, depending on the model and generation of the CT. Cone beam CT (CBCT) is a newer type of CT, first commercially built in 1997, which uses a cone beam structure instead of the fan-beam type source of CT. Figure 2.3 shows the difference between beams of an earlier fan-beam CT model and CBCT. CBCT scanners have smaller FOVs, resulting in higher spatial resolution compared to CT scanners. There are multiple parameters that determine the radiation dose delivered by CBCT such as the energy and current of the beam, beam type, beam filtration parameters, and number of views or rotations [14]. However, generally a smaller FOV translates into lower radiation dose to the patient [15]. That is why they are regularly used for dental imaging before, during and after surgeries [14].

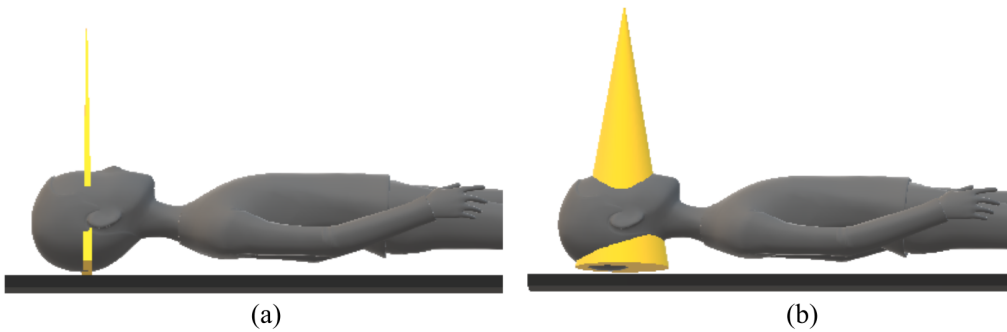


Figure 2.3: Beam structures of (a) fan-beam CT and (b) cone-beam CT

2.3 Sources of artifacts

In medical images, unlike photography, it is not possible to compare the results with the true structures of the object. If the image is distorted for any reason, it can hinder the interpretation of the medical images. There are multiple sources of artifacts

for different imaging modalities, but in general the causes are either physical (beam hardening, motion, noise, scatter, limited angle imaging) or mathematical (assumptions made on the measurement, reconstruction or prior models). In tomographic imaging, some of the common sources of artifacts are noise in the measurements, patient motion, missing projections due to the scanner geometry (partial ring, detector gaps), errors in mathematical modeling of the measurement system, and failure to correct for scattered or random events. In the context of this thesis, we will focus on the artifacts caused by incomplete data with high noise, created in dental CT by the gaps left in the place of high density materials after their extraction and by the limited angular coverage of scanner geometry in PET.

2.3.1 Metal artifacts in CT

High density objects in the human body like dental fillings, hip implants, surgical clips or spine implants degrade CT images and cause artifacts because dense materials attenuate the X-rays more than anatomical structures in the body. Figure 2.4 shows metal artifacts in various CT images.

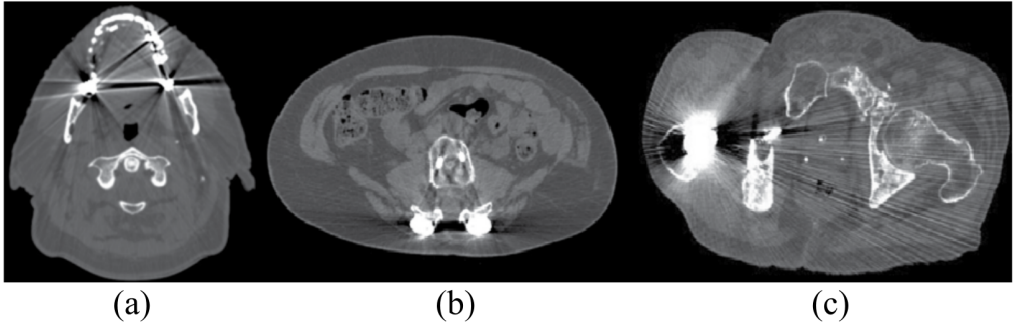


Figure 2.4: Metal artifacts in CT, (a) dental fillings, (b) spine screws, (c) hip replacement. Modified from [16].

There are several mechanisms through which artifacts occur in the presence of metallic objects. The ones that impact the image quality the most are beam hardening, photon starvation, scatter, noise, and the non-linear partial volume effect [13, 17]. Among them, the most dominant ones are beam hardening, scatter and noise [18]. In the case of dental implants, the objects are often small, but the metals used in fillings, crowns, screws etc. can have very high densities. Therefore, the major mechanism in the formation of metal artifacts in dental CT is partial or complete photon starvation. The metal artifacts are commonly visible as bright and dark lines or bands along the axis of attenuation originating from the metals. The ways for reducing artifacts in the presence of metallic objects can be put into one of these categories according to [17]:

- Removal of the metallic objects from the FOV if possible, which is often not feasible.
- Changing parameters of the CT scan to minimize the artifacts, which doesn't necessarily improve the image quality enough for clinical use.
- Correction of the raw measurement data or reduction of the artifacts during image reconstruction using metal artifact reduction (MAR) methods. The correction of artifacts with various reconstruction and correction methods has been widely researched.

- Replacement of corrupted projections if data cannot be corrected. Interpolation methods are commonly used to replace the corrupt data values, but they can cause detail loss at the metal/tissue boundary, which is usually the region-of-interest (ROI) [19].
- Use of iterative reconstruction methods to model and compensate for the corrupted data.
- Application of filters or post-processing on the reconstructed images to reduce artifacts.

There are several commercial solutions for MAR in CT. Philips Healthcare (Cleveland, OH) and Siemens Healthcare (Forchheim, Germany) have adopted hybrid methods, in which iterative approaches are combined with projection completion methods for better image quality and reconstruction speed. For instance, the metal artifact reduction for orthopedic implants (O-MAR) method used in Philips Ingenuity Core iteratively subtracts the correction image from the original image [20]. Although this method was initially designed for orthopedic implants only, it was later found to be effective for dental implants as well [21]. Siemens uses iterative metal artifact reduction (I-MAR) in its Somatom Definition Flash scanner, in which sinogram inpainting is combined with a weighted filtered backprojection [22]. Single-energy-MAR (SEMAR) in Toshiba Aquilion ONE CT (Toshiba Medical Systems, Otawara, Japan) has an iterative MAR method as well, in which the projection completion iteratively fills the gaps left by the segmentation [23]. GE Medical Systems (Milwaukee, WI) on the other hand, has implemented both hardware, dual energy imaging in HD750 Discovery system, and software, compensating for the photon starvation in monochromatic imaging in GE Revolution EVO called SmartMAR, solutions for MAR [20]. In this thesis, P I, P III and P V focus on the reduction of metal artifacts on the measurements of dental CT using iterative reconstruction methods, which take available *a priori* information under consideration.

2.3.2 Artifacts due to limited angular coverage in PET

Full ring structures are the most common geometry for PET scanners and typically have high detection efficiency and high count rates, resulting in good spatial resolution. However, several limitations such as limited FOV, low sensitivity (for scanning of small subjects), restrictions posed by multimodality imaging, and the high cost of full ring structure have led to the exploration of different geometries in PET. Some of the geometries used for PET scanners can be seen in Figure 2.5. Panel PET scanners like Figure 2.5a provide flexible FOV and compact system size [24]. Fewer detectors also decrease its price compared to a full ring scanner, but the count rate is low because of the large gap. Partial ring PET scanners like Figure 2.5b consist of partial rings that are rotated to acquire complete projection data. Such a configuration was used in ECAT ART (Siemens/CTI, Inc., Knoxville, TN), in which the rings were asymmetrically positioned and rotated to achieve full angular coverage. Partial ring and panel PET scanners for breast cancer screening, called positron emission mammography (PEM), were also investigated for breast cancer screening [25]. A recent review on commercial PEM scanners can be found in [26]. Alternatively, the partial ring scanners might not have a large gap between two panels, but smaller gaps between each detector head as in Figure 2.5c–e. The configuration in Figure 2.5c is the most popular among the manufacturers due to its high count rate and detection efficiency [?]. Hexagonal or octagonal geometries like Figure 2.5d and e can have more flexible FOVs with small gaps between detector blocks compared to partial

rings like Figure 2.5b. The flat panels in Figure 2.5d can be changed into curved panels in Figure 2.5e. The HRRT (High Resolution Research Tomograph, Siemens Medical Solutions) system is an example of an octagonal PET scanner for brain imaging.

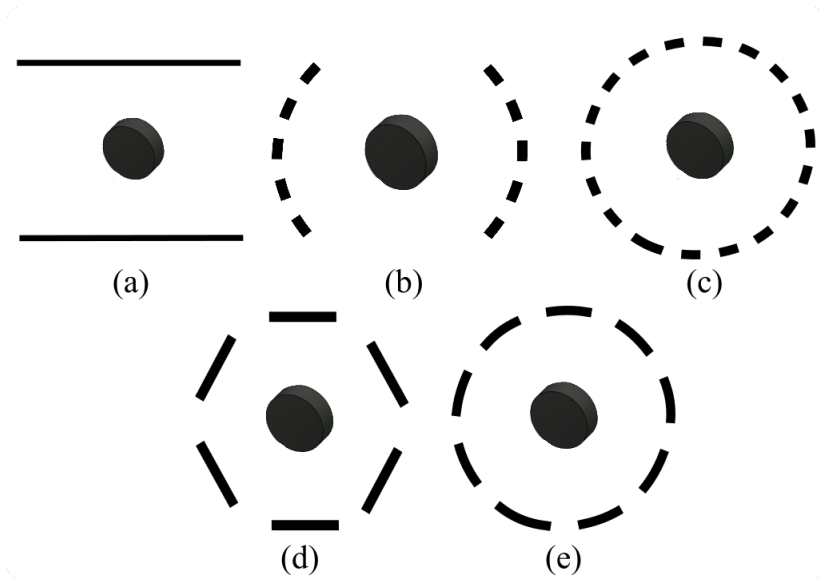


Figure 2.5: Various geometries of PET systems in clinical use. (a) Dual-panel, (b) Partial ring, (c) Full ring, (d) Hexagonal and (e) Octagonal PET configurations. Modified from [?].

3 Image Reconstruction

The art of obtaining information about the human body through the measurements is called image reconstruction. Image reconstruction consists of a forward and an inverse problem. A forward problem is defined as the transform of a matrix into a different domain via an operator. In a forward problem, the source of the information is clear and its discrete representation is written as

$$\mathbf{p} = \mathbf{A}\mathbf{x}, \quad (3.1)$$

where \mathbf{A} is the transform operator acting from the known image \mathbf{x} , in a column form, into projection \mathbf{p} . When one tries to compute \mathbf{x} back from \mathbf{p} , this problem is defined as the inverse problem. For simplicity of expressions in the equations, the image vector containing all x_j at the voxels $j = 1, 2, \dots, J$ is denoted as \mathbf{x} , the projection vector containing all p_i at the i^{th} bin in the transformed domain with $i = 1, 2, \dots, I$ is denoted as \mathbf{p} and the projection operator matrix containing all values of a_{ij} is denoted as \mathbf{A} . Each element of \mathbf{A} , a_{ij} , can be calculated by varying the parameters of the measurement one at a time and then recording the measurement. As a result, image vector \mathbf{x} is of size $J \times 1$, the projection vector \mathbf{p} is of size $I \times 1$ and the projection operator \mathbf{A} is of size $I \times J$. An example of forward and inverse problem in medical imaging can be seen in Figure 3.1.

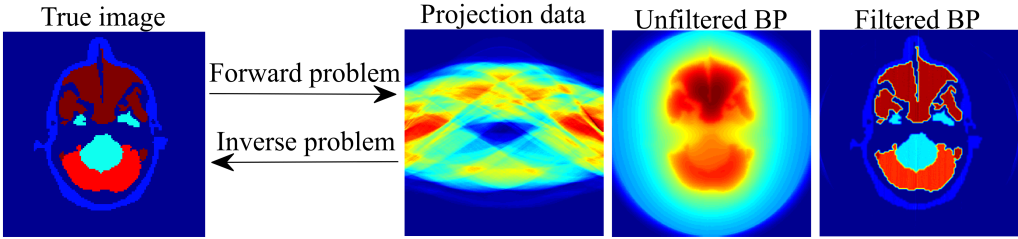


Figure 3.1: An example image and its projections as well as forward and inverse problems. Estimates of the true image using backprojection (BP) without and with filtering are also presented.

To recover \mathbf{x} perfectly, the inverse problem would need to satisfy Hadamard's conditions [27]:

- The problem has a solution (existence);
- The problem has at most one solution (uniqueness);
- The solution changes continuously depending on the input (stability).

If these conditions are satisfied, the problem is well-posed and the image can be perfectly recovered. Otherwise, the problem is ill-posed, for which the direct inversion of the matrix \mathbf{A} is not possible. Reconstruction of medical images is an ill-posed problem due to several reasons. In a discrete setting, ill-posedness can be due to the non-existence of a solution, which occurs due to the approximation of the forward model or the noise in the measurement. Discretization of a physically continuous system can lead to non-uniqueness of the solution, meaning that when the number of measurements is different than the number of voxels, $I \neq J$, reconstruction with the direct inversion of matrix \mathbf{A} is not possible. As the inversion procedure assumes complete data, incomplete projections can cause artifacts upon image reconstruction. Even round-off errors might affect the rank of the matrix. If the system is under-determined, meaning that number of measurements is less than number of pixels ($I < J$), the solution is not unique. Even for a linear problem, which is the assumption for transmission imaging, where direct inversion is possible, non-uniqueness of the solution is possible due to measurement uncertainties [1]. Therefore it is often preferred to have an over-determined system rather than an under-determined one so that the measurement uncertainties are better accommodated. When Hadamard's third condition is violated, the solution becomes unstable and small errors in the measurement can be amplified in the solution space [28]. For instance, noise can cause measurements to have overlapping magnitudes, making a full-rank \mathbf{A} matrix appear singular (non-invertible). Small changes induced by noise might also make measurements seem independent despite being parallel, resulting in singularity [1].

3.1 Analytical reconstruction methods

In ill-posed problems, the total number of voxels J is different than the total number of measurements I , making \mathbf{A} a non-square matrix, which cannot be inverted directly [1]. When direct inversion of the matrix is not possible, it becomes an estimation problem. Let the pseudo-inverse of matrix \mathbf{A} be approximated with \mathbf{A}^+ , also called Moore-Penrose inverse, then the solution of $\mathbf{Ax} = \mathbf{p}$ becomes

$$\hat{\mathbf{x}} = \mathbf{A}^+ \mathbf{p}, \quad (3.2)$$

where $\hat{\mathbf{x}}$ is the estimate for image \mathbf{x} . For a non-square matrix \mathbf{A} , \mathbf{A}^+ assures $\mathbf{AA}^+ \mathbf{A} = \mathbf{A}$, $\mathbf{A}^+ \mathbf{AA}^+ = \mathbf{A}^+$, $(\mathbf{AA}^+)^T = \mathbf{AA}^+$, and $(\mathbf{A}^+ \mathbf{A})^T = \mathbf{A}^+ \mathbf{A}$ [1]. With Moore-Penrose inversion, even an under-determined ($I < J$) problem has a solution.

The matrix solution for an over-determined system can be found by solving the equation

$$\mathbf{A}^T \mathbf{Ax} = \mathbf{A}^T \mathbf{p}, \quad (3.3)$$

in which the square matrix $\mathbf{A}^T \mathbf{A}$ is inverted instead of \mathbf{A} . \mathbf{A}^T denotes the transpose of \mathbf{A} and it is referred as the backprojection operator [29]. Note that $\mathbf{A}^T \mathbf{A}$ is usually nonsingular and an inverse solution will exist. However, in the rare case of singularity, regularization is needed to allow a solution and to avoid the singularity problem. The generalized inverse of \mathbf{A} , \mathbf{A}^+ , is then expressed as

$$\mathbf{A}^+ = [\mathbf{A}^T \mathbf{A}]^{-1} \mathbf{A}^T, \quad (3.4)$$

where the term $[\mathbf{A}^T \mathbf{A}]^{-1}$ is responsible for filtering of the image. For an over-determined system, the solution for Eq. (3.3) using Eq. (3.4) is

$$\hat{\mathbf{x}} = \mathbf{A}^+ \mathbf{p} = [\mathbf{A}^T \mathbf{A}]^{-1} \mathbf{A}^T \mathbf{p}. \quad (3.5)$$

In theory, a perfect reconstruction is possible using Eq. (3.5) for a linear problem but such a solution would not be unique due to measurement uncertainties in an ill-posed setting. However, with a controlled error propagation, the obtained solutions would be closely located. To make the solution in Eq. (3.5) more stable against noise, the system can be assumed to be under-determined, and then the solution becomes

$$\hat{\mathbf{x}} = \mathbf{A}^T [\mathbf{A} \mathbf{A}^T]^{-1} \mathbf{p}, \quad (3.6)$$

which solves the inversion problem

$$\mathbf{A} \mathbf{x} = (\mathbf{A} \mathbf{A}^T)(\mathbf{A} \mathbf{A}^T)^{-1} \mathbf{p}. \quad (3.7)$$

The inversion with Eq. (3.6) is called filtered backprojection (FBP) and it is currently by far the most common reconstruction method in clinical use [30]. Note that the filtering step in Eq. (3.6) is performed prior to the backprojection. One reason for this is that the Radon transform, which is the forward projection operator, does not model the measurement process accurately. A backprojector like FBP can be more time efficient compared to using \mathbf{A}^T matrix for backprojection, but unmatched forward models and backprojection operators can cause high noise in the resulting image. Backprojection results with (Eq. (3.5)) and without (Eq. (3.6)) filtering are depicted in Figure 3.1.

3.2 Iterative reconstruction methods

When the measurement noise is high or the data is incomplete, iterative reconstruction methods are used to control the noise levels and improve the image reconstruction quality [31]. Compared to the analytical approach, an iterative method reconstructs an image multiple times. In each loop, called iterations, an image estimate is projected, compared with the measured data, and then backprojected. The calculation of a new projection at $k + 1^{th}$ iteration can be generalized as

$$\mathbf{A} \mathbf{x}^{k+1} = \mathbf{A} \mathbf{x}^k + \mathbf{A} \Delta \mathbf{x}^k, \quad (3.8)$$

where $\Delta \mathbf{x}^k$ is the corrective term for \mathbf{x}^k and it represents the difference between the measurements and the current estimate of the image at k^{th} iteration, \mathbf{x}^k . \mathbf{A} is the system matrix/projection operator. For linear systems, where \mathbf{A} doesn't change from one iteration to another, Eq. (3.8) can be written as

$$\mathbf{x}^{k+1} = \mathbf{x}^k + \Delta \mathbf{x}^k. \quad (3.9)$$

The iterations try to minimize the difference between the projection at k^{th} iteration and the measurement. The process is continued until the best estimate for the solution is achieved: convergence [11]. In iterative reconstruction methods, the imaging problem is solved by minimizing an objective function [29]. The objective function defines the relationship between the estimated and measured projections.

3.2.1 Algebraic reconstruction methods

Algebraic reconstruction technique (ART) calculates the correction term Δx^k in Eq. (3.8) for one measurement at a time and apply it to all voxels [1, 32]. The image for the next iteration \mathbf{x}^{k+1} is calculated with ART as

$$\mathbf{x}^{k+1} = \mathbf{x}^k - \frac{(\mathbf{A}_t^T \mathbf{x}^k - p_t) \mathbf{A}_t}{\mathbf{A}_t^T \mathbf{A}_t}, \quad (3.10)$$

where $t = (k \bmod I \cdot J) + 1$ [33]. ART is not a single technique, but a family of methods based on the principle of Eq. (3.10). They were among the first to be used in the reconstruction of CT data [30]. Like most of the iterative reconstruction methods, ART typically requires several iterations before a solution is reached. If an exact solution exists, ART will converge to the solution. Otherwise, the iterations will reach a limit cycle around the solution [34]. In that case, the iterations are stopped once a predetermined residual error value between the estimated and acquired measurements is reached. The main advantage of ART is its capacity for reconstruction independent from the geometry of the projection system. As long as matrix \mathbf{A} is available it can be used for the reconstruction, but the large size of this matrix is also the biggest disadvantage of ART methods [33]. Due to the long computation time of ART, FBP rapidly overtook its place in clinical practice as the standard method of reconstruction.

3.2.2 Statistical reconstruction methods

Any knowledge of the measurements prior to the reconstruction, called *a-priori* information, can be incorporated into the solution of an inverse problem. Statistical image reconstruction methods, unlike ART methods, take the nature of measurement uncertainties into consideration. In a probabilistic approach, the estimate of the image to be reconstructed, \mathbf{x} and the measurement vector, \mathbf{p} , are related via Bayes' law:

$$P(\mathbf{x}|\mathbf{p}) = \frac{P(\mathbf{p}|\mathbf{x}) \cdot P(\mathbf{x})}{P(\mathbf{p})}, \quad (3.11)$$

where $P(\mathbf{x})$ and $P(\mathbf{p})$ are the equi-probable (uniform) probability distributions of \mathbf{x} and \mathbf{p} , respectively. $P(\mathbf{p}|\mathbf{x})$ is the conditional probability of the measurement estimate given an image \mathbf{x} , and is also called likelihood term. $P(\mathbf{x}|\mathbf{p})$ is called *a posteriori* probability, as it is the conditional probability of \mathbf{x} given a set of measurements, \mathbf{p} .

3.2.3 Poisson distribution

In PET, the acquisition system is assumed to be a random process with Poisson distribution due to the Poisson statistics of the radioactive decay [11]. The logic of the arguments presented in this section follow the order in [1]. The projection operator a_{ij} transforms an image into its projections, and once normalized, also represents the probability of i^{th} measurement detected in the j^{th} voxel, $P(x_j|p_i)$. The forward model for the estimated projections, \hat{p}_i , from an image \mathbf{x} can be written as

$$\hat{p}_i = \sum_{j=1}^J a_{ij} x_j, \quad (3.12)$$

where J is the number of voxels contributing to \hat{p}_i . It is also possible to describe the estimated projections as a sum of unobservable projections/measurements v_{ij} as

$$\hat{p}_i = \sum_{j=1}^J v_{ij}. \quad (3.13)$$

These measurements are not missing due to mis-recording or misreading of data, but because of the superposition of Poisson photons, which makes it impossible to record the individual contribution of photons emitted from voxel j to bin i [35]. Assuming that each unobservable measurement v_i corresponds to a measurement p_i , the joint probability of v_i , p_i and \mathbf{x} can be written as

$$P(p_i, v_i, \mathbf{x}) = P(p_i|v_i, \mathbf{x})P(p_i|\mathbf{x})P(\mathbf{x}), \quad (3.14)$$

where $P(\mathbf{p}|\mathbf{v}, \mathbf{x}) = \sum_{i=1}^I P(p_i|v_i, \mathbf{x})$. The log-likelihood term can then be written as

$$\ln P(\mathbf{p}|\mathbf{x}) = \ln \sum_{i=1}^I P(p_i|\mathbf{v}, \mathbf{x}), \quad (3.15)$$

in which the knowledge of v_{ij} is not needed. The derivative of Eq. (3.15) with respect to \mathbf{x} results in the solution with the maximum likelihood. However, due to summing operations over measurements, it is easier to estimate the logarithm of the joint probability $P(p_i, v_i, \mathbf{x})$ according to a previously estimated image \mathbf{x}^k ,

$$Q(\mathbf{x}^{k+1}|\mathbf{x}^k) = E(\ln P(\mathbf{p}, \mathbf{v}, \mathbf{x}|\mathbf{x}^k)), \quad (3.16)$$

where $E(\cdot)$ denotes the expected value of a function. The estimation maximization of the log-likelihood, $\ln P(\mathbf{v}|\mathbf{x})$ yields to the most likely solution for \mathbf{x} . The probability can then be expressed with

$$P(\mathbf{v}|\mathbf{x}) = \prod_{i=1}^I \prod_{j=1}^J \exp(-\hat{p}_{ij}) \cdot \frac{(\hat{p}_{ij})^{v_{ij}}}{v_{ij}!} = \prod_{i=1}^I \prod_{j=1}^J \exp[-a_{ij}x_j] \frac{(a_{ij}x_j)^{v_{ij}}}{v_{ij}!}, \quad (3.17)$$

where \hat{p}_{ij} is the estimated measurements that corresponds to unobserved measurement v_{ij} . By taking the logarithm of Eq. (3.17), we get

$$\ln(P(\mathbf{v}|\mathbf{x})) = \sum_{i=1}^I \sum_{j=1}^J [v_{ij} \ln(a_{ij}x_j) - a_{ij}x_j - \ln(v_{ij}!)]. \quad (3.18)$$

By means of expectation maximization methods, we can estimate the expected values for the unobserved measurements based on the available ones. This expectation is then maximized towards the most likely solution. Assuming an estimate image \mathbf{x}^k is available, we can calculate the conditional expectation of the unobserved measurements, v_{ij} , with respect to measurements, \mathbf{p} , and estimated solution \mathbf{x}^k as follows

$$Q(\mathbf{x}^{k+1}|\mathbf{x}^k) = E(\ln P(\mathbf{p}, \mathbf{v}|\mathbf{x})|\mathbf{x}^k) = \sum_{i=1}^I \sum_{j=1}^J E(v_{ij}) \ln(a_{ij} x_j) - a_{ij} x_j - E(\ln v_{ij}!). \quad (3.19)$$

The term $E(\ln v_{ij}!)$ can be taken as constant with respect to the image, and thus can be ignored in the maximization step. As each v_{ij} contributes to j^{th} voxel in p_i (satisfying Eq. (3.13)), the expectation of the unobserved measurements, $E(v_{ij})$, can be considered the same as

$$E(\mathbf{p}, v_{ij}|x^k) = \frac{a_{ij} x_j^k}{\sum_{t=1}^J a_{it} x_t^k} p_i. \quad (3.20)$$

After taking the logarithm of Eq. (3.20), it can be maximized by taking its partial derivative with respect to x_j . By placing Eq. (3.20) into Eq. (3.19), we get

$$\frac{\partial}{\partial x_j} E(\ln P(\mathbf{p}, \mathbf{v}|\mathbf{x}|\mathbf{x}^k)) = \sum_{i=1}^I \left[\frac{a_{ij} x_j^k}{\sum_{t=1}^J a_{it} x_t^k} \frac{p_i}{x_j} - a_{ij} \right] = 0. \quad (3.21)$$

Solving the equation above for x_j results in

$$x_j^{k+1} = \frac{x_j^k}{\sum_{i=1}^I a_{ij}} \sum_{i=1}^I a_{ij} \frac{p_i}{p_i^k}, \quad (3.22)$$

which is the MLEM update equation [36, 37]. The EM algorithm, proposed by Shepp and Vardi [37], and Lange and Carson [36] can be considered as the basic approach for solving the ML problem [38]. As the log-likelihood function is concave, it is possible to show that the iterative approach in Eq. (3.22) converges to the ML estimate [39]. When nonnegative values are assumed for the system matrix elements, a_{ij} , as is often the case in radiation imaging, the values of the solution will always be nonnegative due to the multiplicative nature of the updates [36]. This is in direct contrast with algebraic reconstruction methods, which can have negative solutions.

Rather than maximizing the likelihood, one can also try to maximize the *a posteriori* probability, $P(\mathbf{x}|\mathbf{p})$, to control the noise propagation, in which case it is called maximum *a posteriori* (MAP) estimation. This method has been introduced by Geman *et al.* [40] and since been shown to successfully control the noise levels in PET reconstruction [35, 41–43]. Assuming $P(\mathbf{p})$ is constant with respect to \mathbf{x} , the objective function to be maximized becomes

$$\arg \max_{\mathbf{x}} (P(\mathbf{x}|\mathbf{p})) = \arg \max_{\mathbf{x}} (P(\mathbf{p}|\mathbf{x}) \cdot P(\mathbf{x})). \quad (3.23)$$

The maximization of a posteriori probability is essentially a regularized version of likelihood maximization by using the a priori probability, $P(\mathbf{x})$, as the regularization/penalty term. Taking the logarithm of Eq. (3.23) allows us to separate the two terms on the right hand side of the equation, which makes the regularizing role of $P(\mathbf{x})$ clear. Note that

the maximizing of the logarithm of $P(\mathbf{x}|\mathbf{p})$ is equivalent to maximizing $P(\mathbf{x}|\mathbf{p})$. The logarithm of Eq. (3.23) yields

$$L(\mathbf{x}) = \operatorname{argmax}_x \ln(P(\mathbf{x}|\mathbf{p})) = \operatorname{argmax}_x [\ln(P(\mathbf{p}|v_i, \mathbf{x})) + \ln(P(\mathbf{x}))]. \quad (3.24)$$

$L(\mathbf{x})$ in Eq. (3.24) is called the log-posterior and $\ln(P(\mathbf{p}|\mathbf{x}))$ the log-likelihood. The term $\ln(P(\mathbf{x}))$ represents any *a priori* information can be incorporated into the solution, which is calculated by maximization of the expectation of the log-posterior probability in Eq. (3.24). Note that the use of Bayesian rule can be for Poisson distributed-measurements can be justified by the fact that above a certain count rate, the Poisson distribution approaches to a normal distribution [1]. A solution for this objective function is found via EM optimization, which solves the derivative of Eq. (3.24) with respect to x_j

$$\frac{\partial L(\mathbf{x})}{\partial x_j} = \frac{\partial \ln(P(p|v_i, \mathbf{x})) + \ln(P(\mathbf{x}))}{\partial x_j} = \sum_{i=1}^I \left(\frac{p_i}{p_i^k} \frac{a_{ij} x_j^k}{x_j} - a_{ij} \right) + \frac{\partial U(\mathbf{x})}{\partial x_j} = 0. \quad (3.25)$$

As the term $\frac{\partial U(\mathbf{x})}{\partial x_j}$ is the function of an unknown image \mathbf{x} , the derivative of the prior is simply calculated at the current reconstruction \mathbf{x}^k . This approach is called one-step-late (OSL) [35]. The OSL approach works well as long as the prior strength is not too high. In extreme cases, the denominator may become zero or negative. With OSL, the MAP update term can be re-written from Eq. (3.25) into MAPEM iteration as

$$x_j^{k+1} = \frac{x_j^k}{\sum_{i=i}^N a_{ij} - \frac{\partial U(\mathbf{x})}{\partial x_j} |_{x^k}} \sum_{i=1}^I a_{ij} \frac{p_i}{p_i^k}, \quad (3.26)$$

The prior term, $U(x)$, can be used to encourage solutions of smooth or piecewise linear tracer distribution in PET. This can be achieved with a Markov prior that relates the tracer distribution of a certain voxel, x_j , to its neighboring voxels, Ne_j , as follows

$$U(x_j|x_t, \forall t \neq j) = (x_j|x_t, t \in Ne_j). \quad (3.27)$$

Such priors can be written in the form of

$$U(\mathbf{x}) = \ln(U(x)) = \sum_j \ln U(x_j|x_t, t \in Ne_j) = -\beta \sum_j \sum_{t \in Ne_j} F(x_j x_t), \quad (3.28)$$

where the energy function $F(\cdot)$ suppresses the noise and β determines the weight of the prior. Higher weights lead to smoother images, but decrease the likelihood, i.e. the agreement between the measurement and the estimate is poorer. Most priors take advantage of a simple energy function that is calculated from the absolute difference of $|x_j - x_t|$. Some examples of these functions are quadratic prior, the Huber prior and Geman prior. The prior term in Eq. (3.28) is a concave function if $F|x_j - x_t|$ is convex. This means that the convex energy functions of quadratic and Huber priors lead to a

concave prior with a single maximum. Geman prior on the other hand is not concave, and therefore has local maxima. This makes the initialization of the prior is highly important as the reconstruction result depends on the initialization and the algorithm's behavior. The penalty weight can be incorporated into MAP as

$$x_j^{k+1} = -\frac{x_j^k}{\sum_{i=1}^I a_{ij} + \beta \frac{\partial U(x)}{\partial x_j} \big|_{x_j=x_j^k}} \sum_{i=1}^I \frac{p_i}{\sum_{j=1}^J a_{ij} x_j^k} a_{ij}. \quad (3.29)$$

One can see that MLEM is a special case of MAPEM with $\beta = 0$. With the use of subsets for data reconstruction, the MLEM becomes ordered subset expectation maximization (OSEM) [44]. It is important to note that OSEM has different convergence rates in low and high-count regions, high counts converging faster than the low-count areas [45]. MAPEM approach was used for image reconstruction throughout P I– P IV and compared with MLEM as well as FBP in these publications due to the widespread use of these methods in clinical practice.

3.2.3.1 Least squares methods

The image reconstruction is always ill-posed due to the discretization that creates a matrix from physically continuous forward model. Therefore, a modified matrix, as opposed to the noninvertible matrix \mathbf{A} , is needed for inversion method. The solution of of Eq. (3.2) minimizes the residual error e

$$e = \|\mathbf{p}^{measured} - \mathbf{A}\mathbf{x}\|_2, \quad (3.30)$$

where $\mathbf{p}^{measured}$ denotes the actual measurements with a certain measurement error. Eq.(3.30) is called the least-squares (LS) solution of $\mathbf{A}\mathbf{x} = \mathbf{p}$, as minimizing the residual norm is equivalent to minimizing the LS objective function

$$e^2 = [\mathbf{p}^{measured} - \mathbf{A}\mathbf{x}]^T [\mathbf{p}^{measured} - \mathbf{A}\mathbf{x}] \quad (3.31)$$

Eq. (3.5) is the optimal solution for minimization of Eq. (3.31). The square term makes the assumption that the difference between the measured and modeled/estimated values most likely follow a normal distribution with zero mean.

The LS solution of Eq. (3.5) is a special case, a weighted form, of the solution obtained with singular value decomposition (SVD):

$$\hat{\mathbf{x}} = [\mathbf{A}^T \mathbf{W} \mathbf{A}]^{-1} \mathbf{A}^T \mathbf{W} \mathbf{p}^{measured}, \quad (3.32)$$

where \mathbf{W} is $J \times J$ weighting diagonal matrix and it is used for putting more weight on the solutions with less uncertainty. The pseudo-inversion in SVD eliminates the direct singular values, but such control is not possible in the LS solution. Therefore regularization methods are used to constrain the solutions. Regularization is used for reaching a minimal error, which is measured by the residual norm. It is also possible to add prior information into LS methods. Some of the most commonly used methods for the optimization of LS problem are iterative coordinate descent [46], conjugate gradient [47], penalized weighted least squares [48] and adaptive-steepest-descent-projection onto convex sets (ASD-POCS). A modified LS algorithm was implemented in P V.

3.3 Use of priors in reconstruction

Any form of prior information, such as the probability distribution of measurements or the structures in the image can be incorporated into the reconstruction via $P(x)$ term in Eq. (3.24). It is added into the MAP methods as a penalty term (see Eq. (3.29)). The role of this term is to ensure the agreement of the solution with the knowledge on the image. In PET, the radioactivity concentration is assumed to be piecewise-constant. It is also known that the nature of the measurement system is Poisson-like. Median root prior and total-variation prior are two priors that are suitable for these assumptions.

Median root prior (MRP) comes from the family of Gaussian priors, which generally compare the intensity values within a local neighborhood of the reconstructed image and allow the values that match with the assumption of the image. Noise is considered as an abrupt change in intensity values between neighboring voxels and the aim of Gaussian type priors is the suppress the noise in an image by averaging these voxels. The image in Figure 3.2b was filtered using a Gaussian type averaging filter with size $[3, 3]$, which calculates the average or mean of the values within a certain neighborhood. In the case of MRP, the image is assumed to be piecewise constant, that the values within a local neighborhood are non-decreasing or non-increasing [49]. The comparison of the intensity values is done with respect to the median of the local neighborhood. A large discrepancy between the median and a voxel value is penalized. A comparison of median filtering operation with Gaussian filtering (averaging filter) is shown in Figure 3.2 on a brain phantom contaminated with Poisson noise. .

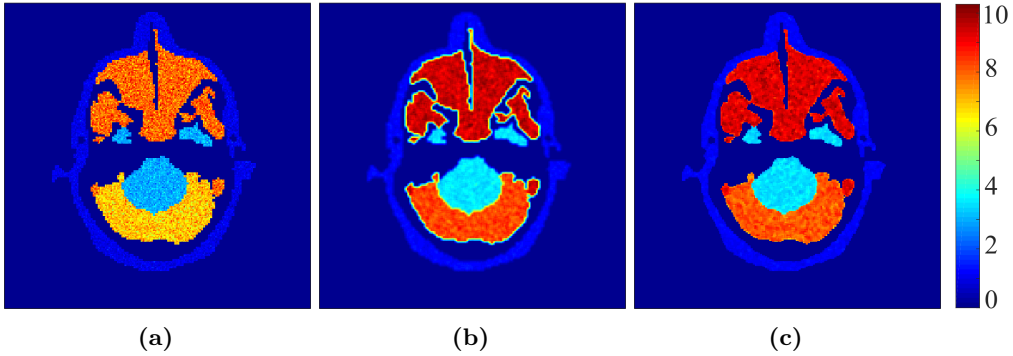


Figure 3.2: Example of (a) the noisy brain phantom with Poisson noise, (b) de-noised image with averaging filter and (c) de-noised image with median filter .

It is visible from Figure 3.2c that the noise is successfully removed by median filter using a 2D filter size of $[3, 3]$, which is the only parameter needed. The blurring is visible on the smaller structures of the Figure 3.2b, which is not present in Figure 3.2c. Edges in an image usually cause abrupt changes in the intensity values, which are often penalized along with the noise, leading to blurry images. The penalization with a median filter prevents the blurring of the edges in the reconstructed image.

There is no analytical derivative to be calculated for $\frac{\partial U(x)}{\partial x}$ in MAP with MRP. Instead, the derivative term is replaced with $\frac{x_j^k - M_j}{M_j}$, where $M_j = \text{Med}\{x_j^k | j \in N_j\}$ and it is the median value of the voxels around the j^{th} voxel. As a result, the MAPEM iteration with MRP is written as

$$x_j^{k+1} = -\frac{x_j^k}{\sum_{i=1}^I a_{ij} + \beta \frac{x_j^k - M_j}{M_j}} \sum_{i=1}^I \frac{p_i}{\sum_{j=1}^J a_{ij} x_j^k} a_{ij}. \quad (3.33)$$

The hyperparameter β determines the weight of the penalization. More information on its effect on the reconstruction with MRP is available in [50]. MRP was the chosen prior term for penalization in the reconstruction methods of P I, P III, and P IV.

Total variation (TV) prior is another effective way of incorporating prior information into both MAP and LS methods. It is based on the TV norm, which is the sum of $l1$ norms of the image gradient. Let the TV norm of image C be defined as function u with elements in 3 dimensions r , s , and t

$$\begin{aligned} U(C)_{TV} &= \sum_{r,s,t} u(r, s, t) \\ &= \sum_{r,s,t} \sqrt{(C_{r+1,s,t} - C_{r,s,t})^2 + (C_{r,s+1,t} - C_{r,s,t})^2 + (C_{r,s,t+1} - C_{r,s,t})^2 + \epsilon}, \end{aligned} \quad (3.34)$$

where a small value of ϵ around 10^{-8} ensures differentiability of the function [51]. The minimization of the TV norm in Eq. (3.34) also minimizes the $L1$ -norm of the gradient image [29]. The derivative of the function u described above is

$$\begin{aligned} \frac{\partial U(C)}{\partial C_{r,s,t}} &= \frac{C_{r,s,t} - C_{r-1,s,t}}{u(r-1, s, t)} \\ &+ \frac{C_{r,s,t} - C_{r,s-1,t}}{u(r, s-1, t)} + \frac{C_{r,s,t} - C_{r,s,t-1}}{u(r, s, t-1)} \\ &+ \frac{C_{r+1,s,t} + C_{r,s+1,t} + C_{r,s,t+1} - 3C_{r,s,t}}{u(r, s, t)}. \end{aligned} \quad (3.35)$$

The high intensity differences at the edges are more pronounced in the gradient image, whereas the locally monotonic regions have zero gradient. Due to this gradient operation, TV norm favors sparsity of the gradient image, in which there is groups of monotonic regions, separated by edges or boundaries [1, 52]. This assumption helps to preserve the edge sharpness in the reconstructed image while reducing the noise. When the TV prior is implemented within the MAPEM scheme, MAPEM becomes TV regularized EM (TV-EM):

$$x_j^{k+1} = -\frac{x_j^k}{\sum_{i=1}^I a_{ij} + \beta \frac{\partial TV(x_j)}{\partial x_j} \big|_{x_j=x_j^k}} \sum_{i=1}^I \frac{p_i}{\sum_{j=1}^J a_{ij} x_j^k} a_{ij}, \quad (3.36)$$

where $TV(x_j)$ is the derivative of the TV norm of image \mathbf{x} at j^{th} voxel at iteration k . The TV norm of the 2D brain phantom with and without Poisson noise can be seen in Figure 3.3. The TV norm of the noiseless image highlights the edges, whereas the norm of the noisy image recovers the edges but also includes the voxel-wise changes induced by

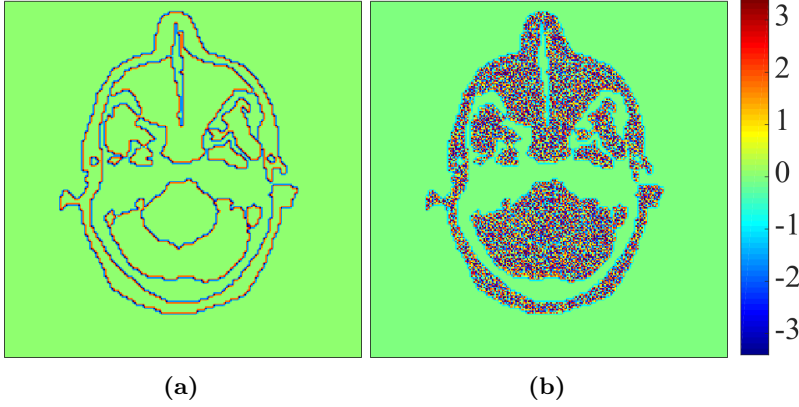


Figure 3.3: TV norms of (a) noiseless and (b) noisy brain phantom

the noise. As a result, the boundaries of the structures within the brain are lost due to the noise.

With the assumption that both likelihood and *a priori* probability density function have normal distribution, TV prior can be easily implemented as a cost function into the reconstruction, resulting in the minimization of the objective function

$$\|Ax - p\|_2^2 + \|\nabla a(x)\|_1, \quad (3.37)$$

where

$$\nabla a(x) = \sum_j \frac{\partial}{\partial x_j} TV(x) \delta_j. \quad (3.38)$$

TV prior was implemented within MAPEM and compared with MRP as a prior in P IV for in-beam PET data. It was also incorporated into LS in P V for MAR in dental CT.

3.4 List-mode data reconstruction

Reconstruction of list-mode data is based on the backprojection of each recorded event using the full knowledge coming from the detectors. The use of list-mode data in reconstruction was first proposed by Barrett *et al.* [9] and the list-mode reconstruction via EM algorithm for PET was first developed by Parra *et al.* [53]. Several algorithms have been developed since then, mostly on the use of subsets and regularization techniques within the reconstruction to improve the computational efficiency of list-mode reconstruction [54–57]. Although many reconstruction methods have been proposed for histogrammed projection data, development on list-mode reconstruction methods have been limited [8]. This was largely because the count rate has been high enough to make the histogramming more efficient for reconstruction than list-mode data processing. In applications with low count rate, however, there are numerous advantages of list-mode reconstruction. It results in higher resolution, better noise levels and contrast. The TOF information can also be easily incorporated into the list-mode reconstruction [54]. The low statistics of PET data in applications such as breast imaging ([25]) and proton therapy ([58]), together

with implementation of TOF information and irregular scanner geometries have put more focus on the list-mode reconstruction in recent years.

The ML estimation of list-mode data via EM can be derived from the MLEM reconstruction of histogrammed data, which was formulated earlier in Eq. (3.22). With list-mode data, the p_i term in Eq. (3.22) is taken as 1 as each projection in histogrammed data corresponds to a single event in the processing of list-mode data [54]. Measured data has simply I events in total instead of I projections. The term $\sum_{j=1}^J a_{i,j}$ is the normalization term, which represents all possible LORs between detectors. When the histogrammed data is replaced with individual events, the MLEM equation stays almost the same and can be written as

$$x_j^{k+1} = -\frac{x_j^k}{\sum_{i=1}^I a_{ij}} \sum_{i=1}^I \frac{1}{\sum_{j=1}^J a_{ij} x_j^k} a_{ij}. \quad (3.39)$$

The equation above is a slow method for reconstruction, as each event is backprojected individually instead of the processing of the bins in the histogrammed data. In order to speed it up, the reconstruction can be divided into subsets. This is easy to implement with list-mode data because each event is independent from others. In the reconstruction of histogrammed data with subsets, only the projections in the subset are used for normalization of the data. In contrast, with list-mode data, all normalization factors can be included in the reconstruction of every subset, making the backprojection of each subset more accurate. There are several methods to incorporate the subsets into the update equation of the image estimates (see [55] and [56] for various methods for incorporation of subsets into reconstruction). One of the main decisions in using subsets is how to divide the data. There are 3 main approaches: preset-counts (each subset has the same number of events), preset-time (data is divided into equal time durations), and preset-geometry (each subset covers a certain region in the FOV) [59]. In P IV, preset-count approach was selected, in which all events in every subset are backprojected, then all subsets are summed together and used to update the image. This way, the extremely low statistics of data in each subset do not affect the noise levels in the image update and the convergence of MLEM part of the algorithm is preserved.

4 Evaluation Criteria

4.1 Assessing overall image quality

Mean squared error (MSE) is a measure of noise in the reconstructed image with respect to a ground truth. It is the square of the error between the reconstructed image and the ground truth. The MSE of images a and b is calculated as

$$MSE(a, b) = \frac{1}{J} \sum_{j=1}^J (a_j - b_j)^2, \quad (4.1)$$

where subscript j represent the j^{th} voxel of the images. MSE is straight-forward to calculate and has a clear physical meaning, which is why it is often used as a stopping criteria for iterative reconstruction algorithms. The iterative reconstruction process is stopped when the error between the two images from consecutive iterations is below a set threshold. MSE and its variations, normalized MSE (NMSE) and root mean squared error (RMSE), were used in P I, P III and P V. MSE was also used for the comparison of proposed reconstruction methods for MAR in this thesis.

Structural similarity index (SSIM) is based on the human visual system and it gives importance to the preservation of structural information within an image [43]. Despite its simplicity, MSE doesn't capture the difference in the cases of contrast stretch, mean luminance shift, contamination by additive white Gaussian noise, impulsive noise distortion, JPEG compression, blur, spatial scaling, spatial shift, and rotation [43]. In these cases, another image fidelity measure like SSIM can be employed. The human visual system can compensate for non-structural changes in the image (i.e. change in contrast, luminance or brightness), but it is very sensitive to structural changes such as blurring, additive noise or lossy compression. SSIM is a combination of three separate measures: luminescence ($l(a, b)$), contrast ($c(a, b)$) and structure ($s(a, b)$). Depending on the application area, the weight for these measures can be adjusted.

$$SSIM(\mathbf{a}, \mathbf{b}) = l(\mathbf{a}, \mathbf{b}) \cdot c(\mathbf{a}, \mathbf{b}) \cdot s(\mathbf{a}, \mathbf{b}). \quad (4.2)$$

SSIM values are in the range of $[0, 1]$ and two identical images result in SSIM being 1. SSIM was used in P V in order to evaluate the structural similarity between the ground truth and reconstructed images.

Normalized mutual information (NMI) was initially developed for evaluating the quality of multimodal image registration in [60]. However, nowadays it is also used to

evaluate the similarity of information between two images [61]. The NMI is calculated through the Shannon entropy of the images, giving the value of 1 if two images are identical. The Shannon entropy of image \mathbf{a} is

$$H(\mathbf{a}) = - \sum_{i=1}^I p(i) \log(p_i), \quad (4.3)$$

where i is the voxel index of image \mathbf{a} , and the probability $p(i)$ that the value of the i^{th} voxel occurs is calculated from the histogram of the image. The respective entropies of two images \mathbf{a} and \mathbf{b} are $H(\mathbf{a})$ and $H(\mathbf{b})$. $H(\mathbf{a}, \mathbf{b})$ represents the entropy of the joint intensity histogram of two images \mathbf{a} and \mathbf{b} [61]. It is defined as

$$H(\mathbf{a}, \mathbf{b}) = - \sum_{i,j} p(i, j) \log p(i, j), \quad (4.4)$$

where the i and j are voxel indices for images \mathbf{a} and \mathbf{b} and $p(i, j)$ is the joint probability [62]. The mutual information (MI) between the two images can be written as

$$MI(\mathbf{a}, \mathbf{b}) = H(\mathbf{a}) + H(\mathbf{b}) - H(\mathbf{a}, \mathbf{b}), \quad (4.5)$$

The NMI is then defined as

$$NMI(\mathbf{a}, \mathbf{b}) = \frac{MI(\mathbf{a}, \mathbf{b})}{\sqrt{H(\mathbf{a})H(\mathbf{b})}}, \quad (4.6)$$

For the calculation of NMI, all images are scaled between $[0, 255]$, enabling comparison of images even when the intensity values are dissimilar. When the reconstructed intensity values do not have clinical importance, as in the list-mode reconstruction in P IV, the NMI becomes a useful tool to evaluate conformity of reconstruction with the ground truth.

4.2 Region of interest analysis

Coefficient of variation (CoV) is used to evaluate the noise levels of a region within a homogeneous ROI. It is defined as the ratio between the standard deviation (σ_{ROI}) and the mean (μ_{ROI}) intensity values of the ROI.

$$CoV(\%) = \frac{\sigma_{ROI}}{\mu_{ROI}} \quad (4.7)$$

The higher is the CoV value, the higher is the noise. CoV was calculated in this thesis to compare the MAR methods within homogeneous ROIs as well as in P IV.

4.3 Evaluation of the edges

In medical imaging, the boundaries of anatomical regions need to be reconstructed as accurately as possible in order to avoid misinterpretation in diagnosis. Also in proton therapy treatments, where a focused proton beam is applied onto the cancerous region, the beam needs to be positioned correctly to prevent radiation of the healthy tissue. The edges of an image can be assessed via analysis of its 1D profile along a certain direction.

Line profile is the intensity profile of an image along a line drawn through one of its dimensions. The intensities along this line can be compared with the line profile of a reference image. They are also useful for calculating image properties like FWHM of an object or the location of Bragg peak in proton therapy (the point where the protons lose their energies and stop). Line profiles were used in P I – P V to study the recovery of intensity values and to compare the steepness of the edges.

Sigmoid fit is a nonlinear curve that is fitted between the beginning and end points of a known edge on a line profile. It is a useful criterion when the line profile is noisy. After a sigmoid function is fitted on an edge, a point on this fit, i.e. 20%, 30% or 50 % of the maximum value, is used to calculate the location of an edge and the steepness of its slope. Although there are several sigmoid function, the sigmoid fits in this thesis are calculated using

$$sig(h) = base + \frac{max}{1 + exp(\frac{h_0 - h}{b})}, \quad (4.8)$$

where h is the voxel index. The $base$ and max are the beginning and end points of the sigmoid fit. h_0 is the position at which 50 % of the difference between max and $base$ is reached. b parameter determines the steepness of the slope fitted on the edge. The smaller is the b , the steeper is the edge. Sigmoid fits can be used in analysis of the reconstruction methods in terms of edge sharpness, spatial resolution and FWHM. They were used in P IV for a quantitative evaluation of the edges in the reconstructed images than line profiles.

5 Artifact Reduction in CT

5.1 Review of previous work

Metallic objects are common in dental imaging, and they are removed prior to the measurements whenever possible. However, when metals cannot be avoided in the FOV, MAR methods are used. MAR can be seen as a reconstruction from incomplete projection data, where metallic regions are treated as missing information once extracted from the data. With metals present in projection data, the first step is to identify the regions with metallic objects and segment them out. The segmented region can then either be filled via projection completion methods or excluded from the reconstruction after incorporating the knowledge of its location into the iterative reconstruction algorithms.

Identification of metallic regions in MAR on a dental CT image is not a straightforward problem because the metal artifacts stretch along the anatomical structures. Although it is theoretically possible to segment the metals in the image (spatial) domain [63, 64], the data is obtained in projection domain and segmentation from a reconstructed image is prone to errors caused by the reconstruction algorithm itself. Mistakes in segmentation can cause artifacts, especially in dental CT, since metallic objects and teeth can have similar attenuation coefficients [65]. Some other segmentation approaches include manual segmentation by Kalender *et al.*, adaptive segmentation mixed with FBP by Mahnken *et al.*, mean-shift technique by Yu *et al.*, active contour model by Xue *et al.*, fusion prior-based MAR scheme by Wang *et al.*, and average filtering in addition to thresholding by Wei *et al.*. Other examples are the use of Markov random field to identify affected projections by Veldkamp *et al.*, Steger method by Xu *et al.*, which detects curvilinear structures for precise determination of small metal object edges, and tissue-class models by Olive *et al.*. See [17] for a more detailed review of these methods. The segmentation of metals from the projections was studied as a part of the proposed MAR method in P I in order to avoid segmentation errors in image domain.

Once the metallic regions are segmented and extracted from the measurements, the gaps left in the places of metallic imprints create inconsistencies in the data. These inconsistencies can result in severe artifacts upon applying analytic reconstruction methods. Projection completion methods can be employed to fill the gaps in measurements by interpolation of the available data, artificially creating consistent data. Approaches for projection completion include wavelet interpolation, adaptive filtering, linear or polynomial interpolation [66]. Other more elaborate projection completion methods have been suggested in [67–70]. The idea behind all these methods is to reduce the metal artifacts by pre-processing the projection data and, thereby, make it suitable for fast, analytic reconstruction.

The most common method for projection completion is called inpainting. It was first

used in digital image processing in [71] and then adapted for MAR in CT by Duan *et al.* [72]. The inpainting method interpolates the voxel values surrounding the unknown part of the measurements to estimate the intensity values of the unknown bins. If the gaps are not filled correctly, projection completion methods carry the risk of misinformation, especially at the metal/tissue boundary. Inaccurate estimation of the unknown bins can result in the loss of the distinct boundaries between the known and estimated bins, making the diagnosis difficult. Possible jumps at the boundaries of unknown and measured bins can also create secondary artifacts upon FBP reconstruction [73]. Filtering and thresholding the projection data in wavelet domain can decrease secondary artifacts, as was suggested in [67]. Zhao *et al.* implemented a multiresolution approach to wavelet-based filtering for MAR using CT data for hip joint prosthesis. It was found to be effective in reducing the artifacts from beam hardening and photon starvation [67].

Another way to avoid secondary artifacts is to combine projection completion methods with iterative reconstruction methods. Some of the recent examples in the literature are [66, 73–75]. However, as such approaches take much longer than FBP, they no longer provide the advantage of a fast reconstruction. In [66], Mehranian *et al.* proposed a projection completion method with a regularized optimization scheme for MAR by incorporating a wavelet-based Gaussian prior into the Bayesian reconstruction scheme for X-ray CT data. A wavelet domain interpolation of the sinogram data allowed the exploitation of the sparse nature of the sinogram. Daubechies 7-9 biorthogonal wavelets with hard thresholding were used for filtering in wavelet domain. In [74], Tang *et al.* utilized thresholding and a weighting image for the voxels near the metals, then smoothened them via cubic interpolation to reduce secondary artifacts. The masked sinogram and weighted image was reconstructed using TV based ASD-POCS to obtain artificial projection values for the metallic regions, which was later used as the initial image for FBP. Such a hybrid approach was used in P V, which combined inpainting with iterative reconstruction methods to prevent secondary artifacts.

Iterative reconstruction methods have also been successfully implemented as stand-alone solutions for MAR. These methods often incorporate the information about the locations of metals into the reconstruction in the form of correction sinograms, which can free the images from the risk of false values and boundaries. The iterative reconstruction methods (EM and ART) for MAR were first suggested by [76] without any gap filling. The idea of using iterative approach for MAR was further improved by [52, 75, 77, 78]. Iterative reconstruction methods are in general more robust against incomplete projections caused by the metallic objects. While the completion of projections is a must for the use of analytic reconstruction methods, the filling of the metallic regions is a more of a matter of preference in iterative reconstruction.

5.2 Methods

Sequentially applied MAPEM (sMAPEM) was implemented using OSL approach in P I [79]. It was selected for MAR due to its ability to accommodate detector gaps and edge preservation abilities [79]. MRP was chosen for incorporating prior information into the reconstruction. Firstly, the sinogram bins, which were affected from the metal objects, were segmented out using a multilevel segmentation method. In the update step, the values of the metallic regions were replaced with 1 in $J_{i_{metals}}$, which were later estimated via MLEM. The projection data without metals, p_i for $i=1,2,...,I$, were used in MAPEM. The image estimate for the next iteration was calculated with sMAPEM as

$$x_j^{k+1} = \frac{x_j^k}{\sum_{i=1}^I a_{ij} + \beta \frac{x_j^k - M_j}{M_j}} \cdot \sum_{i=1}^I \left(\frac{p_i}{\sum_{j=1}^J a_{ij} x_j^k} + J_{i_{metals}} \right) a_{ij}, \quad (5.1)$$

where M_j is the penalty reference calculated by median filtering of the current image estimate for a local neighborhood around the j^{th} voxel [49]. Throughout the iterations, the strength of the regularization was set by gradually decreasing the value of the penalty weight β from 1 to 0.01. With this sequential application of the spatial domain regularization filter, the missing parts of the sinograms were filled consistently while the undesired effects (such as blurring) of the spatial domain regularization filter were minimized.

Adaptive multiresolution MAPEM (amMAPEM) was used in P III for the reconstruction of a jaw phantom after segmentation of metallic regions with multi-level Otsu's thresholding. The reason for using this reconstruction was its shorter reconstruction time compared to sMAPEM, as well as its performance in the presence of missing wedges in electron tomography [80]. Unlike the single resolution level in sMAPEM, amMAPEM reconstructs the image at different resolution levels to speed up the algorithm. The amMAPEM uses the formula of

$$x_j^{k+1} = \frac{x_j^k}{\sum_{i=1}^I a_{ij} + \beta_j \frac{x_j^k - M_j}{M_j}} \cdot \sum_{i=1}^I \frac{p_i}{\sum_{j=1}^J a_{ij} x_j^k} a_{ij}, \quad (5.2)$$

where β_j is a voxel-wise regularization parameter determined by the voxel values in the previous resolution level. The summing of voxels in lower resolution levels provides a natural noise penalization. M_j was calculated from the median values in the neighborhood of each voxel. The iterations at each resolution level were stopped once a pre-determined error between two consecutive iterations was reached. The final estimate for each resolution level was used as an initial estimate for the next one. In this case, no gap filling was used in order to avoid errors during resizing between resolution levels.

Multiresolution conjugate gradient with total variation penalty (MRTV-CG) was implemented in P V as an LS method for tomographic data reconstruction for MAR. The conjugate gradient LS (CGLS) method tries to invert

$$\mathbf{A}\mathbf{x} + \boldsymbol{\eta} = \mathbf{p}, \quad (5.3)$$

where \mathbf{A} is the projection operator (Radon transform in this case) and \mathbf{x} is the image in spatial domain. \mathbf{p} is the measurement vector and $\boldsymbol{\eta}$ is the noise term given by $\boldsymbol{\eta}(x) = \mathbf{D}\mathbf{x}$, where \mathbf{D} is a regularized form of TV penalty. A regularized solution of Eq. (5.3) can be obtained through the following TV regularized algorithm:

$$\mathbf{x}_{\ell+1} = (\mathbf{A}^T \mathbf{A} + \mathbf{D} \Gamma_{\ell} \mathbf{D})^{-1} \mathbf{A}^T \mathbf{y}, \quad (5.4)$$

where Γ_{ℓ} is a weighting matrix that satisfies $\Gamma_0 = I$ and $\Gamma_{\ell} = \text{diag}(|\mathbf{D}x_{\ell}| + \gamma \mathbf{I})^{-1}$ for $\ell \geq 1$ with $\gamma \geq 0$. The regularization matrix \mathbf{D} is given by the derivative of the TV norm and it is formulated as

$$D_{i,j} = \frac{\beta(2\delta_{i,j} - 1)l^{(i,j)}}{\max_{i,j} l^{(i,j)}} + \alpha\delta_{i,j}, \quad \delta_{i,j} = \begin{cases} 1, & \text{if } j = i, \\ 0, & \text{otherwise,} \end{cases} \quad (5.5)$$

where β determines the strength of TV penalty. Parameters α and γ ensure the invertibility of the matrices \mathbf{D} and Γ_ℓ so that the TV iteration does not diverge. $l^{(i,j)}$ represents the length of the edge between i^{th} and j^{th} voxel. The term $\max_{i,j} l^{(i,j)}$ refers to the maximum length of a voxel, and it can be regarded as the voxel width in the reconstruction. The first term of $\mathbf{D}_{i,j}$ in Eq. (5.5) penalizes the jumps over the voxel edges and the second one corresponds to the TV norm of \mathbf{x} . The CG method was used for the matrix inversion. If the iterations of CG converges, it minimizes the regularized objective function

$$F(x) = \|\mathbf{Ax} - \mathbf{p}\|_2^2 + 2\|\mathbf{Dx}\|_1, \quad (5.6)$$

which can be proven based on an alternating steepest descent iteration for L1-norm regularization assuming that \mathbf{D} is an invertible coordinate transform, for which the diagonal weights of \mathbf{D} need to be non-zero [81]. Note that Eq. (5.6) is differentiable anywhere but at one point.

In an attempt to prevent streaking artifacts from the data inconsistency at the tissue/metal boundaries, a sinogram filtering step was implemented after inpainting, prior to image reconstruction. In this step, dual-tree complex wavelet transform (DT-CWT) was used to hard-threshold the lowest 80 % of the wavelet coefficients of the sinogram. The DT-CWT has a higher directional sensitivity compared to conventional 2D wavelet transforms, which helps to preserve the edges in the image.

A multiresolution approach was used in P V to reconstruct the image details at different resolution levels. In the presence of noise, an image reconstructed with the finest resolution can result in severe artifacts due to the inconsistencies in the data. However, if the measurements are divided into coarse (i.e. larger voxel size) and fine (i.e. smaller voxel size) resolution levels, then the coarse level reconstruction imposes a regularization on the noise. The reconstruction of the coarse level measurement is therefore more reliable for the large structures in the image, while the finer resolution levels can be used to add detail into the image after filtering the noise. These properties make multiresolution a good choice for reconstruction of noisy measurements like low dose CT data with metallic objects. In P V, the measurement data was divided into separate resolution levels in the wavelet domain. The wavelet coefficients of each resolution level were filtered separately, decreasing the possibility of thresholding the relevant information out. It was observed that the filtering of the wavelet coefficients contributed to controlling the level of noise. More details on the use of the multiresolution approach is presented in PV.

5.3 Dataset preparation

It is a difficult task to develop a MAR method for experimental CT data due to different protocols in clinical practice and various physical causes of artifacts in the presence of a high density object in the FOV. Phantoms offer a simpler environment to develop and test new MAR methods. They also enable the modeling of different causes of metal artifacts individually, making it possible to assess the limitations of a MAR algorithm. As MAR methods developed in the context of this thesis focus on the head and neck region, a set of numerical 2D jaw phantoms was constructed based on the FORBILD jaw phantom of

Oliver Watzke¹. The jaw phantoms used in P I and P III are presented in Figure 5.1 with their respective noiseless sinograms.

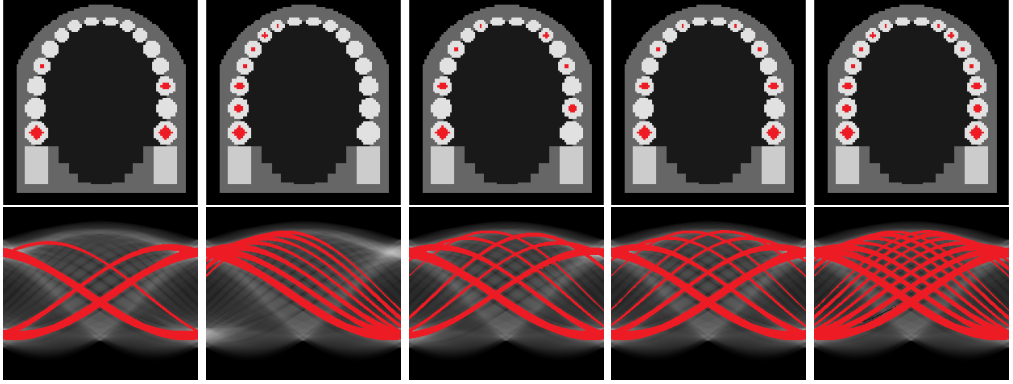


Figure 5.1: 2D numeric jaw phantoms and their sinograms with different size and amount of metals for evaluation of the MAR methods. Each image is 256×256 pixels, and each sinogram consists of 256 axial views and 288 projection angles. The masked sinograms after segmentation of metals were used as inputs for image reconstruction. The metals are marked in red.

Several criteria were taken into consideration for the construction of the phantoms. As the size, location and number of metallic implants can affect the MAR performance, metallic objects with different sizes and in various locations were embedded into the jaw phantom. The intensity values of the metallic objects (golden crown in this case), teeth, jaw bone, soft tissue and oral cavity were 19.3, 2.2, 2, 1 and 0.25, respectively, according to the ratio of the attenuation coefficients of these tissues. The effect of noise on the reconstruction methods was also investigated using noisy projection data.

Prior to reconstruction, the metallic regions were extracted from the projection data in P I and P III with a segmentation based on Otsu's thresholding, which separates the histogram of the data into two clusters with minimal intra-class variance of the mean value [82]. As it selects the threshold from the histogram of the data, Otsu's threshold is stable and automated. However, it can fail if the two clusters have very different sizes, which is the case in the segmentation of high density objects and anatomical structures. In such cases, the selected maximum mean value might be the valley of the histogram. This is why a segmentation approach, which performs multi-level thresholding and multiplies Otsu's threshold with empirical weights, was developed. These weighted thresholds are used to obtain a binary mask for the metals. Finally, the binary mask is back and re-projected to ensure the continuity of the high density objects on the projection data. In P V, perfect segmentation was assumed.

The proposed methods in P I(sMAPEM), P III(amMAPEM) and P V(MRTV-CG) were compared here using the phantom in Fig 5.2a here to allow a fair comparison. The reconstructed images were first evaluated visually and then quantitatively. The metallic regions in the masked projection data were filled via inpainting, prior to FBP and MRTV-CG reconstructions. For sMAPEM and MLEM, these gaps were assigned a fixed value of 1 in the projection data. In amMAPEM, the metallic regions were left as zeros in the projection data. The details of each reconstruction are given in Table 5.1.

¹<http://www.imp.uni-erlangen.de/forbild/deutsch/results/jaw/jaw.htm>

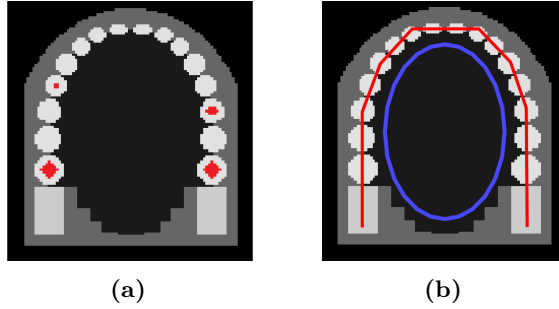


Figure 5.2: (a) The 2D jaw phantom with metals (256×256), (b) ROI that was used for the calculation of CoV (marked blue) and the line along which the line profiles were calculated (marked red), overlaid on the ground truth image.

Table 5.1: Details of the reconstruction methods

Method	Penalty function	Filter	Interpolation	β value	Stopping MSE
FBP	None	Hann	Bilinear	-	-
MLEM	None	None	Bilinear	0	10^{-6}
sMAPEM	MRP	None	Bilinear	$[0.01 \ 1]$	10^{-6}
amMAPEM	MRP	None	Bilinear	voxel-wise	10^{-6}
MRTV-CG	TV	CWT-DT	Bilinear	4	-

For quantitative analysis of the reconstructed images, CoV, SSIM, MSE and line profiles were used in this work. CoV values for the reconstructed images were calculated for a uniform region in the oral cavity (see blue ROI in Figure 5.2b). The line profiles were measured along the red line in Figure 5.2b.

5.4 Results

The results of all reconstruction methods developed for MAR are presented in Figure 5.3 for the 4-metal case, with (0.8 % zero-mean additive Gaussian noise) and without noise. Visual comparison of the noiseless reconstructions show that the MAP methods easily accommodate the gaps in the data. Both sMAPEM and amMAPEM preserve the metal/tissue boundaries and the images are almost artifact free. The dark bands along the metals are still visible in FBP despite the inpainting for larger metals. The dark streaks around the smaller metals in images reconstructed with MLEM make it difficult to identify the metal/tissue boundary.

When the noisy reconstructions are compared, the effect of noise is clear in images reconstructed with FBP. It can be observed that multiresolution LS solution (MRTV-CG) and both MAP methods perform well in the presence of noise, while preserving the anatomical shapes and borders. The edges of the jaw phantom are distorted in MLEM, and this distortion is slightly visible also in the sMAPEM and amMAPEM results. The noise is significantly reduced with amMAPEM, followed by sMAPEM. Note that the gaps from metals were not filled in amMAPEM in order to prevent interpolation errors during the rescaling of the projection data between resolution steps.

The results of quantitative analysis are shown in Table 5.2. The best values for each criterion are marked in bold. sMAPEM, in overall, performs the best for the noiseless

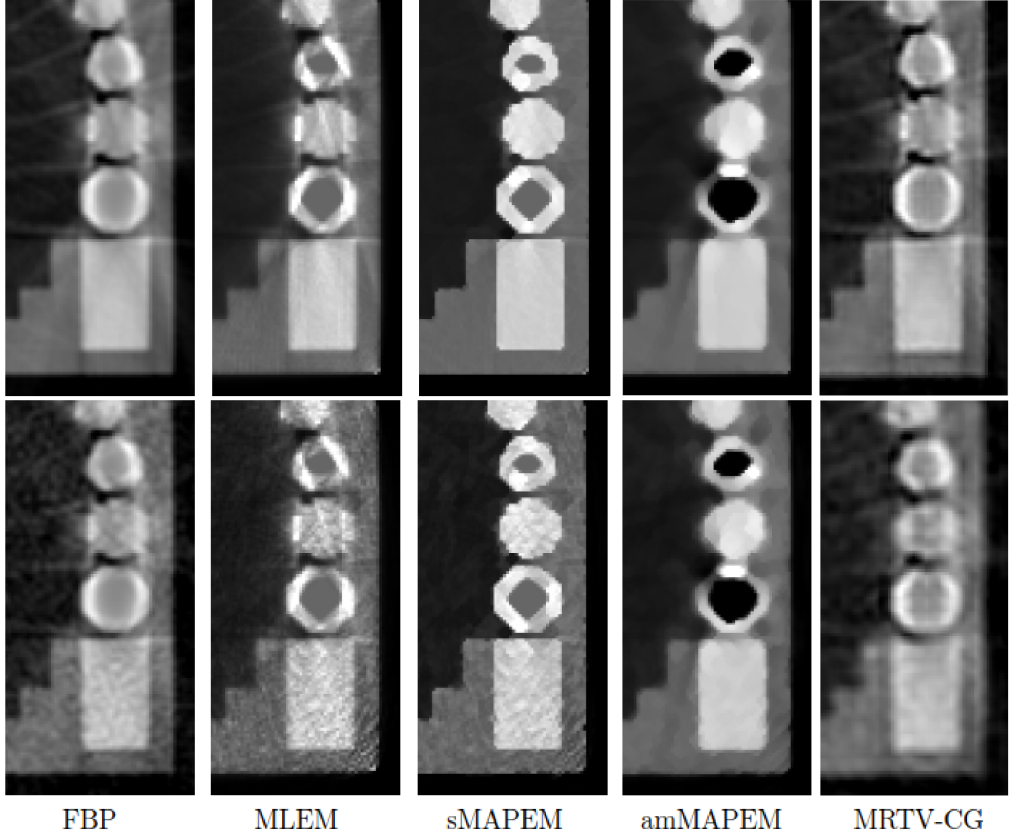


Figure 5.3: Reconstructed images with 4 metals. The 1st and 2nd rows present the results without and with additive Gaussian noise with standard deviation of 0.8% respectively. All image intensities are shown in the range of [0, 2.5].

and noisy reconstructions, followed by amMAPEM. Despite the successful noise reduction of amMAPEM (lowest CoV for noisy reconstructions), the SSIM and MSE values are worse than other ML methods due to the gaps left in the place of the metals in the image. MLEM has an overall performance close to MAP methods with similar SSIM values, but the CoV shows the difference between them in terms of noise reduction. Although MRTV-CG has the much lower SSIM than other MAP methods, its MSE performance is comparable. This is largely due to the hard-thresholding of the wavelet coefficients in MRTV-CG, which could be improved by other filtering approaches.

Table 5.2: Quantitative evaluation of results from Figure 5.3

	FBP	MLEM	sMAPEM	amMAPEM	MRTV-CG
SSIM without noise	0.59	0.86	0.95	0.89	0.44
SSIM with noise	0.36	0.69	0.72	0.66	0.36
CoV without noise	0.27	0.12	0.05	0.09	0.29
CoV with noise	0.39	0.18	0.15	0.11	0.30
MSE without noise ($\times 100$)	2.60	2.94	1.13	4.92	3.27
MSE with noise ($\times 100$)	2.96	3.43	1.50	4.94	3.59

A part of the line profiles of the images reconstructed from noiseless and noisy projections are presented in Figure 5.4. For the noiseless reconstructions, despite the compensation of the gaps via inpainting, FBP cannot recover the intensity values at the edges. MLEM also has a poor performance near the metals. The closest reconstruction to the ground truth at the metallic region is achieved by MRTV-CG, despite the slight overshoot in the other pixels of the line profiles. Both amMAPEM and sMAPEM recover the intensity values and preserve clear metal/tissue boundaries, but sMAPEM recovers the edges more accurately than amMAPEM. Among the noisy reconstructions, the line profile of amMAPEM clearly has less fluctuations, indicating a successful noise suppression. sMAPEM closely follows the line profile of amMAPEM, with slightly higher noise in the image. The use of Hann filter in FBP helps reducing the effect of noise in the reconstruction. Despite the noise penalization in both MAP methods, the line profiles are close to the ground truth and the metal/tissue boundaries are preserved. MLEM line profile is significantly affected by the noise, while MRTV-CG successfully suppresses most of the noise.

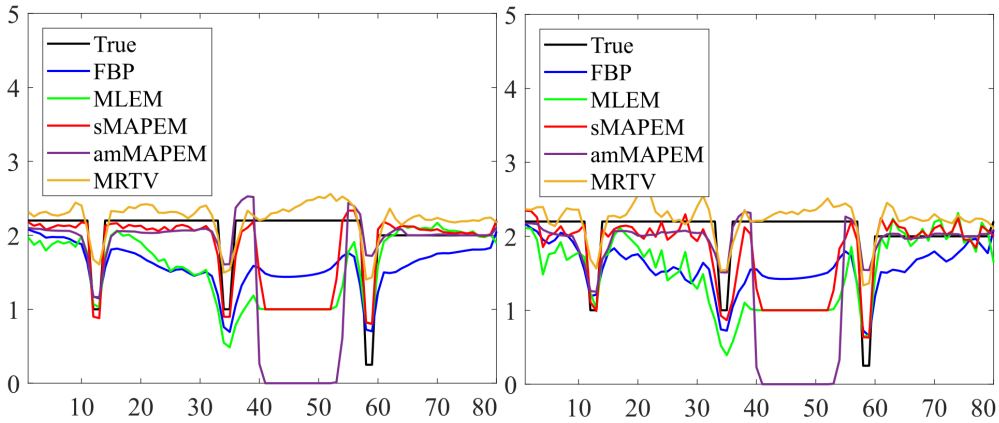


Figure 5.4: A section of the line profiles from (left) noiseless, and (right) noisy reconstructions. The metallic object is between 39th and 54th pixels.

5.5 Discussion

The MAR methods used in this thesis aim to (1) improve segmentation of high density materials, and (2) reduce the metal artifacts with penalized iterative reconstruction methods. The segmentation method based on multilevel Otsu's threshold allowed a more accurate representation of the metals compared to a single threshold. Although it was not implemented for the phantom, the segmentation approach would benefit from a pre-processing step to improve the contrast for the reconstruction of experimental data in order to preserve consistency of the projections.

In P I, the gaps were filled with a constant value, whereas for P III, we haven't replaced the intensity values of the metals. The goal in P I and P III was to reduce the artifacts around the metals and ensure a clear edge while suppressing the noise, which were achieved by both methods. Among the LS solutions implemented for MAR, Sidky *et al.* utilized the steepest descent algorithm to solve the inverse problem [52]. The steepest descent algorithm uses the opposite direction of the largest gradient among the gradients of each image dimension to select the direction of optimization, and it can get

stuck in a limit cycle, requiring an additional adaptive step size parameter to ensure convergence to a solution. We have chosen conjugate gradients in P V instead of the steepest descent because the number of iterations in CG can be used as a parameter to modify the behavior of the algorithm. The CG algorithm has also a faster convergence rate than steepest descent. It was also demonstrated in the images reconstructed with MRTV-CG in P V that combining projection completion and iterative reconstruction can be beneficial for MAR. To improve reconstruction accuracy of the projection data, a multiresolution decomposition was utilized in P V, similar to the work of Mehranian *et al.* in [66].

The filtering step of wavelet coefficients in P V had a similar motive to Zhao's work [67]. Using wavelet coefficients, one can distinguish different frequency components and filter the high frequency artifacts caused by metals and noise without disturbing the edges of the object. In this regard, the selection of wavelet is important. The 2D DT-CWT used in P V can recognize the orientation of the image fluctuations, which makes it is considerably less sensitive to the artifacts related to alteration or compression of the coefficients as compared to the wavelet transforms like orthogonal wavelet transforms or biorthogonal wavelets [67]. For comparison of the effects of the DT-CWT, Haar wavelets were used in P V. The reconstructed images after filtering with Haar wavelets resulted in voxelization of the images, whereas the DT-CWT recovered the details of the image successfully.

The physical processes can have an effect on the reconstruction as they change the interaction between the object and the X-rays. Although they were not included in P I and P III, a similar jaw phantom to Figure 5.1 was designed in P V, taking into account a polychromatic beam model when constructing the projection data. The phantom used in P V is depicted in Figure 5.5. The polychromatic data was included into the reconstruction to take the beam hardening effect into account in the forward model, improving the accuracy of the acquisition model. The energy dependent mass attenuation coefficients of gold, bone, hard tissue and soft tissue were obtained from the National Institute of Standards and Technology (NIST) database. The risk of committing "inverse crime" was avoided by first constructing the sinogram with 1024 pixels and then reconstructing it on a 512 pixel-grid. In doing so, it was ensured that the system matrix size was different for forward and backprojection, making the improvement of the reconstruction easier to evaluate. For modeling of the noise, Gaussian noise with standard deviation of 10 was used. Poisson measurements was also modeled with an initial emitted photon count of 10^5 , which can be considered standard for low-dose CT simulations [83].

In Figure 5.6, one can see the difference between the reconstructions of monochromatic and polychromatic projection data. In the polychromatic reconstruction, the shape of the metal in ROI 3 is recovered better. In terms of RMSE values, it was observed that the error with MRTV-CG decreased with polychromatic phantom thanks to better modeling of the acquisition system. On the other hand, the error from the MRTV results with filtering of the wavelet coefficients increased after implementing a polychromatic model. This increase in error was possibly due to the fact that more realistic modeling of the measurement system resulted in less blurring of the image, which in turn increased the mismatch between the individual voxels of the ground truth and the reconstructed ROI.

For even more realistic evaluation of the methods, the line tracing method could to be modified to include the effects of beam hardening and photon starvation, which are the prominent causes of metal artifacts in dental CT images. Furthermore, the assumption of parallel beam geometry was used for all forward and backprojections in

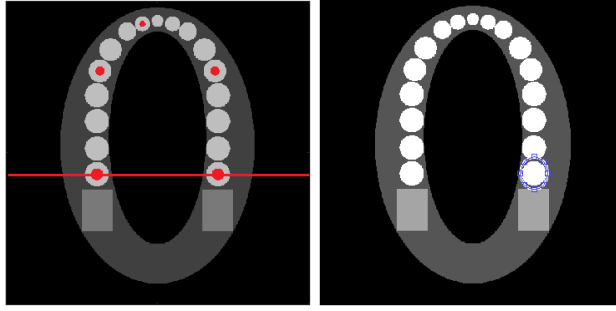


Figure 5.5: (left) 2D numeric jaw phantom used for polychromatic measurement model. The phantom image is 1024×1024 pixels, and its sinogram consists of 786 axial views and 256 projection angles covering 180 degrees. The metals are marked in red. The line profile was calculated along the red line. (right) The evaluated ROI with a metal, overlaid on the ground truth image.

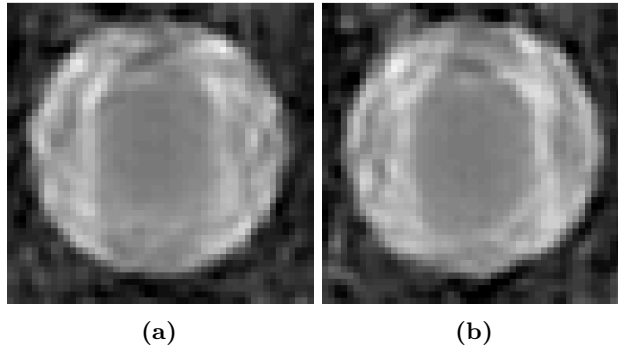


Figure 5.6: Reconstruction results in ROI with MRTV-CG with (a) monochromatic and (b) polychromatic projection data.

the proposed reconstruction methods. For a more realistic reconstruction, the cone or fan beam geometry could be incorporated into the projection model, similar to the work of [52]. This would incorporate the error that occurs once the cone-beam is rebinned into parallel-beam geometry upon reconstruction.

The reconstruction methods implemented for MAR accommodated the missing information in the projection data caused by the metals and successfully reduced the artifacts. The sMAPEM and amMAPEM preserved the borders around the metals clearly, which would be useful when the region of interest is close to the metallic object. If the intention is to reduce the effect of metals as much as possible in the reconstruction, then MRTV-CG would be a better choice. The MRP and TV prior were considered in this work due to their ability to distinguish between noise and edges. The implementation of such priors in the reconstruction will result in less blurring and more accurate images compared to noise suppression with various filters applied after the reconstruction. As a generalization of the proposed reconstructions, with high noise or sparse data (i.e. low dose CT or limited angle imaging), penalized iterative methods produce better images compared to MLEM and FBP. This is why MRP and TV priors were also used for reducing the limited angle artifacts and noise in PET data.

6 Artifact Reduction in PET: A Scanner Design

In order to control the growth rate of cancer, effective and affordable approaches are needed for its detection, diagnosis and treatment. According to 2013 statistics of the International Agency for Research on Cancer (IARC), breast cancer is the second most commonly diagnosed cancer type after lung cancer worldwide [84]. The same report shows that breast cancer is also the most common cause of cancer deaths among women in developed countries. Increasing numbers of occurrences and deaths due to breast cancer indicate the importance of screening for breast cancer in its early stages, which can be achieved non-invasively with good resolution imaging techniques such as mammography, magnetic resonance imaging (MRI) and PET. MRI is not recommended as a part of standard screening for breast cancer due to the high number of false positives and the probability of missing some cancers that could be detected by mammography. While structural information can be obtained from mammography, PET has a high potential in detecting recurrences of cancer cases as well as selection and monitoring of cancer therapy due to its functional imaging capability. PET is also useful for imaging radiodense or fibrocystic breasts, where mammography results can be inconclusive. As more radiotracers became readily available in the world, PET has become a more accessible alternative for imaging. Unfortunately, the insufficient spatial resolution of a whole-body PET (around 4–6 mm) has prevented detection of small, early stage cancer lesions [85]. The low affordability due to high cost of PET also prevented its wide spread use. As size of equipment and use of space are important factors in developing regions and in small clinics, the bulky size of whole-body PETs has also contributed to the demand for the search for alternative PET solutions [86]. All these limitations of conventional whole-body PET have led to the development of organ-specific PET scanners, which can provide higher sensitivity and better spatial resolution (1–2 mm) than whole-body PET [85]. AvanTomography was proposed as a highly sensitive, affordable PET demonstrator with a portable and modular configuration for breast imaging.

6.1 Review of previous work

Positron emission mammography (PEM) offers high sensitivity due to its proximity to the breast. A small FOV, which is needed for high sensitivity, is achieved with either a dual-plate configuration used in standing/sitting position, similar to other two plate PEM scanners or with ring scanners that are used in prone position [87]. PEM with 2 opposing plates offers flexibility over the positioning of the patient's breast, as well as the ability to accommodate different breast sizes over the ring type scanners (i.e. dbPET-MAMMI). This configuration enables the visualization of axilla and the lesions near the chest wall

and the possibility of incorporation with biopsy operations. Despite having lower contrast and signal-to-noise ratio than ring scanners, dual-panel design results in lower noise and a simple assembly without complicating the structure with rotation and center of rotation corrections [85, 86].

Since the approval of PEM technology by Food and Drug Administration (FDA) in 2003 for pre-surgical planning, evaluation of axillary lymph nodes, monitoring response to chemotherapy and to look for recurrent diseases, several PEM scanners have been proposed [88]. Although many PEM scanners are under ongoing research in universities, only few are currently available on the market [85, 87, 89]. While this might be interpreted as lack of commercialization efforts, it also points towards a need for optimizing the scanner structures for commercial use. A detailed account of the current dedicated breast imaging devices, which includes PEM and gamma cameras, can be found in [85, 90]. Some properties of available PEM scanners are given in Table 6.1 [85].

Table 6.1: Coincidence-detection technologies applied to breast imaging, from [85].

	Manufacturer	Geometry	FOV	Energy resolution	Spatial resolution
PEM-FLEX	CMR Naviscan Corporation, San Diego, CA	2-panel	$24 \times 24 \times 16.4 \text{ cm}^3$	2.3 % at 511 keV	2.5 mm FWHM (in-plane), 6-9 mm cross planes
Clear-PEM	Crystal Clear Collaboration, CERN	2-panel	$16 \times 16 \times 18 \text{ cm}^3$	16 % at 511 keV	1.4 mm at the center of the FOV
dbPET-MAMMI	Oncovision, Valencia, Spain	Ring	17 cm diameter, 4 cm axial FOV	-	1.6 mm (FWHM in transverse FOV), 2.7 mm at the edges of the FOV
C-shaped PEM [91]	Shimadzu Corporation, Kyoto, Japan	Ring	22.8 cm diameter, and an axial extent of 10.5 cm axial FOV	16.9 %	0.7-1.2 mm

One of the challenges in breast imaging is the trade-off between system sensitivity and spatial resolution in conventional PET scanners. In order to achieve an accurate level of detail from a small object like breast, both sensitivity and resolution should be as good as possible. The use of long and narrow crystals with a small diameter increases the sensitivity, but it worsens the spatial resolution [92]. The degradation of the spatial resolution occurs at the reconstruction step, where the center of the crystal is taken as annihilation point. In longer crystals, this leads to the mis-positioning of the reconstructed LORs. Wrongly reconstructed LORs cause parallax error, which is the estimation error that occurs when incident photons at oblique angles cannot be measured. Parallax error increases proportionally with the distance from the center of the FOV in radial direction. The depth-of-interaction (DOI) information helps decrease parallax error, improving the spatial resolution, even at the center of the FOV. Without the DOI information, it is unlikely to achieve a good sensitivity and a good spatial resolution, which makes accurate determination of DOI very important for PEM. Another alternative is the phoswitch configuration, where two different crystals with different light decay constants are used instead of one long crystal [93]. This solution gives two different DOI points at the center of each crystal, thus decreasing the parallax error. It is also possible to use a dual-sided readout from the scintillating crystals, in which the ratio of light between two detectors reading the same crystal helps to determine the DOI [94]. TOF information can aid in more accurate determination of the annihilation points as well, but its implementation

is still expensive for its wide clinical application in small scanners. All these methods are beneficial to achieve more accurate DOI points, but all use the same scanner crystal configuration structure, therefore they can't eliminate the parallax error.

Axial PET (AX-PET) design uses axially oriented crystals to decouple the sensitivity from the spatial resolution [95]. The scintillating crystal layers in AX-PET are interleaved with an array of plastic wavelength shifting (WLS) strips, placed orthogonal to the crystals. When a photon deposits its energy in the crystal, a correlated amount of light is isotropically emitted in a different wavelength. Emitted light from the crystal is captured by WLS strips. The signals from strips and crystals are detected by individually coupled photodetectors. This information is used to determine the 3D coordinate of the photon interaction. Position of the crystal provides the hit location in x and y (transaxial) directions, whereas the z (axial) coordinate is calculated using the position of active strips. Intersection point of a crystal and a WLS strip results in the exact 3D coordinate of the annihilation. The transaxial and axial resolutions are determined by the cross-sections of scintillating crystals and WLSs respectively. The sensitivity depends on the type of the scintillating crystals as well as the number of crystal layers used.

6.2 Methods

AvanTomography demonstrator proposed in P II is a prototype for a highly sensitive PET scanner for breast screening. Its design was based on the work of the Axial PET (AX-PET) project in CERN [95], which was developed primarily as a full ring scanner for brain or small animal imaging. Its application in breast imaging brings some distinct advantages over the whole-body PET and other PEM scanners. Firstly, as a type of PEM, it has a higher sensitivity compared to whole-body PET due to its proximity to the breast. Secondly, its axially oriented crystals eliminates parallax error and provide an exact location of the positron annihilation. P II presents the physical measurement setup of a 6-module scanner and the initial measurement results on its performance. The configuration of individual modules and the AvanTomography demonstrator is shown in Figure 6.1.

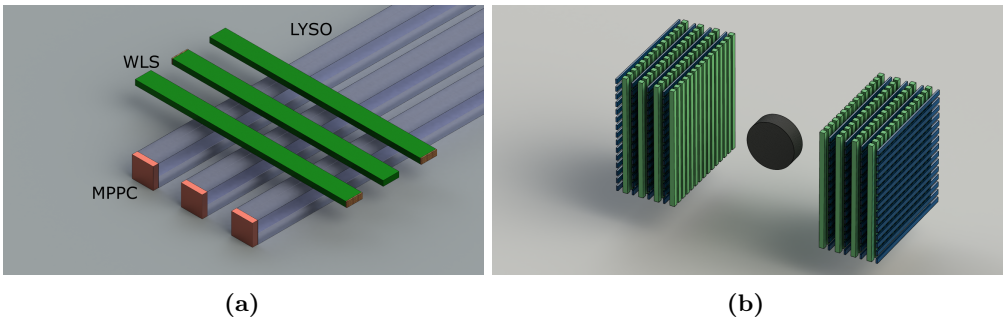


Figure 6.1: (a) Crystal (LYSO type), plastic wavelength shifter (WLS) strip and photodetector (MPPC@Hamamatsu Photonics, Japan) positioning within the AvanTomography modules, (b) Placement of the modules in the AvanTomography demonstrator. A point-like source is placed at the center of the FOV in the experimental setup.

The construction of the modules and associated electronics are explained in P II. The initial measurements from the demonstrator aimed at characterization of the constructed modules such as detection efficiency and sensitivity as well as energy calibration curves.

6.3 Experimental setup

For the experiments, a 6-module prototype was constructed in P II. Each module was designed to be electronically and mechanically independent, connected to the computer via a USB cable for data processing. The hardware design for each module consisted of a bias circuit, a sensor board, and a temperature compensation unit. P II explains the electronic design of the individual modules in detail. One of the important considerations in this design was to ensure that the bandwidth of the transmission was sufficient enough to handle the high data load from individual readings without data overflow. A simple user interface (see Figure 4 in P II) was designed to check the activity level of each crystal and WLS strip. A point-like ^{22}Na with 675 kBq activity within a polymethyl methacrylate (PMMA) casing was used for the experiments. The modules were placed so that the distance from the source to the closest module was 11 cm. For coincidence sorting a time window of 10 ns, and an energy window of 350–650 keV were used. The processing of the measured data from the detection by the photodetectors to digital processing in the computer is also described in detail in P II.

6.4 Simulation setup

The prototype design was also assessed using Monte Carlo simulations in Gate [96]. The simulations in Gate were based on the Monte Carlo simulations of the AX-PET group [97]. The simulated detector model comprised of separate modules consisting of LYSO crystals and WLS strips. In order to simulate the WLS strips efficiently, an analytical model of light transport within the crystals and strips was implemented into Gate simulation tool. The axial coordinate of a hit was determined from the response of the row of strips with 1.5 mm resolution. Due to the axial orientation of the crystals, the standard Gate packages could not be used. To ensure the event positioning of the simulations would match the physical model, the digitizer package was modified so that when the photons hit the crystal, the axial coordinate of the hit would be preserved instead of being merged. The digitization modules for the x - and y -coordinates were also changed in order to position the hit at the center of the axially oriented crystals. In the simulation, the included physical processes were photoelectric effect, Compton scattering, Rayleigh scattering and gamma conversion for photons, multiple scattering, ionization, bremsstrahlung and annihilation for electrons and positrons, and atom de-excitation. These simulations were used to measure the performance parameters such as sensitivity, energy and spatial resolution, count rate, noise equivalent count rate and scatter fraction. Details of the simulated model can be found in [96].

The initial simulations were conducted with a point source to determine the spatial resolution of the system. The list-mode data collected from the simulation was reconstructed with a voxel resolution of 0.5 mm^3 using MLEM. Afterwards, a cylindrical phantom was used to evaluate the performance of the scanner structure in a controlled environment. The phantom consisted of hot and cold regions filled with water, having the total activity of 1.5 MBq. The larger cylinder had a diameter of 6 cm, whereas the small cylinders were 2 cm in diameter and placed 1 cm away from the center of the larger cylinder (see Figure 6.2a). The list-mode data obtained from the simulations were reconstructed with MLEM using 1 mm^3 voxel size. Only the true coincidence events were considered in the reconstruction. As DOI was calculated from the WLS and crystals, no TOF information was considered in the reconstruction.

6.5 Results

Preliminary experiments with the constructed modules, also presented in P II, resulted in an energy resolution of around 14% FWHM in the sum of crystals. The recorded photon attenuation values were 51% at the first layer, 32% at the second layer and 17% at the third layer. The results of the experiments with the point source are presented in Figures 6–9 in P II. Measured sensitivity was calculated as 0.00355% from an average of 5 measurements.

From the simulations, it was observed that the photoelectric events detected by the modules decreased exponentially when the distance from the source increased. The effective attenuation length has been calculated by counting the photoelectric at each crystal layer (3 modules, each with two layers of LYSOs, leading to a total of 6 crystal layers). According to the simulations of the photopeak statistics, 54% of the photons were stopped at the first module. Attenuations in second and third layers of the simulations were 30% and 16% respectively. The reconstruction results from the point source simulations indicated a transaxial resolution of 2.1 mm, which was calculated from the mean of resolutions in x (2.5 mm) and y (1.7 mm) directions. According to the simulation results, total sensitivity of the system was 502 cps/MBq (0.05 %). Axial resolution (z direction) was calculated as 0.66 mm for 0.5 mm^3 sampling size. The energy resolution obtained from the simulations was 11.9%. In comparison, the AX-PET scanner resulted in 1.57 mm transaxial and 0.65 mm axial resolution with an energy resolution of 12.8% [98, 99]. The simulated phantom was reconstructed using 5M true counts, results of which are depicted in Figure 6.2. No data correction was applied.

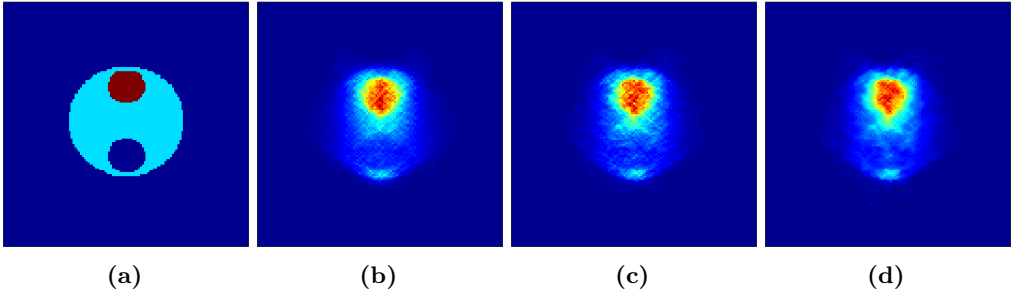


Figure 6.2: (a) The ground truth image, (b) reconstructed image with MLEM after 8 iterations, (c) MAP-MRP with $\beta = 0.3$ after 9 iterations, (d) MAP-TV with $\beta = 0.05$ after 9 iterations.

6.6 Discussion

Avantomography provides a PEM scanner alternative for low-dose PET imaging in breast screening based on preliminary results. The simulations indicate a high sensitivity and comparable spatial resolution with other PEM scanners presented in Table 6.1. It also achieves a comparable energy resolution to Clear-PEM and C-shaped PEM.

AvanTomography prevents the parallax error upon reconstruction without any expensive hardware required for TOF or phoswitch. Without the parallax error, the overall uncertainty in the reconstructions decrease significantly for small FOVs. In this scanner, the crystal length determines the scanner width, i.e. the size of the FOV in the transaxial direction. Use of longer crystals can increase the scanner width, providing a larger FOV in the axial direction as well as increasing the angular coverage. The increased scanner

FOV also improves the sensitivity. When a full plate PEM configuration with 16 modules in each plate and a FOV of 5 cm in diameter was simulated, the sensitivity increased up to 2%, indicating that a larger scanner is crucial to achieve a good sensitivity comparable to commercial scanners. It should be noted, however, that longer crystals would widen the FWHM of the 511 keV peak, from which the energy resolution is calculated. This is due to the decrease in the detected number of photons with longer crystals. Worsening of the energy resolution for longer crystals creates a limit for the crystal length to be used in a PET application. For a good energy resolution, it is important to be able to distinguish the photoelectric peak from the Compton region. In order to ensure the separability of the Compton and 511 keV peaks, the crystal length should not exceed 200 mm. Considering the other FOVs presented in Table 6.1, 15 cm-long crystals would be needed to ensure sufficient counts and full coverage of the breast.

Separate bias boards, coupled to the temperature compensation units for individual modules might be required in the future to ensure the temperature compensation of channels with high count rates. Even though individual temperature compensation circuitry and the use of temperature compensation coefficient in software would improve the results in the future, the measurement system still provided reliable results for 2-hour measurements with the radioactive source.

In the simulations, the sensitivity was found to be almost 10 times higher than the experimental sensitivity. The difference arises from the fact that not all the properties of the system were modeled. The experimental system has added dead time from the intrinsic activity counts from Lutetium, cross-talk within a layer of crystals, and non-instant data transfer times, which were not taken into consideration in the simulations. Furthermore, in the measurement setup, some of the counts were lost within the data acquisition system. This loss in coincidence counts was due to the fact that in the data recording, only one LYSO event is registered with the corresponding charge. However, if there are two or more crystals active at the same time, since both are registered with the same charge value, it is currently not possible to differentiate between the high and low energy photons. Therefore energy gating on this data eliminates possible coincidences. Handling of these multiples in the data acquisition is required to achieve higher sensitivity. Furthermore, multiple hits within the same layer being hit by the same photon constituted a large part of the measurement data. However, their percentage in the simulated data was much lower. The abovementioned differences between the simulations and experimental data, as well as the data acquisition system imperfections are most likely the cause of the difference in sensitivity values.

The reconstruction results from the simulations indicate that despite a slight elongation in the background, the hot and cold regions preserve their shapes. Even the elongation in the background is decreased in TV and MRP approaches compared to MLEM due to the median filtering in MRP and differentiation in TV. The accuracy of the phantom shape also confirms that the modifications in Gate packages have been successful. An optimized binning size and data correction with a normalization map from the geometric scanner configuration could be used for better reconstruction results. In overall, the AvanTomography demonstrator showed promising results for a PEM scanner, with sufficient resolution and sensitivity for cancer detection in breast. It could provide a low cost and accurate alternative for breast screening with an optimized structure of its modules. With its independent modular structure, it is also possible to design other organ-specific scanners, which target visualization of a specific region rather than whole body.

7 Artifact Reduction in PET: A Reconstruction Method

7.1 Review of previous work

In proton therapy, proton beam can deliver a high dose of radiation to the tumor with minimal effect on the tissues nearby. However, if the dose is not delivered to the correct location, healthy tissue can be damaged. Imaging of the secondary irradiation in proton therapy using PET helps adjusting the treatment plan. There are several options to combine PET imaging with proton therapy: (1) in-room PET, in which patient is transferred to a PET scanner in the same room shortly after proton therapy, (2) off-line PET in which patient is transferred to a PET scanner nearby after proton therapy with several minutes delay, and (3) in-beam PET, in which the PET data is acquired during the treatment. As the secondary radiation from proton therapy produces a high percentage of the short-lived isotopes, it is important to minimize the time between the treatment and PET imaging. In P IV, we focus on the reconstruction of simulated PET data acquired during proton therapy. The in-beam PET data is difficult to reconstruct accurately with conventional FBP or MLEM methods for two reasons. First issue is the low count rate of the recorded PET isotopes during proton therapy, which makes the data very noisy. Secondly, generally a partial ring configuration is required for the beam to pass through the PET scanner, thus limiting the acquisition angles and decreasing count rates further. A typical problem of limited angle reconstruction without penalization is elongation of the object orthogonal to the beam direction [100]. Several papers have been published with suggestions on how to use reconstruction methods to reduce the elongation of in-beam PET data [62, 101–103]. A more detailed account of the published work can be found in P IV.

7.2 Methods

P IV proposes a MAPEM reconstruction method with MRP in order to solve the problems of in-beam PET data. The incorporation of MRP penalizes the noise in the image without blurring the edges. This is a major advantage of MRP as in-vivo dose delivery verification requires accurate determination of the edges. Otherwise, the range of the proton beam can be misinterpreted, potentially harming the organs/tissues sensitive to radiation. MAPEM with MRP was previously implemented by [104] with histogrammed data, in which MAPEM with MRP successfully reconstructed histogrammed data from real measurements. Similarly, the limited angle issue was tackled in P IV with the reconstruction of list mode data instead of histogramming the data into sinograms (see Chapter 3.4 for the comparison of list mode data and histogramming). TOF information

was incorporated into the reconstruction to decrease the elongation in the reconstructed image. The reconstruction of image x_j for iteration $k + 1$ with MAPEM using the OSL scheme is written as

$$x_j^{k+1} = \frac{x_j^k}{\sum_{i=1}^I a_{ij} + \beta \frac{\partial U(x)}{\partial x_j} \big|_{x_j=x_j^k}} \sum_{l=1}^L \sum_{h \in S_l} a_{ihj} \frac{1}{\sum_{j=1}^J a_{ihj} x_j^{k,l}}, \quad (7.1)$$

where β is the hyperparameter that determines the strength of penalization. β can take values in the range of $[0, 1]$ because the non-negativity constraint of the reconstruction dictates that the maximum of the hyperparameter cannot exceed the maximum of the normalized sensitivity image $\sum_{i=1}^I a_{ij}$. The difference of Eq. (7.1) from Eq. (3.29) is the use of subsets in the reconstruction of the data. The recorded counts are divided into L subsets ($l = 1, 2, \dots, L$), each subset containing h LORs. The h LORs within each subset are backprojected once. Then, these backprojected images from all the subsets are summed and used to update x_j^k . Processing of list-mode data using subsets speeds up the reconstruction L times.

The MRP and TV priors were selected as penalty terms for the reconstruction of data in P IV. In the implementation of reconstruction with MRP, the derivative of the energy function is replaced with the difference between the j^{th} voxel of the image x at iteration k , x_j , and the median of the neighborhood centered at voxel j , M_j , resulting in the term $\frac{x_j^k - M_j}{M_j}$. In TV, the penalty term is replaced with the derivative of the $l1$ norm of the TV function. Note that both priors were applied over 3D data.

7.3 Dataset preparation

A geometrical and a realistic phantoms were simulated for testing the reconstruction methods for in-beam PET data. In order to test the performance of the reconstruction methods in controlled environments, both phantoms were simulated via Monte Carlo simulation tool Gate [105]. For both phantoms, the reconstructions of partial ring configurations (240 and 180 degrees coverage) were compared with the reconstructions from the full ring data. CRT for standard for PET scanners was taken as 400 ps (LOR length of 6 cm), and 200 ps (LOR length of 3 cm) was considered as the best-case scenario. Details of both simple and realistic phantom simulations are presented in Table 7.1.

Table 7.1: Details of phantoms used in for reconstruction of in-beam PET data

Phantom	Scan time	Total activity	Counts (full ring)	Simulated isotopes
Geometrical phantom	60s	4 MBq	0.3 million	^{15}O
Realistic phantom	120s	5.9 MBq	4.5 million	^{10}C , ^{11}C , ^{13}N , ^{14}O , ^{15}O , ^{30}P , ^{38}K

For the geometrical phantom, a 12 cm-long polyethylene nonvoxelized phantom with 10 cm radius was constructed with 1 kBq/cm³ activity. A high activity (hot) cylinder was inserted into it with an activity level of 4 kBq/cm³. Another cylinder was inserted into the larger cylinder, filled with air (see P IV for details of the simulated PET scanner). The size of the reconstructed images for the geometrical phantom was $81 \times 81 \times 45$ voxels in x , y and z dimensions.

For the realistic patient case, the simulated treatment plan in Geant4 Simulation Toolkit for irradiation of a tumor near the spine and the corresponding CT data was provided by the Department of Radiotherapy of the University Medical Centre in Groningen [106]. The isotopes collected from this simulation was used for Gate simulations of the PET scanner. Three proton fields were delivered with proton beam angles of $+40$, 0 and -40 degrees with respect to the x axis in Figure 7.1b. The reconstructed image size for the realistic patient phantom was $125 \times 88 \times 110$ voxels in x , y and z dimensions. Both phantoms are shown in Figure 7.1 with voxel size of $4 \times 4 \times 4 \text{ mm}^3$ for the reconstruction of both phantoms. Such large voxel sizes helps in reducing the statistical noise in the images as well as decreasing the amount of averaging required for a reliable analysis of the edges. All data corrections were implemented within the reconstruction algorithm in order to preserve the Poisson characteristic of the measurement system.

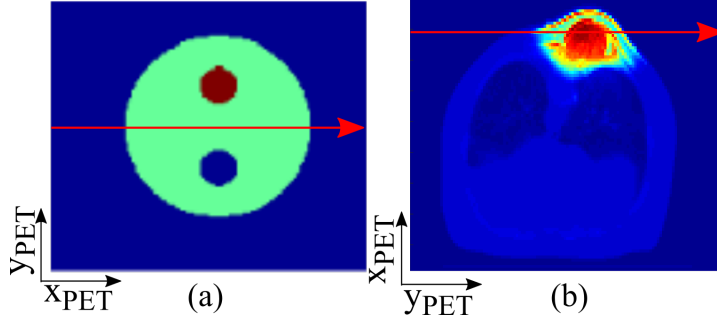


Figure 7.1: The transverse views of (a) geometrical and (b) realistic phantoms

Normalization correction was applied to both geometrical and realistic phantoms. For the geometrical phantom, the sensitivity matrix was calculated with a separate Gate simulation. For this simulation, the same scanner configuration for the geometrical phantom was used, but the FOV was defined as a vacuum with uniform activity and no object. The detector responses were recorded for sufficiently large number of events. Each recorded LOR was backprojected and summed to form the normalization coefficient for each voxel. The normalization correction is represented with the term $\sum_{i=1}^I a_{ij}$ in Eq. (7.1). For the realistic phantom, the sensitivity matrix was computed analytically by backprojecting one count per LOR.

Attenuation correction factors (ACFs) for both geometrical and realistic phantoms were constructed by calculating the attenuation of each LOR on-the-fly during the backprojection. All the LORs were multiplied with their corresponding ACF. For the realistic phantom, the HU values of the CT image from the patient were scaled using bilinear interpolation to calculate the attenuation values [107]. Randoms were found to be small enough (approx. 6% of total counts) due to low activity levels, therefore randoms corrections was not implemented into the reconstruction. For the simplicity of reconstruction, scattered counts were also excluded from the list mode data prior to reconstruction.

7.4 Results

7.4.1 Geometrical phantom results

The optimal hyperparameter values (β) for TV prior and MRP were selected according to the NMI values of the reconstructed images. Tested β values were 0.01, 0.04, 0.08, 0.15,

0.3, 0.4, 0.6 and 0.8. The NMI values calculated for different β are shown in Figure 7.2 for a full ring configuration with 400 ps CRT. For MLEM, β is zero and it is shown in Figure 7.2b only for comparison.

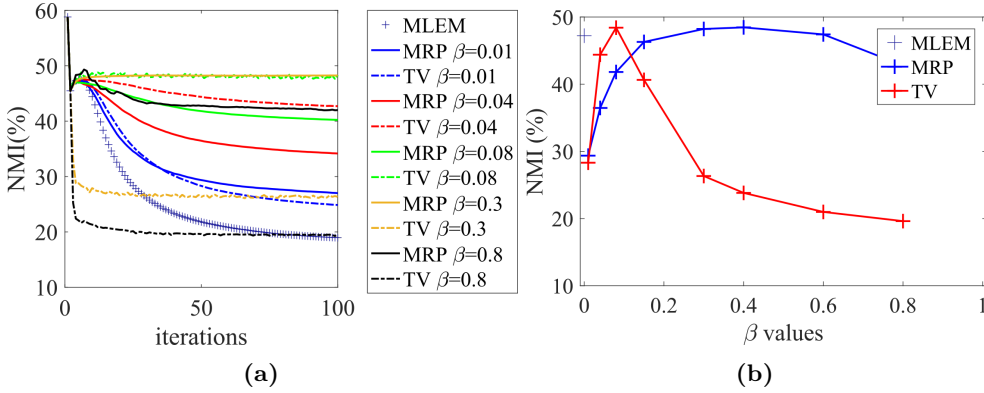


Figure 7.2: (a) NMI values calculated from the 3D volume of the geometrical phantom for full ring configuration with 400 ps CRT over 100 iterations. (b) The mean NMI values at 50 iterations for various β values. MLEM was stopped after 7 iterations. The voxel size is $4 \times 4 \times 4$ mm³.

The 2D slices of reconstructions with the tested β can be seen in Figure 7.3. For MAPEM-MRP, β greater than 0.3 improves the contrast upon visual inspection (see Figure 7.3), but the NMI values in Figure 7.2 are slightly lower for large β due to blurring. For MAPEM-TV the β value of 0.08 results in the highest contrast and best noise reduction. According to the results in Figure 7.2 and Figure 7.3, the optimal hyperparameters for MRP and TV prior were selected as 0.3 and 0.08 respectively. The NMI values from the partial ring configuration (2/3 ring) for the phantom are presented in P IV.

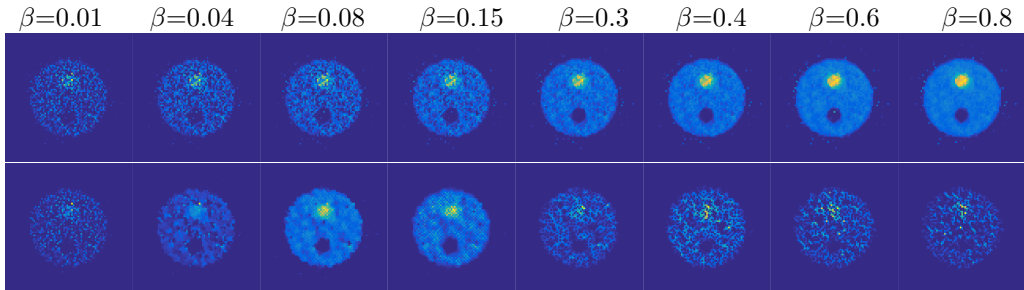


Figure 7.3: 1st and 2nd rows show the reconstructed images from the geometrical phantom with MRP and TV priors respectively after 50 iterations using various β values. Images depict the central slices in z direction, reconstructed using full ring configuration with CRT of 400 ps.

The reconstructed images from the geometrical phantom are shown in Figure 7.4. The elongation is visible for reconstructions of partial rings with MLEM and MAPEM-TV, especially with 400 ps CRT. A better CRT decreases the elongation significantly in 2/3 ring reconstructions for these methods, but it is not enough to compensate for the elongation in the 1/2 ring configuration. Checkerboard artifacts are observed in the images reconstructed with MAPEM-TV. Some artifacts are visible outside the phantom with MAPEM-MRP, which are more pronounced in the MAPEM-MRP results from the

partial ring scanners. On the other hand, almost no elongation is visible in any of the MAPEM-MRP results.

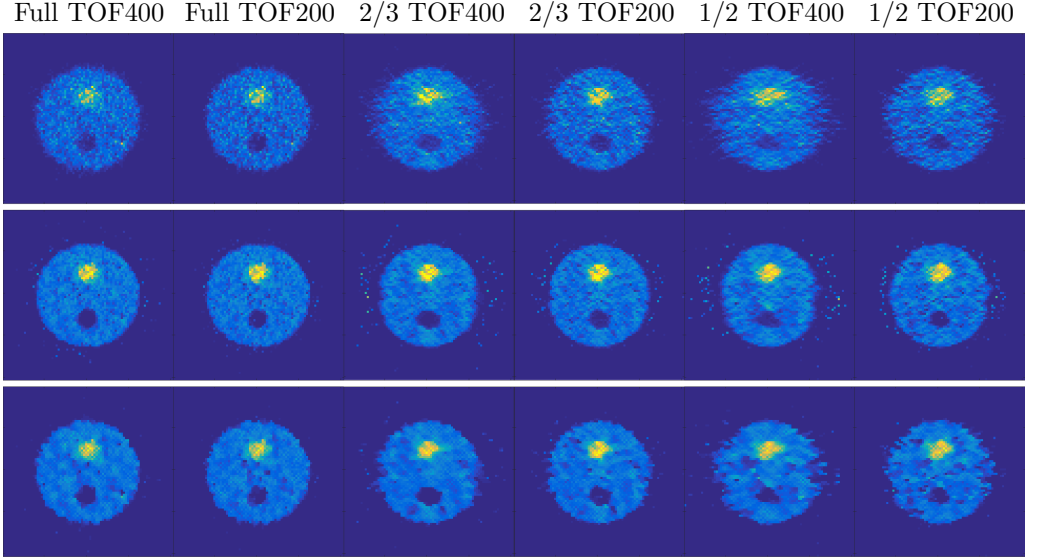


Figure 7.4: Reconstructed images for the geometrical phantom. Rows 1, 2 and 3 show the results from MLEM, MAPEM-MRP and MAPEM-TV respectively. Images here are the central slice in z direction.

The accuracy of the edges in the reconstructed images were evaluated with the 50% point of the maximum along the sigmoid functions fitted to the line profiles. The line profiles were calculated along the red line on the geometrical phantom in Figure 7.1. The 50% value is denoted with h_0 in Eq. (4.8). The sigmoid functions were fitted to the normalized line profiles over the central slice and its two closest neighbors along the z direction. The h_0 and slope (b) values are presented in Table 1 of P IV, in which all full ring reconstructions result in h_0 s close to the h_0 of the emission map. Although the steepest slope for the full ring reconstruction is achieved by MAPEM-TV, the slopes of the partial ring reconstructions are significantly steeper for MAPEM-MRP than MAPEM-TV and MLEM.

As a measure of noise reduction in the reconstructed images, CoV was calculated over the volume of the large, background cylinder with uniform activity. The regions at the vicinity of low and high activity cylinders were excluded from the VOI to ensure the uniformity of the radioactivity concentration. Lower CoV indicates less noise in the reconstructed images, while large CoV is a sign of large variation between pixels. The CoVs for the reconstructed images are presented in Table 1 in P IV. It can be observed that MLEM has the highest levels of CoV despite the early stopping after 7 iterations. Both MAP methods have significantly lower CoVs than MLEM, irrespective of the ring configuration or the TOF. The CoV values of MRP are generally lower than that of TV, as well as having smaller variability between slices.

7.4.2 Realistic phantom results

To find the optimal hyperparameter for the realistic phantom, β values of 0.01, 0.02, 0.05, 0.07, 0.3, 0.4, 0.6 and 0.8 were tested. The NMI values are presented in Figure 7.5. The

NMI values follow a similar trend as the NMIs of the geometrical phantom, in which MRP retains the NMI values well over 40 % for all β , whereas NMI values of TV prior peak around $\beta = 0.02$ and then rapidly decrease for larger β . Based on the NMI results in Figure 7.5, optimal β values for TV and MRP were chosen as 0.02 and 0.3, respectively.

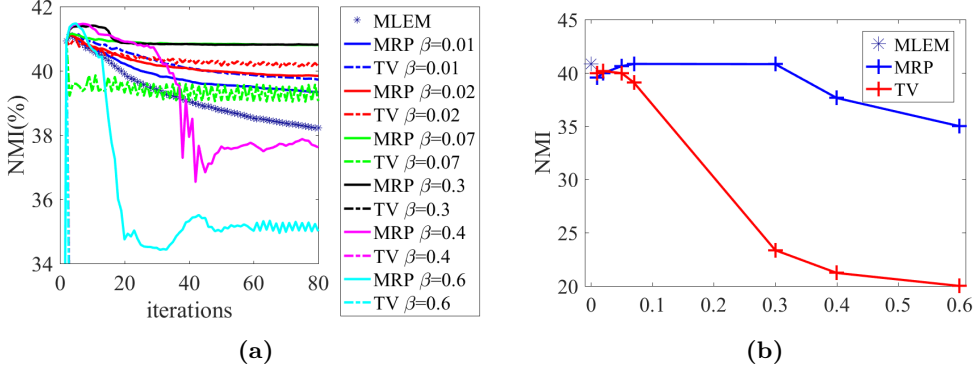


Figure 7.5: (a) NMI values calculated from the 3D volume of the realistic phantom for full ring configuration with 400 ps CRT over 100 iterations. (b) The mean NMI values at 50 iterations for various β values. The voxel size is $4 \times 4 \times 4 \text{ mm}^3$.

The 2D slices from the reconstructed images are also shown in Figure 7.6. MRP is effective at noise suppression with β around and greater than 0.3, below which the prior is not strong enough to reduce the noise in the images. Larger β than 0.3 only causes slight blurring in the images reconstructed with MAPEM-MRP in Figure 7.6. For TV, the opposite is valid; smaller β than 0.02 effectively suppresses the noise in the images, but higher values cause checkerboard artifacts, also called staircasing artifacts in [51].

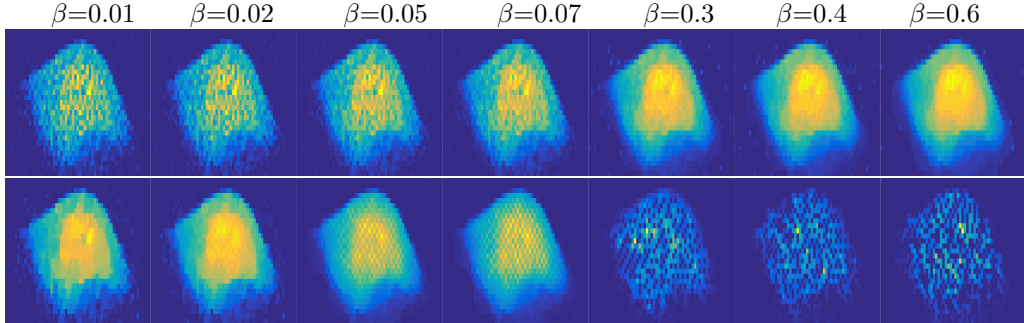


Figure 7.6: 1st and 2nd rows show the reconstructed images from the realistic phantom with MRP and TV priors respectively after 50 iterations using various β values. Images depict the central slices in z direction, reconstructed using full ring configuration with CRT of 400 ps.

The reconstructed images from the realistic patient phantom are depicted in Figure 7.7. They were compared with the emission image, which is the map of the radioactivity distribution directly obtained from the simulation of the PET isotopes. The results show an elongation in the direction of the partial ring detectors for MLEM with 400 ps CRT, especially for the 1/2 ring. The edges of MAP reconstructions are sharper compared to MLEM. Despite some activity outside the emission area in MRP, the overall visual inspection indicates better reconstruction of the low activity areas close to the edges of the irradiated area.

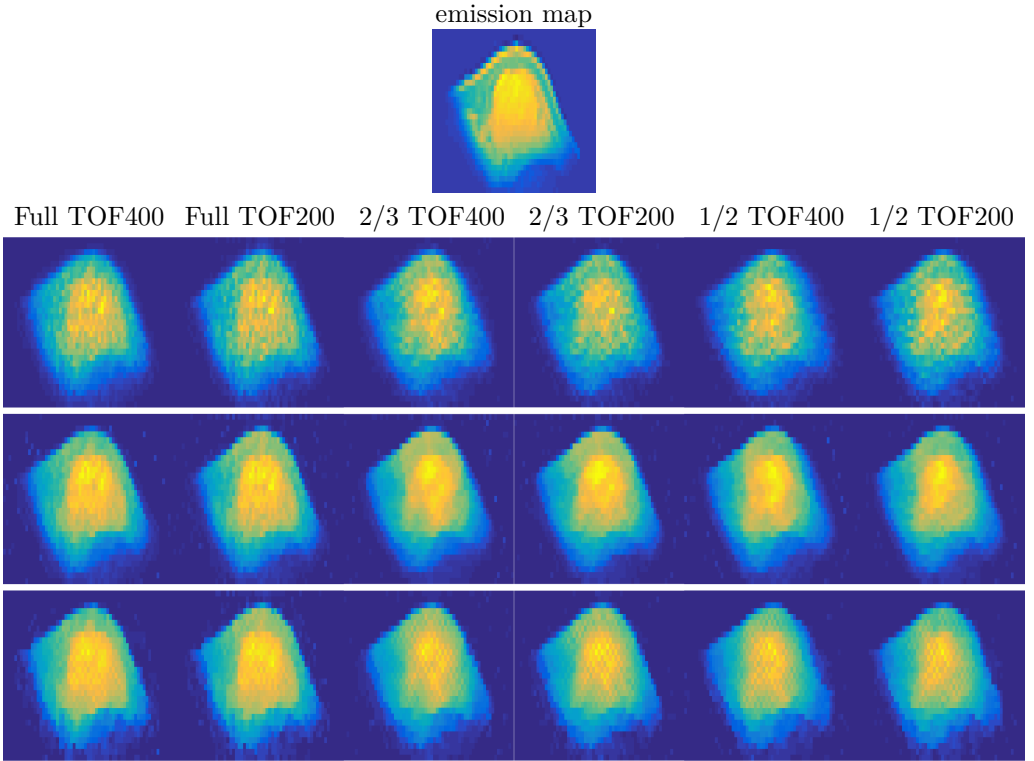


Figure 7.7: Reconstructed images for the realistic phantom. The top row shows the emission image. The 3 rows below the emission image show the reconstructed images with MLEM, MAPEM-MRP and MAPEM-TV respectively. Images here are the central slices along the z (axial) direction.

The accuracy of the reconstructed edges were evaluated using the sigmoid fit parameters h_0 and b . The sigmoid fit parameters for the reconstructions from the realistic phantom data are presented in Table 2 in P IV. The functions were fitted to the normalized line profiles over the central slice and its two closest neighbors along the z direction. Although h_0 values of MAPEM-TV are closer to the emission image than other reconstructions, the slope of the sigmoid fit is steeper for the MAPEM-MRP reconstructions. All fit parameters show a closer fit to the emission image with better TOF information.

The CoV values for the realistic phantom are shown in Table 2 of P IV, which were calculated over the volume enclosed by the 80% iso-contour line (marked red in Figure 6 in P IV). It is clear that all full ring configurations have similar CoVs with the MAP methods. For the partial ring configurations, the variability across slices increase significantly. The lowest CoV is achieved by MAPEM-MRP for nearly all configurations. The CoV values of MLEM is close to those of MAPEM-TV largely because the early stopping of MLEM prevents the amplification of noise, and that the checkerboard artifacts in MAPEM-TV increase the CoV in the selected VOI.

The iso-contours for the reconstructions are depicted in Figure 6 of P IV. MAPEM-MRP reconstructions have more similar iso-contour lines to the emission image compared to MLEM and MAPEM-TV. With MAPEM-MRP, the high activity area, iso-contours marked with red in Figure 6 of P IV, are very close to that of the emission image. On the other hand, the partial ring reconstructions of MLEM and MAP-TV do not correctly

recover the iso-contour lines for the same area.

7.5 Discussion

The limited angle artifacts in in-beam PET data were effectively reduced with the implementation of MRP in MAPEM reconstruction in P IV. Based on the results presented here and in PIV, MRP was found to be less sensitive to hyperparameter selection compared to TV prior, which is also supported by previous research on MRP hyperparameter values [49, 50]. Although 0.3 was selected as optimal value for β for MRP in this work, higher values would also be feasible, with minimal blurring at the edges. On the other hand, the selection of β for TV proved to be critical for the reconstruction quality, which produces artifact-free images for a small range of values. This was also pointed out by Kinouchi *et al.*, where they have used MAP-TV for reconstruction of pencil-beam measurements [101]. Panin *et al.*, who have proposed the TV method for regulating the EM algorithm, also noted the possibility of staircasing effect in the presence of noise [51]. These studies could raise the possibility that such checkerboard artifacts are observed due to the selection of MAP or EM algorithms, if they weren't also observed in [6], where the checkerboard effects were particularly visible for low-count reconstruction results despite using TV together with alternating direction method. It is possible then, that the sparsity assumption does not hold in the presence of high noise in the data, leading to checkerboard effect. This hypothesis was also tested in the thesis work of [108], which showed that the Gaussian filtering together with MAP-TV improves the results of MAP-TV, indicating that the high noise can indeed be the source of checkerboard effect in TV for some penalty weights, and that it can be alleviated with a smoothing filter. Another way to obtain better results with TV, according to the work of Yu *et al.*, is by implementing Poisson TV, which utilizes alternating direction method to solve the TV objective function [6]. They found that LS-TV resulted in higher contrast than Poisson TV, but Poisson-TV was more accurate with lower bias and variance compared to LS-TV. As the accuracy of the reconstruction is more important in proton therapy than the contrast, Poisson-TV could be a possible alternative for incorporating TV prior into in-beam PET reconstruction. Incorporation of wavelet domain filtering into the penalty term alongside TV prior can also help alleviate the artifacts caused by the TV term [109].

As general observations, the selection of the reconstruction method had a greater impact on the reconstructed image fidelity than the CRT of the system. For instance, the elongation was clearly visible with MLEM unless very good TOF information (< 200 ps) was available. In contrast, very little elongation was observed with MAP methods. Both MAP methods were stable throughout large number of iterations. When two MAP methods are compared, the contrast recovery of MRP results was better than the ones with TV prior. The relationship between CoV and reconstruction methods were similar to the observations in [62], in which MLEM results from full ring scanners had higher CoV than partial ring reconstructions with MAP-TV. Despite the difference in CoV values, the NMI values in Figures 7.2 and 7.5 were similar to those of MLEM for optimal β . This shows that although NMI is a good measure for overall image similarity, it does not necessarily give us information about the noise reduction performance of different reconstruction methods. The changes in NMI in terms of image quality was also found to be smaller than the CoVs in [62]. The accuracy of the edges were similar for both MAP methods, but the steeper slopes of MAPEM-MRP reconstructions indicate sharper edges around the irradiated volume. The parameters of the sigmoid fits presented in P IV were in line with the observations on the distal falloff in [62], in which smaller errors and lower

variations were noted for images reconstructed with MAPEM compared to MLEM.

The artifacts in MRP, which occurred outside the irradiated area, were most likely caused by the tails of LORs. The distortion of the slices at the edges of the irradiated volume decreases the NMI of MAPEM-MRP, but it does not affect majority of the slices. Despite the fact that [110] observed similar artifacts with OSEM, not MRP, the authors mentioned that such artifacts outside the images object do not effect the dose verification via PET imaging because the approximate beam location is already known *a priori*. The same argument is valid for the study of dose verification with MRP.

8 Conclusion

The artifacts from missing measurements prevent the accurate reconstruction of structures in tomographic imaging that is crucial for assessment and diagnosis of the imaged subject. The methods developed within this work aimed to reduce the artifacts caused by incomplete data in medical tomographic images with the inclusion of prior knowledge into the reconstruction. They were implemented for incomplete projection data created by (1) the gaps after extraction of high density materials from the projection data in dental CT and (2) limited angular coverage of PET scanners.

The MAR methods proposed for dental CT were tested with a set of phantoms constructed to simulate relevant biological structures for better evaluation of the algorithm performance for each reconstruction problem. Effects of size and proximity of the high density materials were studied, as well as the noise levels and penalty weights. After qualitative and quantitative analysis, it was found that the methods implemented here could provide useful for preventing secondary artifacts after removal of the metallic objects, after being tested on experimental data. The shape, size and proximity of high density materials were found to be important when assessing the performance of the proposed methods, as for small, circular objects gap filling and analytic reconstruction methods may be sufficient. For larger or irregular shaped objects, however, iterative reconstructions would be preferable.

This thesis work on partial ring PET scanners addressed the low sensitivity problem caused by the missing detectors. A dual-panel axial PET demonstrator was designed and constructed, with its properties optimized for breast cancer screening. The preliminary experiments and Monte Carlo simulations were conducted to evaluate the performance of the scanner. With its accurate 3D localization and close proximity to the breast, such a scanner could provide a comparable sensitivity with other available PEM scanners with full-coverage, as well as offering a high resolution decoupled from the sensitivity. A software method, MAP reconstruction with MRP implemented for list-mode data, was also proposed to compensate for the missing angles of in-beam PET data. Various TOF information and angular coverages were studied on geometrical and realistic phantoms, using realistic dose levels and CRT values. The reconstruction results compared the proposed reconstruction method with previously suggested ones in the literature. MAP with MRP was shown to improve the reconstruction efficiently and in a robust way, despite the low-count rates and partial angular coverage of PET data typically acquired during proton therapy.

Although the iterative reconstruction methods implemented in this thesis produced high quality reconstructions, it is important to note that for high-dose/count imaging, analytic reconstruction methods with various gap filling techniques produce fast and reliable images. The iterative methods are slower due to multiple iterations required to obtain

an image. More specifically, MAP methods might introduce bias to non-negativity constraints and different convergence rates in low and high dose/count regions in the image. It is reasonable to assume that with the continuous development of computing power and parallel computing approaches, the iterative methods may become standard for difficult cases of CT imaging as well as for the new types of PET scanners.

The results presented in this thesis were aimed at providing practical solutions to the problems posed by limited-angle data in dental CT and PET. MAP with MRP successfully reduced the noise in a robust way in terms of penalty weight, compared to conventional methods, as well as improving the image fidelity. The effectiveness of the proposed methods in the reconstruction of the low dose/count measurements is also another reason for their implementation in clinical practice. Additionally, the successful application of a data-driven prior such as MRP could widen the possible application areas of such priors in the future.

Bibliography

- [1] E. M. Hussein, *Computed Radiation Imaging*. Elsevier, 2011.
- [2] R. M. Leahy and J. Qi, “Statistical approaches in quantitative positron emission tomography,” *Statistics and Computing*, vol. 10, pp. 147–165, 2000.
- [3] K. Parodi, “Vision 20/20: Positron emission tomography in radiation therapy planning, delivery, and monitoring,” *Medical Physics*, vol. 42, no. 12, pp. 7153–7168, dec 2015.
- [4] D. W. Townsend, “Positron Emission Tomography/Computed Tomography,” pp. 152–166, 2008.
- [5] Y. Gao, Z. Bian, J. Huang, Y. Zhang, S. Niu, Q. Feng, W. Chen, Z. Liang, and J. Ma, “Low-dose X-ray computed tomography image reconstruction with a combined low-mAs and sparse-view protocol,” *Optics express*, vol. 22, no. 12, pp. 15 190–210, jun 2014.
- [6] X. Yu, C. Wang, H. Hu, and H. Liu, “Low dose PET image reconstruction with total variation using alternating direction method,” *PLoS ONE*, vol. 11, no. 12, pp. 1–19, 2016.
- [7] J. Radon, “On the determination of functions from their integral values along certain manifolds,” *IEEE Transactions on Medical Imaging*, vol. 5, no. 4, pp. 170–176, dec 1986.
- [8] R. Lewitt and S. Matej, “Overview of methods for image reconstruction from projections in emission computed tomography,” *Proceedings of the IEEE*, vol. 91, no. 10, pp. 1588–1611, oct 2003.
- [9] H. H. Barrett, T. White, and L. C. Parra, “List-mode likelihood,” *Journal of the Optical Society of America A*, vol. 14, no. 11, pp. 2914–2923, 1997.
- [10] M. N. Ullah, E. Pratiwi, J. Cheon, H. Choi, and J. Y. Yeom, “Instrumentation for Time-of-Flight Positron Emission Tomography,” vol. 50, no. 2, pp. 112–122, jun 2016.
- [11] M. M. Khalil, “Positron emission tomography (PET): Basic principles, year = 2011,” *Basic Sciences of Nuclear Medicine*, pp. 179–284.
- [12] M. Schwaiger, S. Ziegler, and S. G. Nekolla, “PET/CT: Challenge for Nuclear Cardiology,” *J Nucl Med*, vol. 46, no. 10, pp. 1664–1678, oct 2005.

- [13] K. D. Toennies, "Digital image acquisition," in *Guide to Medical Image Analysis*, K.D. Toennies, Ed. London: Springer-Verlag, 2012, ch. 2, pp. 21–82.
- [14] W. C. Scarfe, M. D. Levin, D. Gane, and A. G. Farman, "Use of cone beam computed tomography in endodontics," *International Journal of Dentistry*, vol. 2009, pp. 1–20, 2009.
- [15] J. A. Roberts, N. A. Drage, J. Davies, and D. W. Thomas, "Effective dose from cone beam ct examinations in dentistry," *British Journal of Radiology*, vol. 82, no. 973, pp. 35–40, jan 2009.
- [16] GE Healthcare, "Smart Metal Artifact Reduction (MAR)," Tech. Rep., 2013. [Online]. Available: http://www3.gehealthcare.com/en/Products/Categories/Computed_Tomography/Radiation_Therapy_Planning/Metal_Artifact_Reduction
- [17] L. Gjesteby, B. De Man, Y. Jin, H. Paganetti, J. Verburg, D. Giantsoudi, and G. Wang, "Metal artifact reduction in CT: Where are we after four decades?, volume = 4, year = 2016," *IEEE Access*, pp. 5826–5849.
- [18] B. De Man, J. Nuyts, P. Dupont, G. Marchai, and P. Suetens, "Metal streak artifacts in x-ray computed tomography: A simulation study, volume = 46, year = 1999," *IEEE Transactions on Nuclear Science*, no. 3 PART 2, pp. 691–696, jun.
- [19] J. F. Barrett and N. Keat, "Artifacts in CT: Recognition and Avoidance," *RadioGraphics*, vol. 24, no. 6, pp. 1679–1691, 2004.
- [20] J. Y. Huang, J. R. Kerns, J. L. Nute, X. Liu, P. A. Balter, F. C. Stingo, D. S. Followill, D. Mirkovic, R. M. Howell, and S. F. Kry, "An evaluation of three commercially available metal artifact reduction methods for ct imaging," *Physics in Medicine and Biology*, vol. 60, no. 3, pp. 1047–1067, 2015.
- [21] Phillips, "Metal Artifact Reduction for Orthopedic Implants (O-MAR)," *Philips Healthcare*, pp. 1–12, 2011. [Online]. Available: [http://clinical.netforum.healthcare.philips.com/us/{_}en/Explore/White-Papers/CT/Metal-Artifact-Reduction-for-Orthopedic-Implants-\(O-MAR\)](http://clinical.netforum.healthcare.philips.com/us/{_}en/Explore/White-Papers/CT/Metal-Artifact-Reduction-for-Orthopedic-Implants-(O-MAR))
- [22] N. Subhas, A. N. Primak, N. A. Obuchowski, A. Gupta, J. M. Polster, A. Krauss, and J. P. Iannotti, "Iterative metal artifact reduction: Evaluation and optimization of technique," *Skeletal Radiology*, vol. 43, no. 12, pp. 1729–1735, 2014.
- [23] K. Sofue, T. Yoshikawa, N. Negi, Y. Ohno, N. Sugihara, H. Koyama, M. Nishio, and K. Sugimura, "Abdominal CT with Single-Energy Metal Artifact Reduction (SEMAR): Initial Experiences," *European Society of Radiology*, Tech. Rep., 2014.
- [24] B. Li, Q. Xie, Y. Guo, C. Zeng, S. Wang, R. Zheng, L. Wan, and P. Xiao, "A Panel PET With Window: Design, Performance Evaluation, and Prototype Development," *IEEE Transactions on Radiation and Plasma Medical Sciences*, vol. 1, no. 4, pp. 310–321, jul 2017.
- [25] E. Lee, M. E. Werner, J. S. Karp, and S. Surti, "Design optimization of a dedicated breast PET scanner using TOF imaging in a partial ring geometry," in *2011 IEEE Nuclear Science Symposium Conference Record*. IEEE, oct 2011, pp. 4276–4280.

- [26] D. Narayanan and W. A. Berg, "Dedicated Breast Gamma Camera Imaging and Breast PET: Current Status and Future Directions," *PET Clinics*, vol. 13, no. 3, pp. 363–381, jul 2018.
- [27] J. Hadamard, *Le probleme de Cauchy et les equations aux derivees oartielles lineaires hyperboliques*. Paris: Hermann et cie, 1932.
- [28] A. Doicu, T. Trautmann, and F. Schreier, "Ill-posedness of linear problems," in *Numerical Regularization for Atmospheric Inverse Problems*. Berlin, Heidelberg: Springer Berlin Heidelberg, 2010, pp. 23–38.
- [29] G. L. Zeng, "Basic principles of tomography," in *Medical Image Reconstruction*, Gengsheng Lawrence Zeng, Ed., Heidelberg, 2010, ch. 1, pp. 1–19.
- [30] D. Fleischmann and F. E. Boas, "Computed tomography-old ideas and new technology," vol. 21, no. 3, pp. 510–517, 2011.
- [31] M. J. Willemink, P. A. De Jong, T. Leiner, L. M. De Heer, R. A. Nievelstein, R. P. Budde, and A. M. Schilham, "Iterative reconstruction techniques for computed tomography part 1: Technical principles," *European Radiology*, vol. 23, no. 6, pp. 1623–1631, jun 2013.
- [32] R. Gordon, R. Bender, and T. Gabor, "Algebraic Reconstruction Techniques (ART) for Three-dimensional Electron Microscopy and X-ray Photography," *Journal of Theoretical Biology*, vol. 29, pp. 471–481, 1970.
- [33] R. Cierniak, *X-ray computed tomography in biomedical engineering*. London: Springer London, 2011.
- [34] J. Qi and R. M. Leahy, "Iterative reconstruction techniques in emission computed tomography," *Physics in Medicine and Biology*, vol. 51, no. 15, pp. R541–R578, aug 2006.
- [35] P. J. Green, "Bayesian reconstructions from emission tomography data using a modified em algorithm," *IEEE Transactions on Medical Imaging*, vol. 9, no. 1, pp. 84–93, mar 1990.
- [36] K. Lange and R. Carson, "EM reconstruction algorithms for emission and transmission tomography," *Journal of computer assisted tomography*, vol. 8, no. 2, pp. 306–316, 1984.
- [37] L. A. Shepp and Y. Vardi, "Maximum Likelihood Reconstruction for Emission Tomography," *IEEE Transactions on Medical Imaging*, vol. 1, no. 2, pp. 113–122, oct 1982.
- [38] L. Kaufman, "Maximum likelihood, least squares, and penalized least squares for pet," *IEEE Transactions on Medical Imaging*, vol. 12, no. 2, pp. 200–214, jun 1993.
- [39] Y. Vardi, L. A. Shepp, and L. Kaufman, "A Statistical Model for Positron Emission Tomography," *Journal of the American Statistical Association*, vol. 80, no. 389, p. 8, mar 1985.
- [40] S. Geman and D. McClure, "Bayesian Image Analysis: An application to Single Photon Emission Tomography," in *Proceedings of the American Statistical Association*, 1985, pp. 12–18.

- [41] L. Yang, J. Zhou, A. Ferrero, R. D. Badawi, and J. Qi, "Regularization design in penalized maximum-likelihood image reconstruction for lesion detection in 3D PET," *Physics in Medicine and Biology*, vol. 59, no. 2, pp. 403–419, jan 2014.
- [42] E. Rapisarda, L. Presotto, E. De Bernardi, M. C. Gilardi, and V. Bettinardi, "Optimized Bayes variational regularization prior for 3D PET images," *Computerized Medical Imaging and Graphics*, vol. 38, no. 6, pp. 445–457, sep 2014.
- [43] Z. Wang and A. C. Bovik, "Mean squared error: Love it or leave it? a new look at signal fidelity measures," *IEEE Signal Processing Magazine*, vol. 26, no. 1, pp. 98–117, 2009.
- [44] H. Hudson and R. Larkin, "Accelerated image reconstruction using ordered subsets of projection data," *IEEE Transactions on Medical Imaging*, vol. 13, no. 4, pp. 601–609, 1994.
- [45] N. V. Denisova, "Regularized versus non-regularized statistical reconstruction techniques," *Nuclear Instruments and Methods in Physics Research, Section A: Accelerators, Spectrometers, Detectors and Associated Equipment*, vol. 648, no. SUPPL. 1, pp. S65–S67, aug 2011.
- [46] K. Sauer and C. Bouman, "A local update strategy for iterative reconstruction from projections," *IEEE Transactions on Signal Processing*, vol. 41, no. 2, pp. 534–548, 1993.
- [47] S. Kawata and O. Nalcioglu, "Constrained iterative reconstruction by the conjugate gradient method," *IEEE transactions on medical imaging*, vol. 4, no. 2, pp. 65–71, jun 1985.
- [48] J. A. Fessler, "Penalized weighted least-squares image reconstruction for positron emission tomography," *Transactions on Medical Imaging*, vol. 13, no. 2, pp. 290–300, 1994.
- [49] S. Alenius and U. Ruotsalainen, "Bayesian image reconstruction for emission tomography based on median root prior," *European Journal of Nuclear Medicine*, vol. 24, no. 3, pp. 258–265, mar 1997.
- [50] S. Alenius, U. Ruotsalainen, and J. Astola, "Using local median as the location of the prior distribution in iterative emission tomography image reconstruction," *IEEE Transactions on Nuclear Science*, vol. 45, no. 6 Part 2, pp. 3097–3104, 1998.
- [51] V. Y. Panin, G. L. Zeng, and G. T. Gullberg, "Total variation regulated EM algorithm," *IEEE Transactions on Nuclear Science*, vol. 46, no. 6, pp. 2202–2210, 1999.
- [52] E. Y. Sidky and X. Pan, "Image reconstruction in circular cone-beam computed tomography by constrained, total-variation minimization," *Physics in Medicine and Biology*, vol. 53, no. 17, pp. 4777–4807, 2008.
- [53] L. Parra and H. H. Barrett, "List-mode likelihood: EM algorithm and image quality estimation demonstrated on 2-D PET," *IEEE transactions on medical imaging*, vol. 17, no. 2, pp. 228–235, 1998.

- [54] A. J. Reader, K. Erlandsson, M. A. Flower, and R. J. Ott, "Fast accurate iterative reconstruction for low-statistics positron volume imaging," *Physics in medicine and biology*, vol. 43, no. 4, pp. 835–846, 1998.
- [55] A. J. Reader, "List-mode EM algorithms for limited precision high-resolution PET image reconstruction," *International Journal of Imaging Systems and Technology*, vol. 14, no. 3, pp. 139–145, 2004.
- [56] C. Schretter, "Event-by-event image reconstruction from list-mode PET data," *IEEE Transactions on Image Processing*, vol. 18, no. 1, pp. 117–124, jan 2009.
- [57] C. Byrne, "Likelihood maximization for list-mode emission tomographic image reconstruction," *IEEE Transactions on Medical Imaging*, vol. 20, no. 10, pp. 1084–1092, 2001.
- [58] S. Surti, W. Zou, M. E. Daube-Witherspoon, J. McDonough, and J. S. Karp, "Design Study of an In-Situ PET Scanner for Use in Proton Beam Therapy," *Physics in Medicine and Biology*, vol. 7, no. 56, pp. 2667–2685, 2011.
- [59] L. Popescu, S. Matej, and R. Lewitt, "Iterative image reconstruction using geometrically ordered subsets with list-mode data," *IEEE Symposium Conference Record Nuclear Science 2004.*, vol. 6, no. C, pp. 3536–3540, 2004.
- [60] C. Studholme, D. Hill, and D. Hawkes, "An overlap invariant entropy measure of 3D medical image alignment," *Pattern Recognition*, vol. 32, no. 1, pp. 71–86, 1999.
- [61] J. Pluim, J. Maintz, and M. Viergever, "Mutual-information-based registration of medical images: a survey," *IEEE Transactions on Medical Imaging*, vol. 22, no. 8, pp. 986–1004, aug 2003.
- [62] J. Cabello, I. Torres-Espallardo, J. E. Gillam, and M. Rafecas, "PET reconstruction from truncated projections using total-variation regularization for hadron therapy monitoring," *IEEE Transactions on Nuclear Science*, vol. 60, no. 5, pp. 3364–3372, oct 2013.
- [63] S. Karimi, P. Cosman, C. Wald, and H. Martz, "Segmentation of artifacts and anatomy in CT metal artifact reduction," *Medical Physics*, vol. 39, no. 10, pp. 5857–5868, 2012.
- [64] O. Watzke and W. A. Kalender, "A pragmatic approach to metal artifact reduction in CT: Merging of metal artifact reduced images," *European Radiology*, vol. 14, no. 5, pp. 849–856, may 2004.
- [65] C. Saint Olive, M. R. Kaus, V. Pekar, K. Eck, and L. Spies, "Segmentation-aided adaptive filtering for metal artifact reduction in radio-therapeutic CT images," J. M. Fitzpatrick and M. Sonka, Eds., vol. 5370. International Society for Optics and Photonics, may 2004, p. 1991.
- [66] A. Mehranian, M. R. Ay, A. Rahmim, and S. Member, "X-ray CT Metal Artifact Reduction Using Wavelet Domain L0 Sparse Regularization," *IEEE Transactions on Medical Imaging*, vol. 32, no. 9, pp. 1707–1722, 2013.
- [67] S. Zhao, D. D. Robertson, G. Wang, B. Whiting, and K. T. Bae, "X-ray CT metal artifact reduction using wavelets: an application for imaging total hip prostheses," *IEEE Transactions on Medical Imaging*, vol. 19, no. 12, pp. 1238–1247, 2000.

- [68] Y. Zhang, L. Zhang, X. R. Zhu, A. K. Lee, M. Chambers, and L. Dong, "Reducing metal artifacts in cone-beam ct images by preprocessing projection data," *International Journal of Radiation Oncology Biology Physics*, vol. 67, no. 3, pp. 924–932, 2007.
- [69] S. Tohnaek, A. J. H. Mehnert, M. Mahoney, and S. Crozier, "Dental CT metal artefact reduction based on sequential substitution," *Dentomaxillofacial Radiology*, vol. 40, no. 3, pp. 184–190, 2011.
- [70] A. Mehranian, M. R. Ay, A. Rahmim, and H. Zaidi, "Sparsity constrained sinogram inpainting for metal artifact reduction in X-ray computed tomography," in *2011 IEEE Nuclear Science Symposium Conference Record*. IEEE, oct 2011, pp. 3694–3699.
- [71] J. Shen and T. F. Chan, "Mathematical models for local nontexture inpaintings," *SIAM Journal on Applied Mathematics*, vol. 62, no. 3, pp. 1019–1043, jan 2002.
- [72] X. Duan, L. Zhang, Y. Xiao, J. Cheng, Z. Chen, and Y. Xing, "Metal artifact reduction in CT images sinogram TV inpainting," in *IEEE Nuclear Science Symposium Conference Record*. IEEE, oct 2008, pp. 4175–4177.
- [73] M. A. A. Hegazy, M. H. Cho, and S. Y. Lee, "A metal artifact reduction method for a dental ct based on adaptive local thresholding and prior image generation," *BioMedical Engineering OnLine*, vol. 15, no. 1, p. 119, 2016.
- [74] Z. Tang, G. Hu, and H. Zhang, "Efficient metal artifact reduction method based on improved total variation regularization," *Journal of Medical and Biological Engineering*, vol. 34, no. 3, pp. 261–268, 2013.
- [75] B. Meng, J. Wang, and L. Xing, "Sinogram preprocessing and binary reconstruction for determination of the shape and location of metal objects in computed tomography (CT)," *Medical Physics*, vol. 37, no. 11, pp. 5867–5875, nov 2010.
- [76] G. Wang, D. L. Snyder, J. A. O'Sullivan, and M. W. Vannier, "Iterative deblurring for CT metal artifact reduction," *IEEE Transactions on Medical Imaging*, vol. 15, no. 5, pp. 657–664, 1996.
- [77] X. Zhang, J. Wang, and L. Xing, "Metal artifact reduction in X-ray computed tomography (CT) by constrained optimization, volume = 38, year = 2011," *Medical physics*, no. 2, pp. 701–11, feb.
- [78] C. Peng, B. Qiu, M. Li, Y. Yang, C. Zhang, L. Gong, and J. Zheng, "GPU-accelerated dynamic wavelet thresholding algorithm for X-Ray CT metal artifact reduction," *IEEE Transactions on Radiation and Plasma Medical Sciences*, vol. 2, no. 1, pp. 17–26, jan 2018.
- [79] U. Tuna, A. Sohlberg, and U. Ruotsalainen, "Can We Reduce SPECT Acquisition Time Using MAP-EM Reconstruction?" *Journal of Pattern Recognition and Intelligent Systems*, vol. 1, no. 3, pp. 54–63, 2013.
- [80] E. Acar, S. Peltonen, and U. Ruotsalainen, "Adaptive multiresolution method for MAP reconstruction in electron tomography," *Ultramicroscopy*, vol. 170, pp. 24–34, 2016.

- [81] S. Pursiainen and M. Kaasalainen, “Orbiter-to-orbiter tomography: A potential approach for small solar system bodies,” Tech. Rep. 6, 2016.
- [82] N. Otsu, “A threshold selection method from gray-level histograms,” *IEEE Transactions on Systems, Man, and Cybernetics*, vol. 9, no. 1, pp. 62–66, jan 1979.
- [83] Y. Liu, J. Ma, Y. Fan, and Z. Liang, “Adaptive-weighted total variation minimization for sparse data toward low-dose X-ray computed tomography image reconstruction,” *Physics in Medicine and Biology*, vol. 57, no. 23, pp. 7923–7956, dec 2012.
- [84] W. H. O. International Agency for Research on Cancer, “Latest world cancer statistics Global cancer burden rises to 14 . 1 million new cases in 2012 : Marked increase in breast cancers must be addressed.” Tech. Rep. December, 2013. [Online]. Available: <http://www.iarc.fr/en/media-centre/pr/2013/pdfs/pr223{ }E.pdf>
- [85] C. B. Hruska and M. K. O’Connor, “Nuclear imaging of the breast: Translating achievements in instrumentation into clinical use,” *Medical Physics*, vol. 40, no. 5, p. 050901, may 2013.
- [86] W. W. Moses, “Positron emission mammography imaging,” in *Nuclear Instruments and Methods in Physics Research, Section A: Accelerators, Spectrometers, Detectors and Associated Equipment*, vol. 525, no. 1-2. North-Holland, jun 2004, pp. 249–252.
- [87] M. V. Martins, “Positron Emission Mammography,” in *Mammography Techniques and Review*, F. C. Fernandes, L. M. Brasil, and R. d. V. Guadagnin, Eds. InTech, jul 2015, pp. 39–62.
- [88] S. B. Glass and Z. A. Shah, “Clinical utility of positron emission mammography,” *Proceedings (Baylor University. Medical Center)*, vol. 26, no. 3, pp. 314–9, jul 2013.
- [89] Y. Wu, S. L. Bowen, K. Yang, N. Packard, L. Fu, G. Burkett, J. Qi, J. M. Boone, S. R. Cherry, and R. D. Badawi, “ET characteristics of a dedicated breast PET/CT scanner prototype,” *Physics in Medicine and Biology*, vol. 54, no. 13, pp. 4273–4287, jul 2009.
- [90] A. Collarino, V. Fuoco, L. Arias-Bouda, A. Sánchez, L.-F. de Geus-Oei, R. Masetti, and R. Olmos, “Novel frontiers of dedicated molecular imaging in breast cancer diagnosis,” *Translational Cancer Research*, vol. 7, no. 3, pp. 295–306, 2018.
- [91] M. Furuta, K. Kitamura, J. Ohi, H. Tonami, Y. Yamada, T. Furumiya, M. Satoh, T. Tsuda, M. Nakazawa, N. Hashizume, Y. Yamakawa, A. Kawashima, and Y. Kumazawa, “Basic evaluation of a C-shaped breast PET scanner,” in *IEEE Nuclear Science Symposium Conference Record*. IEEE, oct 2009, pp. 2548–2552.
- [92] D. Uzun, G. D. Lorenzo, M. Kolstein, and M. Chmeissani, “Simulation and evaluation of a high resolution VIP PEM system with a dedicated LM-OSEM algorithm,” *Journal of Instrumentation*, vol. 9, no. 5, 2014.
- [93] M. V. Green, H. G. Ostrow, J. Seidel, and M. G. Pomper, “Experimental evaluation of depth-of-interaction correction in a small-animal positron emission tomography scanner,” *Molecular Imaging*, vol. 9, no. 6, pp. 311–318, 2010.
- [94] E. P. Delfino, S. Majewski, R. R. Raylman, and A. Stolin, “Towards 1mm PET resolution using DOI modules based on dual-sided SiPM readout, year = 2010,” in *IEEE Nuclear Science Symposium Conference Record*. IEEE, oct, pp. 3442–3449.

- [95] P. Beltrame, E. Bolle, A. Braem, C. Casella, E. Chesi, N. Clinthorne, R. De Leo, G. Dissertori, L. Djambazov, V. Fanti, M. Heller, C. Joram, H. Kagan, W. Lustermann, F. Meddi, E. Nappi, F. Nessi-Tedaldi, J. F. Oliver, F. Pauss, M. Rafecas, D. Renker, A. Rudge, D. Schinzel, T. Schneider, J. Séguinot, P. Solevi, S. Stapnes, and P. Weilhammer, “The AX-PET demonstrator - Design, construction and characterization,” *Nuclear Instruments and Methods in Physics Research, Section A: Accelerators, Spectrometers, Detectors and Associated Equipment*, vol. 654, no. 1, pp. 546–559, oct 2011.
- [96] S. Ylipää, “Monte Carlo simulations of an axial positron emission tomography demonstrator,” MSc. thesis, Tampere University of Technology, 2015.
- [97] P. Solevi, J. F. Oliver, J. E. Gillam, E. Bolle, C. Casella, E. Chesi, R. De Leo, G. Dissertori, V. Fanti, M. Heller, M. Lai, W. Lustermann, E. Nappi, F. Pauss, A. Rudge, U. Ruotsalainen, D. Schinzel, T. Schneider, J. Séguinot, S. Stapnes, P. Weilhammer, U. Tuna, C. Joram, and M. Rafecas, “A Monte-Carlo based model of the AX-PET demonstrator and its experimental validation,” *Physics in Medicine and Biology*, vol. 58, no. 16, pp. 5495–5510, aug 2013.
- [98] E. Bolle, C. Casella, E. Chesi, R. De Leo, G. Dissertori, V. Fanti, J. E. Gillam, M. Heller, C. Joram, W. Lustermann, E. Nappi, J. F. Oliver, F. Pauss, M. Rafecas, A. Rudge, U. Ruotsalainen, D. Schinzel, T. Schneider, J. Séguinot, P. Solevi, S. Stapnes, U. Tuna, and P. Weilhammer, “AX-PET: A novel PET concept with G-APD readout,” *Nuclear Instruments and Methods in Physics Research, Section A: Accelerators, Spectrometers, Detectors and Associated Equipment*, vol. 695, pp. 129–134, 2012.
- [99] C. Casella, M. Heller, C. Joram, and T. Schneider, “A high resolution TOF-PET concept with axial geometry and digital SiPM readout,” *Nuclear Instruments and Methods in Physics Research A*, vol. 736, no. 2014, pp. 161–168, 2015.
- [100] P. Crespo, G. Shakirin, and W. Enghardt, “On the detector arrangement for in-beam PET for hadron therapy monitoring,” *Physics in Medicine and Biology*, vol. 51, no. 9, pp. 2143–2163, may 2006.
- [101] S. Kinouchi, T. Yamaya, H. Tashima, E. Yoshida, H. Ito, and M. Suga, “Total variation minimization for in-beam PET image reconstruction,” in *IEEE Nuclear Science Symposium Conference Record*. IEEE, oct 2012, pp. 3412–3414.
- [102] C. Hui, D. Robertson, and S. Beddar, “3D reconstruction of scintillation light emission from proton pencil beams using limited viewing angles - A simulation study,” *Physics in Medicine and Biology*, vol. 59, no. 16, pp. 4477–4492, aug 2014.
- [103] P. Crespo, G. Shakirin, F. Fiedler, W. Enghardt, and A. Wagner, “Direct time-of-flight for quantitative, real-time in-beam PET: A concept and feasibility study,” *Physics in Medicine and Biology*, vol. 52, no. 23, pp. 6795–6811, dec 2007.
- [104] V. Bettinardi, E. Pagani, M. Gilardi, S. Alenius, K. Thielemans, M. Teras, and F. Fazio, “Implementation and evaluation of a 3D one-step late reconstruction algorithm for 3D positron emission tomography brain studies using median root prior,” *European Journal of Nuclear Medicine*, vol. 29, no. 1, pp. 7–18, 2002.

- [105] S. Jan, D. Benoit, E. Becheva, T. Carlier, F. Cassol, P. Descourt, T. Frisson, L. Grevillot, L. Guigues, L. Maigne, C. Morel, Y. Perrot, N. Rehfeld, D. Sarrut, D. R. Schaart, S. Stute, U. Pietrzyk, D. Visvikis, N. Zahra, and I. Buvat, “GATE V6: A major enhancement of the GATE simulation platform enabling modeling of CT and radiotherapy,” *Physics in Medicine and Biology*, vol. 56, no. 4, pp. 881–901, feb 2011.
- [106] S. Agostinelli, J. Allison, and K. Amako, “Geant4 - A simulation toolkit,” *Nuclear Instruments and Methods in Physics Research A*, vol. 506, pp. 250–303, jul 2003.
- [107] C. Burger, G. Goerres, S. Schoenes, A. Buck, A. Lonn, and G. Von Schulthess, “PET attenuation coefficients from CT images: Experimental evaluation of the transformation of CT into PET 511-keV attenuation coefficients,” *European Journal of Nuclear Medicine*, vol. 29, no. 7, pp. 922–927, 2002.
- [108] K. Lou, “Feasibility of on-line proton beam range verification with positron emission tomography imaging,” PhD Thesis, Rice University, 2015. [Online]. Available: <https://scholarship.rice.edu/handle/1911/88105>
- [109] S. Valiollahzadeh, J. W. Clark, and O. Mawlawi, “Using compressive sensing to recover images from PET scanners with partial detector rings,” *Medical Physics*, vol. 42, no. 1, pp. 121–133, dec 2014.
- [110] C. Kurz, J. Bauer, M. Conti, L. Guérin, L. Eriksson, and K. Parodi, “Investigating the limits of PET/CT imaging at very low true count rates and high random fractions in ion-beam therapy monitoring,” *Medical Physics*, vol. 42, no. 7, pp. 3979–3991, jun 2015.

Publications

PUBLICATION

I

Metal Artifact Reduction Based on Multi-Level Sinogram Segmentation and Sequentially Applied MAP-EM Reconstruction Method

U. Tuna*, D. Us*, U. Ruotsalainen (* equal contribution)

2013 IEEE Nuclear Science Symposium and Medical Imaging Conference Record (NSS/MIC)
pp. 3412—3414, Nov. 2013, Seoul, South Korea

[10.1109/NSSMIC.2013.6829179](https://doi.org/10.1109/NSSMIC.2013.6829179)

Publication reprinted with the permission of the copyright holders.

© 2013 IEEE

Metal Artifact Reduction Based on Multi-Level Sinogram Segmentation and Sequentially Applied MAP-EM Reconstruction Method

Uygur Tuna*, *Student Member, IEEE*, Defne Us*, *Member, IEEE*, and Ulla Ruotsalainen, *Member, IEEE*

Abstract: Metal artifacts and their reduction is a common problem in imaging field because artifacts arising from these high density objects often hinder the underlying anatomical structures. This study investigates the performance of sequentially applied *maximum a posteriori* expectation maximization (MAP-EM) for metal artifact correction. Firstly, positions of metal objects were identified with a novel multi-level segmentation method based on weighted Otsu's threshold level. The sinogram bins representing the metal objects were regarded as missing data which are modeled in the system matrix of the sequentially applied MAP-EM method with the spatial domain median filtering. Regularization level in the MAP-EM was decreased gradually throughout the sequences. Qualities of reconstructed images were investigated both qualitatively and quantitatively on a numerical jaw phantom with different amount of metals. NMSE% and line profile analysis results were in parallel with the visual impression that as penalization is reduced, reconstructed images have higher contrast with sharper boundaries between anatomical structures. This study provides encouraging results for using sequentially iterative algorithms such as sequentially applied MAP-EM in order to have a more accurate reconstruction of intensity values.

I. INTRODUCTION

HIGH density objects in the field-of-view (FOV) result in so-called metal artifacts in the reconstructed images in X-Ray Computerized Tomography (CT), especially in dental applications. Metal artifact reduction (MAR) methods intend to abate the severe effects of these highly attenuating materials in the reconstructed CT images. Attempts to use low dose radiation in dental imaging modalities such as cone-beam CT (CBCT) increases the importance of automated segmentation of metallic regions as low contrast between teeth and metals make metal extraction more difficult. Collinearity of multiple metals on the same image plane is also another motivation for automated segmentation. MAR methods are composed of two main steps: (1) Segmentation of the projection data (sinogram bins), which are affected from the high density objects in the FOV. (2) Reduction of the metal artifacts before or during the image reconstruction with the methods based on interpolation using neighboring sinogram bins, sinogram inpainting, Fourier and

DCT-based methods, projection-backprojection approaches and λ -MLEM method [1-7]. If metals are extracted accurately in step (1), they can be treated as missing projection bins in step (2) for modeling of the system matrix.

II. MATERIALS AND METHODS

As the simulation dataset, we used a numerical jaw phantom¹ (128x128) and its sinograms (128 radial bins, 180 angular views). In Fig. 1, we show the 14 possible locations for metal dental implants in the image and sinogram domains. By picking various combinations for metal dental filling locations, we generated 4 different phantom images with various numbers and sizes of dental metal implants (1, 6, 7 and 14 metal fillings). In addition to the 4 ideal (non-noisy) cases, the generated sinograms were contaminated with Gaussian noise making up 8 sinograms in total.

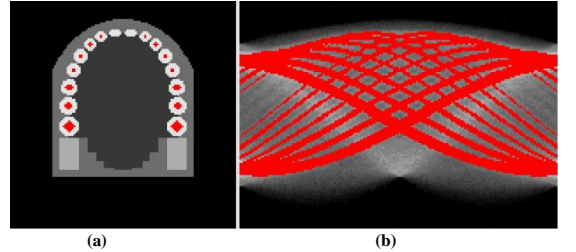


Fig. 1. (a) Locations for the metal fillings are shown with red color in the numerical jaw phantom image. (b) The projection data affected from the metal fillings are shown with red color in the corresponding sinogram which is contaminated with Gaussian noise. Teeth, jaw bone, soft tissue and air gap inside the mouth have the intensity values of 1, 0.75, 0.5 and 0.25 respectively.

Before the application of the sequentially applied MAP-EM method [9], we segmented the sinogram bins affected from the metal implants by a novel multi-level segmentation method using weighted Otsu's threshold (see Fig. 2). Otsu's method finds the threshold level, which minimizes the intra-class variance of the white and the black pixels in a gray scale image [8] on the image histogram. We denoted the Otsu's threshold level with t_{OTSU} . The segmentation method which we proposed in this study firstly performed thresholding at multiple (19 in this study) levels which are obtained from the Otsu's threshold (t_{OTSU}) using the experimentally found weights $a_i = \{a_{-9}, a_{-8} \dots a_{-1}, a_0, a_1 \dots a_8, a_9\}$. In this study we used $a_i = \{0.1, 0.2 \dots 0.9, 1, 1.1 \dots 1.8, 1.9\}$ for threshold level weights. Secondly, the weighted average of the binary images generated using different threshold levels were calculated. The experimentally determined weights $w_i = \{w_{-9}, w_{-8} \dots w_{-1}, w_0, w_1 \dots w_8, w_9\}$ for the weighted averaging were $w_i = \{1, 3, 4.6, 4.8, 5, 5.2, 5.5, 5.7, 5.9, 6, 5.9,$

* Authors have equal contribution to the paper.

This work was supported by the Graduate School in Electronics, Telecommunication and Automation (GETA), Finland.

U. Tuna, D. Us, and U. Ruotsalainen are with the Department of Signal Processing, Tampere University of Technology, P.O. BOX 533, FIN-33101, BioMediTech, Tampere, Finland (e-mail: firstname.surname@tut.fi).

¹ <http://www.imp.uni-erlangen.de/phantoms/jaw/jaw.htm>

5.7, 5.5, 5.2, 5, 4.8, 4.6, 3, 1}. Thirdly, in order to ensure the continuity of the sinogram, sinogram was backprojected using

Algorithm defined in (1) is run 91 times for each β sequence before changing the β to the next value.

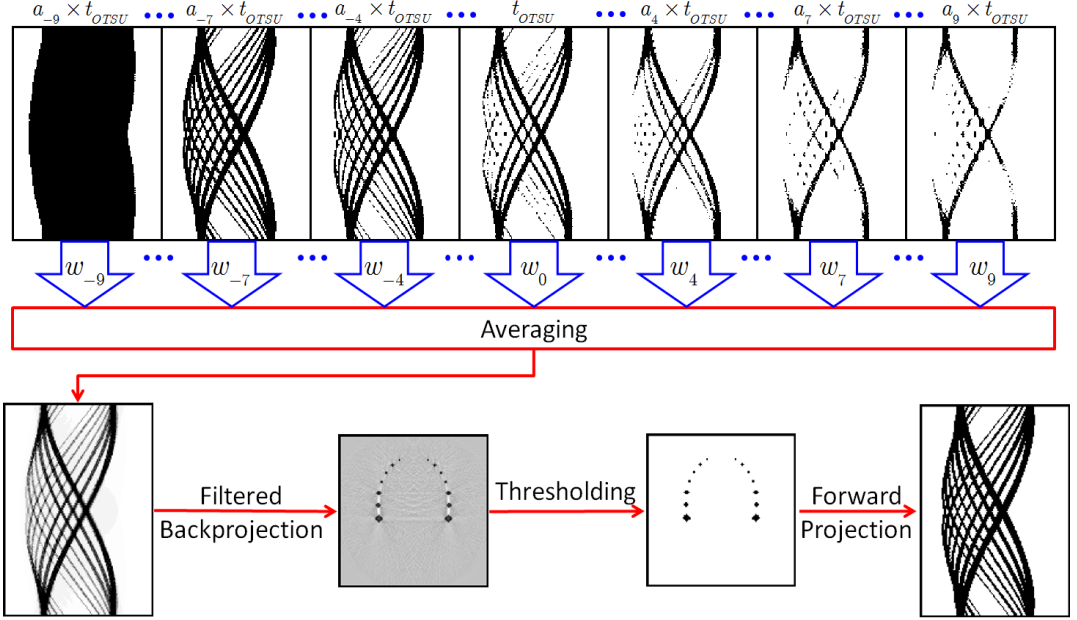


Fig. 2. Block diagram for the sinogram segmentation using the Otsu's threshold at multiple levels. t_{OTSU} represents the Otsu's threshold level. The experimentally found weights a_i 's are used to threshold the sinogram with metal artifacts at multiple levels. The weighted averaged mask sinogram is calculated with w_i 's which are decided based on the performed experiments. The spatial and sinogram domain masks for the metal objects are generated using FBP and backprojection operators.

filtered back projection (FBP) with a Ramp filter. Resulting image was thresholded with global thresholding.

As the final step, the metal mask was forward projected into sinogram domain before being fed to the sequentially applied MAP-EM reconstruction method. We reconstructed the images with the sequentially applied MAP-EM (or regularized MLEM) method with median filtering which was implemented using one-step-late (OSL) algorithm [9]. Sequentially applied MAP-EM with OSL algorithm is formulated as follows:

$$\lambda_j^{k+1} = \frac{\lambda_j^k}{\sum_i a_{ij} + \beta \left(\frac{\lambda_j^k - M_j}{M_j} \right)} \sum_i \left(\frac{y_{i \in \text{known_bins}}}{\sum_j a_{ij} \lambda_j^k} + J_{i \in \text{unknown_bins}} \right) \quad (1)$$

where λ_j^{k+1} and λ_j^k are the pixel values in the reconstructed images in current and next iterations respectively, a_{ij} is the system matrix, β is the control parameter for regularization, y_i represents the projection data, J_i is the vector of ones modeling the unmeasured sinogram bins and M_j is the penalty reference calculated by using different spatial domain regularizers. The sinogram bins which were affected from the metal objects and segmented out in the previous step were regarded as the missing parts of the projection data. Missing parts of the data were modeled in the system matrix. In the correction sinogram, the correction factors of unknown bins were set to 1, which were later estimated throughout the iterations of MLEM.

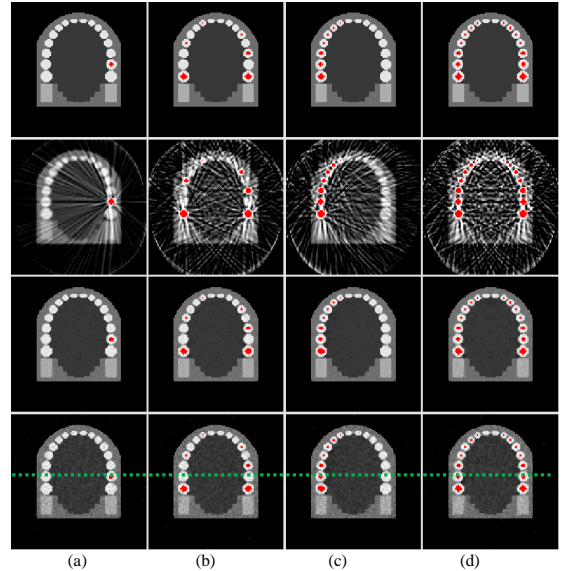


Fig. 3. Simulation results with different amount of metal dental fillings and Gaussian noise contamination. Rows from top to bottom: Ground-truth images, images reconstructed using FBP with Ramp filter, images reconstructed with sequentially applied MAP-EM from non-noisy (ideal) sinograms, reconstructed images obtained with sequentially applied MAP-EM from noisy sinograms. Columns: (a) – (d) show simulations with different amounts of metal fillings. Green line marked on reconstructed images was used for line profile analysis.

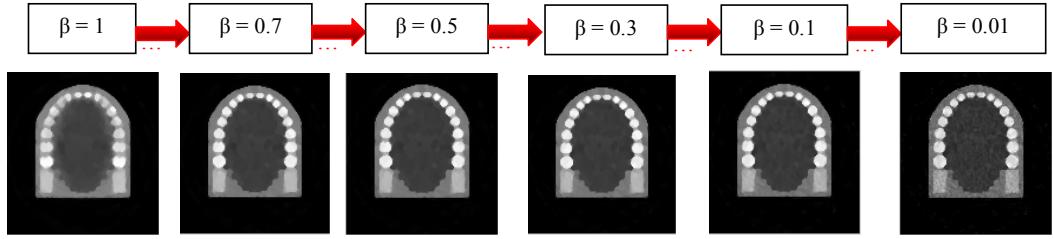


Fig. 4. Effect of gradually reducing β in MAP-EM is shown on the resulting images of numerical jaw phantom for intermediate steps of $\beta=1$, $\beta=0.7$, $\beta=0.5$, $\beta=0.3$, $\beta=0.1$ and $\beta=0.01$ are depicted. Blurring caused by the regularization decreases as β is reduced and teeth boundaries become sharper.

Throughout the MLEM iterations, the strength of spatial regularization was reduced step-by-step by varying β from 1 to 0.1 with steps of 0.1, where $\beta=1$ corresponds to full regularization. In order to avoid the situation without regularization, minimum β value was chosen as 0.01. Fig.4. depicts the decrease in blurring throughout the resulting images of reducing β sequences.

With this novel sequential application of the spatial domain regularization filter, the missing parts of the sinograms were filled consistently while the undesired effects (such as blurring) of the spatial domain regularization filter are minimized. It can be observed from Fig.4 that boundaries around teeth become sharper as the penalization is reduced.

III. RESULTS

In Fig. 3, we show the simulation results with different amounts of dental metal fillings and Gaussian noise contamination. From visual inspection of reconstructed images, it can be concluded that sequentially applied MAP-EM significantly reduces the blurring caused by the regularization in image reconstruction. In order to evaluate the performance of the algorithm quantitatively, percentage normalized mean squared error (NMSE%) was calculated with respect to the ground truth jaw image with the following formula

$$NMSE\%(I_{rec}, I_{gnd}) = \frac{\sum_{x=1}^M \sum_{y=1}^N [I_{rec}(x, y) - I_{gnd}(x, y)]^2}{\sum_{x=1}^M \sum_{y=1}^N [I_{gnd}(x, y)]^2} \times 100\% \quad (2)$$

where I_{rec} is the reconstructed images obtained from sequentially applied MAP-EM and I_{gnd} is the ground truth phantom image with no metals. Teeth region was chosen as region of interest (ROI) for this calculation because that region was affected the most by the metal artifacts. NMSE% values for 1, 6 and 14 metal levels are shown in Fig. 5.

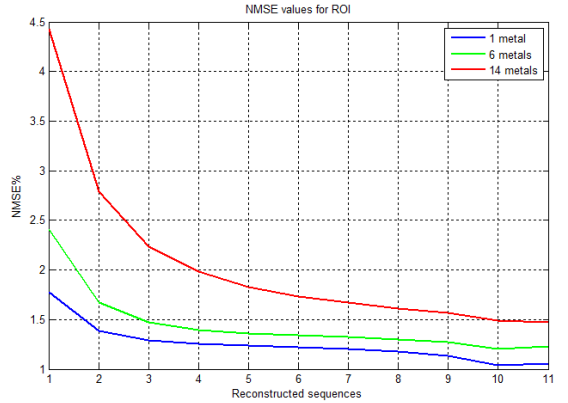
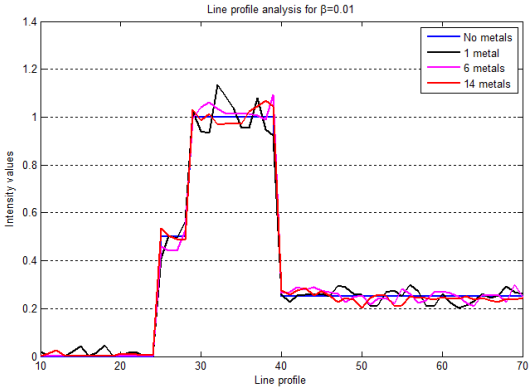
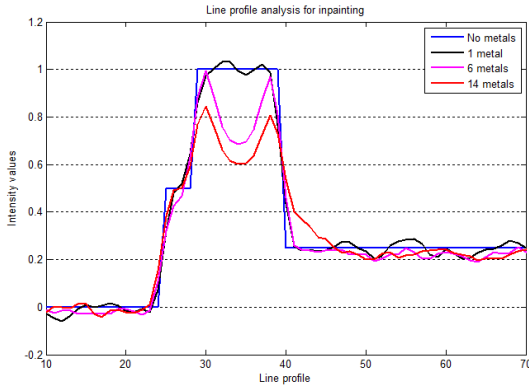


Fig. 5. NMSE% values for different level of metals in the numerical jaw phantom for selected ROI with respect to 11 β values. Blurring caused by the noise in the initial images is later compensated, which leads to a lower NMSE%.

Fig. 5 indicates that NMSE% converge and become stable even for 14-metal case as iterations continue throughout decreasing β values in sequentially applied MAP-EM. In addition to the NMSE% calculations, we have also performed line profile analysis for different metal cases (see Fig.6). Green line in Fig.3 was used for calculating the line profiles of the images. Efficiency of sequentially applied MAP-EM was compared with the results from inpainting, which is the most common reconstruction algorithm in clinical applications. The inpainting method was applied on the noisy sinograms, where extracted metals are assigned to Not-a-Number (NaN). NaNs were later replaced by estimates from interpolation, calculated by using springs metaphor, which assumes each node is connected to its neighbors with springs of nominal length 0 [10]. As number of metals/missing data increases in the phantom, intensity values deviate more from the ground truth value.



(a)



(b)

Fig. 6. Line profile analysis for (a) $\beta = 0.01$ for 1, 6 and 14 metal cases on the left half of the noisy numerical jaw phantom for image clarity. Line profile for the ground truth image is depicted in blue. Results of inpainting on the noisy jaw phantom for different amount of metals is also depicted in (b). Increased deviation for low β can be explained by the dominating effect of noise as a result of the trade-off between noise reduction and image sharpness. Sequentially applied MAP-EM performs significantly better than inpainting in recovering the intensity values for both β values.

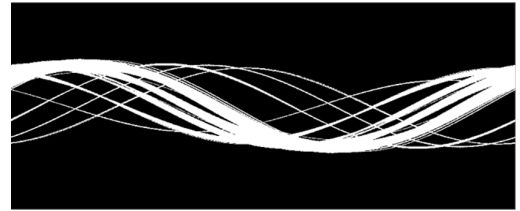
According to the line profile comparisons in Fig.6, deviation from ground truth value, 1, for 1-metal case is higher than other metal cases. Also as amount of metals in the phantom increases, deviation decreases, indicating a stronger effect of regularization. Decrease in β makes the resulting images sharper, along with a slight increase in deviation. Inpainting results indicate good reconstruction quality with values close to the ground truth image for a few metals. However, with the increased amount of metals, reconstructed intensities get as low as 60% of the original value. When Fig.6 (a) and (b) are compared, it is clearly visible that the sequential MAP-EM results in closer values to the ground truth with respect to inpainting.

We later applied the multi-level segmentation on a real full angle cone-beam CT (CBCT) phantom measurement acquired

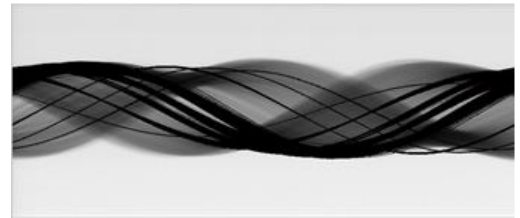
from Planmeca 3D Max CBCT (Planmeca Ltd, Helsinki, Finland). The phantom used for this measurement consisted of a gypsum base and braces made of steel. Constructed sinogram from the 3D data is shown in Fig.7 with 750 angular views and 368 radial bins. Binary image of Segmented metallic regions and these regions overlaid on the original image can be seen from Fig.7.(b) and (c).



(a)



(b)



(c)

Fig. 7: (a) Constructed sinogram of size 750 angular views and 368 radial bins, (b) extracted regions after multi-level sinogram segmentation, (c) segmented regions overlaid on the original sinogram. Overlaid image shows the accurate detection of metals as there are no metallic regions left undetected.

IV. DISCUSSION AND CONCLUSION

This study shows how sequentially applied MAP-EM enhances the image quality once the metals are accurately segmented from the numerical jaw phantoms. As penalization in MAP-EM was reduced, details such as boundaries around teeth became more visible. Also boundaries between different regions such as jaw bone and soft tissue were sharper for lower β . Larger amount of metals resulted in higher NMSE% in general, which was expected as the amount of missing data increased depending on the number of metals in the phantom. Initial high NMSE% in Fig. 5, which was caused by the added noise, was reduced throughout the iterations, leading to a stable and convergent NMSE% value for all phantoms. Fluctuation in line profile analysis for $\beta = 0.01$ is originated from the trade-off between blurring and noise. Performance of the reconstruction can be improved by optimizing the

iterations and β sequences in MAP-EM. Nevertheless, compared to the initial ratio of 10:1 between metal and teeth intensities, deviation remains low, indicating an accurate reconstruction. For the real jaw phantom, it can be said that segmentation step was accomplished so that all metallic regions are extracted from the original sinogram.

Despite of the speed and efficiency of inpainting in general, it is visible from Fig.6 that increased number of metals in the image data starts reducing the performance of the algorithm. For higher levels of missing data, sequentially applied MAP-EM outperforms inpainting.

In overall, proposed multi-level segmentation was successful for extraction of all metals from noisy jaw phantom and sequentially applied MAP-EM was successfully employed on sinograms, where missing information from the metals were estimated accurately.

REFERENCES

- [1] H. Xue, L. Zhang, Y. Xiao, Z. Chen, and Y. Xing, "Metal artifact reduction in dual energy CT by sinogram segmentation based on active contour model and TV inpainting," *Nuclear Science Symposium and Medical Imaging Conference (NSS/MIC), 2009 IEEE*, pp. 904-908, 2009.
- [2] A. Amirkhanov, C. Heinzl, M. Reiter, J. Kastner, and M. E. Göller, "Projection-Based Metal-Artifact Reduction for Industrial 3D X-ray Computed Tomography," *IEEE Transactions on Visualization and Computer Graphics*, vol. 17, no. 12, pp. 2193-2202, December 2011.
- [3] U. Tuna and U. Ruotsalainen, "Metal Artifact Reduction with DCT-Domain Gap-Filling Method," *IEEE Nuclear Science Symposium & Medical Imaging Conference Record (MIC2012)*, pp. 2322-2324, Anaheim, CA, USA, 29 October - 03 November 2012.
- [4] U. Heil, D. Gross, R. Schulze, U. Schwanecke, and E. Schömer, "Metal artifact reduction in X-ray computed tomography: inpainting versus missing value," *Nuclear Science Symposium and Medical Imaging Conference (NSS/MIC), 2011 IEEE*, pp. 2675-2677, 2011.
- [5] E. Meyer, R. Raupach, B. Schmidt, A. H. Mahnken, and M. Kachelrieß, "Adaptive normalized metal artifact reduction (ANMAR) in computed tomography," *Nuclear Science Symposium and Medical Imaging Conference (NSS/MIC), 2011 IEEE*, pp. 2560-2565, 2011.
- [6] M. Abdoli, M. R. Ay, A. Ahmadian, and H. Zaidi, "Reduction of dental filling metallic artifacts in CT-based attenuation correction of PET data using weighted virtual sinograms," *Nuclear Science Symposium Conference Record (NSS/MIC), 2009 IEEE*, pp. 2752-2755, 2009.
- [7] M. Oehler and T. M. Buzug, "The λ -MLEM Algorithm: An Iterative Reconstruction Technique for Metal Artifact Reduction in CT Images," *Advances in Medical Engineering*, pp. 42-47, 2007.
- [8] N. Otsu, "A Threshold Selection Method from Gray-Level Histograms," *IEEE Transactions on Systems, Man, and Cybernetics*, vol. 9, no. 1, pp. 62-66, January 1979.
- [9] U. Tuna, A. Pepe, and U. Ruotsalainen, "Sequential regularized MLEM reconstruction method for incomplete sinograms," *IEEE Nuclear Science Symposium & Medical Imaging Conference Record (MIC2011)*, pp. 2553 - 2557, Valencia, Spain, 23 - 29 October 2011.
- [10] M. Bertalmio, G. Sapiro, V. Caselles and C. Ballester, "Image Inpainting," *Proceedings of SIGGRAPH 2000*, New Orleans, USA, July 2000.

PUBLICATION

II

AvanTomography: A Compact Module for Positron Emission Mammography

D. Us, A. Moreno-Galera, S. Nazari-Farsani, K. Palovuori, H. Kosola, T. Zedda,
U. Ruotsalainen

IEEE International Symposium on Medical Measurements and Applications, MeMeA 2015 –
Proceedings, pp. 52--57, May 2015, Turin, Italy

[10.1109/MeMeA.2015.7145171](https://doi.org/10.1109/MeMeA.2015.7145171)

Publication reprinted with the permission of the copyright holders.

© 2015 IEEE

AvanTomography: A Compact Module for Positron Emission Mammography

D. Us, *Student Member, IEEE*, A. Moreno-Galera, *Member, IEEE*, S. Nazari-Farsani, K. Palovuori, H. Kosola, T. Zedda, U. Ruotsalainen, *Member, IEEE*

Abstract— In AvanTomography project, a compact, high performance module was developed for axial positron emission mammography, which can be integrated with X-ray mammography. With its axial crystal orientation, AvanTomography can achieve a uniform spatial resolution and eliminate the parallax error by unambiguously detecting the location of the positron annihilation. Compact design of the module enables a cost and space efficient system for breast screening. Various configurations, plate or full ring, can be obtained by using multiple modules, allowing the screening of axillary and mammary regions with a single scanner position. In this project, a 6-module system was constructed and tested with a ^{22}Na point source. Energy calibration was performed and initial measurements for energy resolution were conducted.

Index Terms— Positron Emission Tomography (PET), Axial geometry, LYSO, Positron Emission Mammography (PEM), breast cancer, pulse width conversion.

I. INTRODUCTION

With its functional imaging capabilities, Positron Emission Tomography (PET) provides a cost-effective alternative to invasive procedures such as dissections and biopsies that are used for cancer staging and treatment planning, which is not possible to obtain with structural imaging methods like X-ray Computed Tomography (X-ray CT) or Magnetic Resonance Imaging (MRI). Localized screening techniques like Positron Emission Mammography (PEM) improve the overall sensitivity, which was demonstrated by Berg *et al.* [1]. This is mainly due to the increased sensitivity in PEM by (1) closer placement of detectors to the breast and (2) less amount of tissue travelled by the gamma rays, leading to lower dose of radiotracer injection [2]. Unfortunately, most of these breast PET scanners have the inherited problem of excluding the base of

the breast, the axillary tail and the lymph nodes [3]. As sentinel lymph node mapping is an important tool in early staging of breast cancer, it is important to include the axillary region into the screening procedure. Mammary and axillary PET (maxPET) addresses this issue with its large field of view (FOV), where the patient is scanned in prone position with two different scanner placements [4]. However, 65% of the scintillation signal is lost between the coupling of crystal array and photomultiplier (PM) tubes. Furthermore, the count rate is limited as a result of multiplexed readout [4]. Another example of PEM is Mammography with Nuclear Imaging (MAMMI-PEM) from Oncovision (Valencia, Spain), which has a 1.6 mm spatial resolution at the center, but the resolution is lowered to 2.7 mm at the edges of the FOV [5]. We aim to achieve a high count rate by reading each channel individually, limiting the data rate by thresholding in electronics and accomplish uniform resolution with axial placement of the scintillating crystals within the modules.

II. AVANTOMOGRAPHY

The aim of AvanTomography modules is to provide an alternative compact configuration for breast screening by incorporating Axial PET (AX-PET) concept implemented in CERN within a compact module. These modules are planned to be used in construction of a PEM. Mechanically and electronically independent modules provide a flexible structure, with which the gantry size of the scanner can be arranged by changing the number of modules used. Compact structure of AvanTomography modules make it a suitable candidate for smaller clinics, where a cost and space efficient pre-screening instrument is much needed in order to overcome the limitations of MRI or whole body PET/CT.

Inner structure of a single AvanTomography module is depicted in Fig. 1.

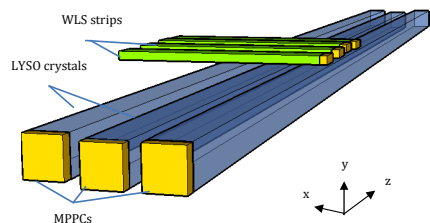


Fig. 1. AvanTomography module inner structure, depicting the WLS strips orthogonally placed over the LYSO crystals. Both LYSO crystals and WLS strips are read out with MPPCs from one end.

According to the work of Beltrame *et al.*, AX-PET configuration offers a parallax-free scanner alternative with precise 3 dimensional (3D) localization of the point of positron annihilation. The main difference of AX-PET concept

This project was supported by Tekes funding number 360/31/2013.

D. Us, A. Moreno-Galera, U. Ruotsalainen, are with Department of Signal Processing, Tampere University of Technology, FI-33720, Tampere, Finland (e-mail: author@tut.fi).

S. Nazari-Farsani was with Department of Signal Processing, Tampere University of Technology, FI-33720, Tampere, Finland. She is now with Åbo University, Domkyrkotorget 3, 20500 Turku, Finland (e-mail: author@utu.fi).

T. Zedda was with Department of Signal Processing, Tampere University of Technology, FI-33720, Tampere, Finland. She is now with Department of Biomedical Engineering, Ghent University, 9000 Ghent, Belgium (e-mail: author@ugent.be).

Karri Palovuori is with Department of Electronics, Tampere University of Technology, FI-33720, Tampere, Finland (e-mail: author@tut.fi).

Heikki Kosola was with Department of Electronics, Tampere University of Technology, FI-33720, Tampere, Finland. He is now with Icraft Oy, FI-33100, Tampere, Finland (email: author@icraft.fi).

from the conventional PET geometry is that the scintillating crystals are placed in the axial direction instead of conventional radial arrangement. Crystal layers are interleaved with an array of wavelength shifter (WLS) strips, placed orthogonal to the crystals. Both crystals and WLS strips are read out by multi pixel photon counters (MPPCs) at one end. When a photon deposits its energy in the crystal, a correlated amount of light is isotropically emitted. Emitted light is captured by WLS strips. The signals from WLS strips and crystals are captured by the MPPCs, which are used to determine the 3D coordinate of the photon interaction. In this configuration, the axial coordinate is recorded continuously along the scintillating crystals. Position of the crystal provides the hit location in x and y axes, whereas z axis is obtained from WLS strips. Intersection point of the positions of a LYSO and a WLS strip results in the 3D coordinate of the annihilation. The mid-point of WLS and LYSO are used in determination of the annihilation coordinates. [6]

AvanTomography modules improve the previous design in AX-PET by making it compact, without compromising the sensitivity, energy resolution and spatial resolution [7] [8] [9] [10].

The potential of Axial PET geometry for brain imaging has been verified in AXPET project [6]. Also Brard and Brasse presented their Monte Carlo simulation results for a small animal PET scanner with axial PET configuration to achieve a spatial resolution less than 1 mm. The proof-of-concept level study in GATE showed that it is possible to go below 1 mm by using One-Pass List-Mode reconstruction algorithm [11].

For breast screening purposes, target spatial resolution for the AvanTomography demonstrator was decided as approximately 1.5 mm, which is sufficient to detect small tumors (3mm and below) [2]. In this project, the focus was on implementing this design with smaller, low-cost modules with independent electronics to be used for PEM. In this article, the mechanical and electronics construction are described. Experimental performance of the 6-module system is presented.

III. AVANTOMOGRAPHY MODULES SETUP

AvanTomography modules consist of WLS strips, scintillating crystals and MPPCs. The data acquisition part of the system includes a bias board, pulse width conversion circuits and digital electronics boards for transmission of energy (converted from charge during post-processing) and location information. In this section, data acquisition components are described in detail. A simplified configuration of a module with its respective electronics is depicted in Fig. 2.

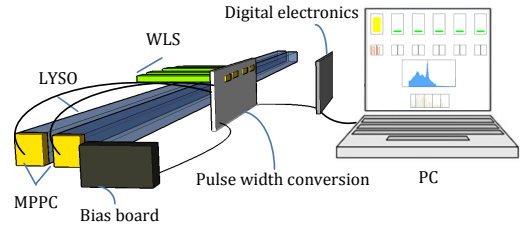


Fig. 2. Simplified module measurement setup including the basic components of the module as well as the data acquisition system.

A. Components

The scintillating bars used in AvanTomography modules were PreLude®420 Lu 1.8Y₂SiO₅:Ce crystals (LYSO) produced by Saint-Gobain Crystals, with maximum emission at around 420 nm. Crystals are of size 3x3x150 mm³ and all surfaces are optically polished by the manufacturer, with a density of 7.1 g/cm³. Wavelength shifting (WLS) strips are EJ-260-10 from Eljen Technology, which is based on Polyvinyltoluene (PVL) with high dye concentration, with a maximum emission at a wavelength of 490 nm. Photodetectors used in this demonstrator are fast Geiger-mode Avalanche photodiodes (S12572-050P) from Hamamatsu Photonics, marketed as Multi-pixel Photon Counter (MPPC)[®]. MPPCs have an active area of 3x3 mm² with 50x50 μm² pixel size. Photodetection efficiency (PDE) of the MPPCs is maximum around 420 nm at 25°C, which is compatible with the emission spectrum of the LYSOs.

B. Read-out Electronics

Bias circuit: All MPPCs received for this project require an average of 67 Volts (operating voltage + diode activation) as their operating (bias) voltage. Therefore, all modules are supplied with the same bias voltage generated by a single bias circuit. Bias circuit consists of a rectification stage and a resistive feedback circuit. The rectification part includes a gated oscillator boost controller (MCP1650 Microchip Technology Inc.) with a low operating current around 120 μA and 56% duty cycle, an inductor, a Schottky diode and a transistor IRLML0100 from International Rectifier. The oscillator is switched on and off with a 750 kHz switching frequency, decreasing the external capacitor and inductor of the component smaller in size, making it ideal for our space limited design. When the oscillator (U_1 in Fig. 3) is switched on, I_C flows into the inductor (L_1 in Fig. 3), in which case the MOSFET (Q_1 in Fig. 3) is OFF and one end of L_1 is grounded. When U_1 is switched off, $I_C = 0$ and the current collected in L_1 flows through C_2 via the Schottky diode D_1 . D_1 prevents the back-flow of the current into the inductor. This way all current collected in L_1 piles up in C_2 (V_{BIAS}). Through the resistive feedback circuit, small portion of V_C is fed back to the feedback pin of U_1 . When the feedback voltage reaches 1.22 Volts, U_1 stops switching. At this point V_{BIAS} equals to 67.7 Volts in the ideal setting. Taking the MPPC temperature sensitivity into consideration, V_{BIAS} can be changed with the potentiometer within the resistive feedback circuitry. This

alters the feedback voltage at which U_1 stops operating, thus changing the amount of charge collected within C_2 . The bias board has a typical 1 mA output current, most of which is consumed by the resistive feedback circuit.

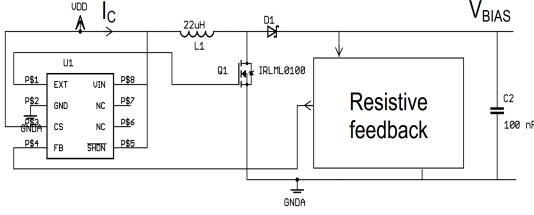


Fig. 3. Bias circuit formed with a rectification stage and a resistive feedback loop.

Sensor boards (Pulse width conversion): The sensor boards receives the signal from the MPPCs and convert it into varying pulse lengths. The circuit design for sensor boards is based on charge-to-time conversion circuit suggested in the work of Parl *et al.* [12]. In this scheme, pulse width is correlated with the amount of charge detected by the photodetectors. Although individual photons are counted in the design of Parl *et al.*, our circuit detects the photon bursts, meaning that the circuit sensitivity is arranged so that only large enough (eliminating noise and misfired MPPCs) pulses pass through the comparator stage and transmitted to the digital acquisition part, eliminating the effect of noise from the beginning. Due to the higher photon-detection threshold voltage set by V_{THRESH} in the circuit, even though the relationship between the charge and pulse width is linear, there is a higher offset observed [12].

Due to large amount of data and the space limitation, complexity of electronics per channel was kept as low as possible. Differently from the circuitry in AX-PET, no shaper was used for simplicity and minimal delay in the system. Also no trigger was implemented since the system collects all the information above the hardcoded threshold once it is turned on. Due to the high gain of MPPCs, primary amplifiers were not needed. Each integrating amplifier output is thresholded and buffered similarly to [12].

Reference pulse time was calculated based on the number of counts in AX-PET simulations [9]. According to the expected count rates for LYSOs and WLSs, the amount of charge for full width half maximum (FWHM) of the reference charge was set to 26.2 pC (approximately 133 counts). For a reference pulse length of 100 ns, the pulse current was calculated to be 266 μ A.

Each 10-channel circuitry within a module was grouped and assembled together on a printed circuit board (PCB), avoiding the risk of mismatch between MPPC slots and MPPCs due to the different thermal expansion coefficients of the PCBs and module container.

Temperature compensation: Linearity over the dynamic range is necessary for accurate energy calibration and measurements. Unfortunately, MPPCs are sensitive to temperature change [13]. Therefore, the bias circuitry is arranged so that the operating voltage of the MPPCs can be adjusted. MPPCs are supplied with an initial 67.7 V, and the bias voltage can manually be changed within the range of 65-75 V with a potentiometer connected between the temperature sensing

circuit and the resistive feedback circuit in the bias circuitry. 1°C temperature increase in the system can be compensated with a 60 mV increase in the bias voltage [12].

In the work of Parl *et al.*, an integrating stage was used as a part of temperature compensation by changing V_{COMP} in [12] with respect to temperature, but this requires a higher operating voltage for the operational amplifier (op-amp), increasing the energy consumption and causing heating of the op-amps. In order to keep the system with low power consumption and to avoid cooling the individual op-amps, we used a constant V_{COMP} (lower than [12]) and implemented the temperature compensation feature by changing the bias voltage of MPPCs. This modification eliminates the need for heat sinks around the op-amps, making the electronics design more compact.

Temperature compensation unit includes a low power microcontroller (ATtiny43U) from Atmel Corporation® (California, USA) equipped with a temperature sensor. ATtiny43U is placed next to one sensor board (second module, layer 8-9) so that its temperature is approximately the same as the temperature of the sensor board. The temperature of the microcontroller is converted into a pulse width modulated signal between zero and operating voltage [0,5V]. This voltage is then discretized by the low pass filter connected to it. Output of the filter is connected to the bias circuit with a potentiometer so that the feedback voltage fed to the boost controller changes according to the resistance of the potentiometer.

C. Digital electronics

Charge information from each channel is obtained by integrating the pulse widths received from the sensor boards. Corresponding energy peaks are calculated according to the energy calibration curve based on the intrinsic radioactivity peaks of LYSO and 511 keV.

A Cyclone FPGA from Altera is used for processing the charge information. One layer of LYSOs and associated WLSs use the same FPGA, totaling into 12 FPGA modules, each handling 48-49 channels.

WLSs are only used for position detection, therefore their timing window is held larger than LYSOs in order to decrease the data rate. A time stamp is assigned to each event detected by the MPPCs within a timing window of 10 ns for WLS and 2.5 ns for LYSOs. Each event is defined by 6-bytes: 1 byte for preamble, 1 byte for localization of the channel (layer number within module, LYSO number and WLS number in corresponding layer), 2 bytes for the event time stamp and 2 bytes for charge information. A priority system is established between the FPGAs so that information can be transferred without overwriting on the other channels. As the FPGAs are set to give priority to the incoming data, it is important to keep the data rate high enough to prevent overflowing. Every 2 FPGA form digital read-out for a module and are connected to the computer with a separate USB serial port for initial experiments. Acquired data from the measurements is organized into list mode data format in order to enable the continuous input data for reconstruction.

In order to check the activity levels of all channels in real-time and provide effective troubleshooting of the system during the measurements, a serial log file was prepared in

Visual Studio as a user interface. Data bandwidth consumption in each module is displayed as well as LYSO and WLS activity levels. Each LYSO channel can be selected in order to visualize its respective histogram and the corresponding WLS activities. Connectivity of the MPPCs to the LYSOs and WLSs can be tracked via this interface. Also the defective channels can easily be distinguished from the active ones by following the activity peaks. An example screenshot is depicted in Fig. 4. Note that the histogram is displayed cumulatively; therefore the plot is only reset when a different LYSO is selected. Due to the threshold value used in the electronics to eliminate the background, the histogram values lower than the threshold can be seen as zero in Fig. 4.

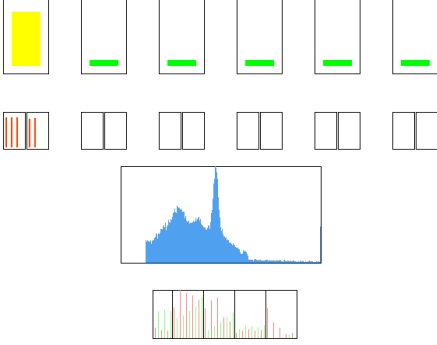


Fig. 4. Screenshot from individual testing of a module with ^{22}Na source placed 1 cm away from the module in total darkness. The first row shows the bandwidth consumption of the module. Second row indicates the activity levels of the LYSOs. Third row shows the histogram of the chosen LYSO (in this case layer 0, crystal 0). The last row represents the WLS activity for each LYSO. WLS activity is divided into 4 slots, where each slot corresponds to a sensor board. Notice that 511 keV peak is clearly seen from the histogram.

In the future, an Ethernet connection can be established instead of multiple serial port connections, enabling a more versatile design for future applications.

D. Module description

The AvanTomography measurement configuration includes 6 modules with independent customized electronics for each module. Each module consists of 97 channels (5 LYSO crystals and 92 WLS strips) and is divided into two layers. A black non-conductive and non-transparent Polyacetal-Copolymer (POM) container with 2 LYSOs is mounted on top of another container with 3 LYSOs in order to prevent light sharing from crystals in different layers. Inside the modules, LYSOs are placed with an air gap of 1 mm from each other in a layer. One end of the crystals and WLSs are optically coupled to the MPPCs with optically clear adhesive, having a light transmission efficiency of approximately 99% [14]. The other ends of the crystals and WLSs are covered with a non-metallic reflective film. Each layer of LYSO is covered with WLSs with a gap of 6 mm from the MPPC side and 9 mm from the reflective films for accommodating the metal frames holding 2 and 3 crystals in upper and lower layers respectively. LYSOs inside the module are held in place with metal plates from both ends in order to minimize the movement of crystals and contact with the module container.

Due to the minimal contact achieved, LYSOs were not wrapped or coated. Each MPPC is placed inside a specific slot in the container, which prevents the motion of MPPCs and avoids electrical conduction or propagation between two adjacent MPPCs.

E. Measurement Setup

6 of above-mentioned modules were constructed and tested for this demonstrator setup. Energy calibration was performed for each crystal. Performance of the overall system was tested in terms of energy resolution and sensitivity. In the calculation of the overall energy resolution, results obtained from all the crystals were averaged. The overall structure of the system is demonstrated in Fig. 5.

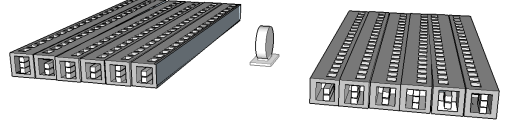


Fig. 5. 6-module configuration of AvanTomography. A module consists of one 2 crystal layer and one 3 crystal layer placed in a staggered way. WLS strips are not shown in this image for clarity purposes, but the MPPC slots are visible.

III. MODULE CHARACTERIZATION

A. Detection efficiency

The spatial information of the photoelectric events varies according to the detection axis. The point of interaction (POI) in the trans-axial coordinates is the center of the photoelectric impact. Collision points of the events were calculated following the above statements. Fig. 6 shows the impact statistics in percentage scale. According to the LYSO and WLS configuration per layer, the minimum binning size was calculated as 1.85 mm for the y coordinate and 0.5 mm for the z coordinate.

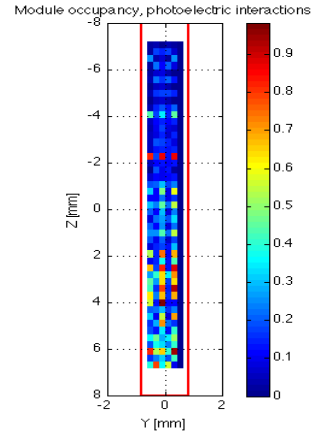


Fig. 6. Study of the positron collision positions in percentage over the total statistical events. Y and z coordinates are determined according to the module orientation given in Fig. 1.

Fig. 6 shows that the LYSOs closer to the source are more active than the lower layers, which creates photoelectric

clusters. On the other hand, the WLSs close to MPPCs are more active and detect more positrons than the ones further away. This is due to the digital electronics reading, where the first detected WLS is recorded and the rest is ignored. Naturally, the signal from the WLSs closest to the MPPCs reach the detectors faster than the further ones. Although this setup is used to decrease the data amount in the initial measurements, future electronics will be designed to read all channels at all times in order to avoid loss of data.

B. Energy calibration

The energy calibration of the LYSOs is required so that data acquired from each crystal can be corrected for individual differences in the electronics and non-linearity in MPPC response [6]. It also enables a more precise localization of the energy peak in the overall system. The intrinsic activity of LYSO was taken as 39 cps/g [15]. For 30 crystals used in this project, the total activity was calculated to be around 11.25 kBq (374 Bq of β^- decays for a single crystal) [15]. All crystals were stacked together in order to increase the probability of photon absorption and the radioactivity was measured from all crystals.

Intrinsic radioactivity measurements for energy calibration were run for 1 hour in complete darkness with an integration time of 10 μ s and bias voltage of 67.7 V. The location of intrinsic energy peaks of the LYSOs were characterized in pC for each crystal. The measurement result from one LYSO can be seen in Fig. 7. Although the two highest peaks of typical de-excitation of ^{176}Lu (202 keV and 307 keV) are clearly visible in the spectrum, the lowest de-excitation photon at 88 keV cannot be seen due to its high internal conversion probability [6]. Instead, the third peak with the lowest energy is attributed to the x-ray emission from the K-shell of the ^{176}Lu , corresponding to the energy peak of 55 keV observed in the spectrum. [15]

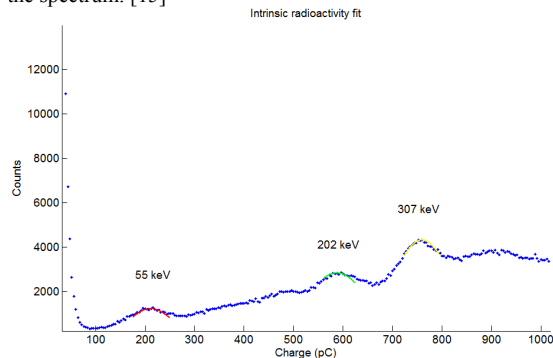


Fig. 7. Gaussian fits superimposed on the intrinsic radioactivity peaks of ^{176}Lu at 202 and 307 keV on the charge spectrum of middle LYSO (LYSO 10). The peak at 55 keV is generated by the x-ray emission the K-shell of the lutetium.

In order to measure the 511 keV photons absorbed by the LYSOs, a 675 kBq point-like ^{22}Na source was placed in the center of FOV with a distance of 12 cm from the closest module. Fig. 8 shows the 511 keV peak measured from LYSO 10 and the nonlinear curve fit, which is 30 cm far from the ^{22}Na source.

Mean charge values, derived from the Gaussian fits in charge spectrums of intrinsic radioactivity measurements of LYSO and 511 keV measurements in Fig. 7 and Fig. 8 respectively, were translated into their corresponding energy peak values and used for calibrating the LYSO channels individually.

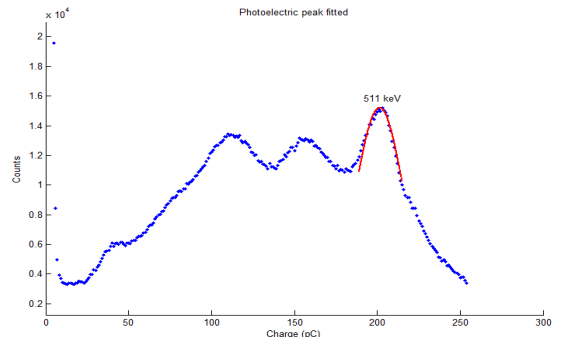


Fig. 8. The counts for the 511 keV radioactivity peak value is quite close to the intrinsic radioactivity peaks for this crystal as the detected counts by the crystal are not very high due to the distance from the source.

A non-linear fit was calculated from the three intrinsic radioactivity peaks and the 511 keV peak by modification of the calculations from [15]. The results from this fitting can be observed in Fig. 9. Initial measurements lead to a 9.5% deviation from linearity in average for all crystals.

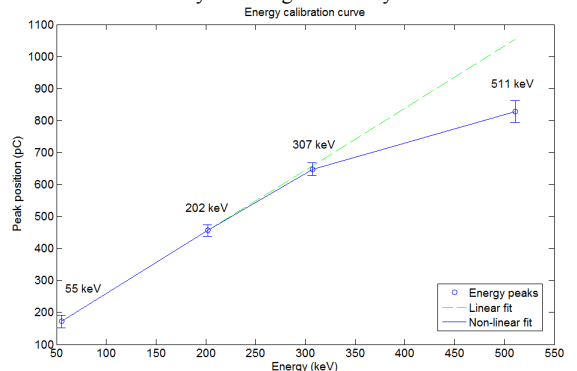


Fig. 9. Nonlinear fitting curve along the intrinsic radioactivity and 511 keV peaks (LYSO 10). The correlation coefficient R was calculated as 0.926.

IV. CONCLUSION

During the AvanTomography project, 6 modules were successfully built and tested. Preliminary results indicate an energy resolution of around 14% FWHM in the sum which was similar to 12.5% in the sum that was obtained with AX-PET from initial measurements [16]. This result is expected to improve with better temperature compensation as well as the use of optical glue between the components instead of the double sided tape. The next step will be to compare the experimental sensitivity with the simulation results obtained from Monte Carlo simulations by using Geant4. Additionally, separate bias boards for individual modules might be required

in order to ensure the temperature compensation of channels with high count rates.

AvanTomography module offers a parallax-free, cost-effective alternative to large and expensive PEM units. Also mechanical and electrical independence of each module enables personalization of the scanner depending on the desired use.

ACKNOWLEDGMENT

We are grateful to Uygur Tuna, Viivi Nuottajärvi, Antti Nuottajärvi, and Chiara Casella for their contributions and supervision during the project.

REFERENCES

- [1] W. Berg, K. J. Schilling, M. Tartar, J. E. Kalinyak and K. S. Madsen, "Comparison of Positron Emission Mammography and Whole Body PET in Breast Cancer Surgical Planning," in *RSNA 96th Scientific Assembly and Annual Meeting*, Chicago, 2010.
- [2] W. W. Moses, "Positron Emission Mammography imaging," *Nuclear Instruments and Methods in Physics Research A*, vol. 525, pp. 249-252, 2004.
- [3] R. Freifelder and J. S. Karp, "A Dedicated PET Scanner for Breast Cancer," in *Nuclear Science Symposium and Medical Imaging Conference Record*, San Francisco, 1995.
- [4] N. K. Doshi, R. W. Silverman, Y. Shao and S. R. Cherry, "maxPET: A Dedicated Mammary and Axillary Region PET Imaging System for Breast Cancer," *IEEE Transactions on Nuclear Science*, vol. 48, no. 3, pp. 811-815, 2001.
- [5] B. Koolen, T. Aukema, A. G. Martinez, W. Vogel, L. C. Ontanaya, M. V. Peeters, C. Vroonland, E. Rutgers, J. B. Baviera and R. V. Olmos, "First clinical experience with a dedicated PET for hanging breast molecular imaging," *The Quarterly Journal of Nuclear Medicine and Molecular Imaging*, vol. 56, pp. 92-100, 2012.
- [6] P. Beltrame, E. Bolle, A. Braem, C. Casella, E. Chesi, N. Clinthorne, R. D. Leo, G. Dissertori, L. Djambazov, V. Fanti, M. Heller, C. Joram, H. Kagan, W. Lustermann, F. Meddi, E. Nappi, F. Nessi-Tedaldi, J. Oliver, F. Pauss, M. Rafecas and D. Renker, "The AX-PET demonstrator - Design, construction and characterization," *Nuclear Instruments and Methods in Physics Research*, vol. 654, pp. 546-559, 2011.
- [7] A. Braem, C. Joram, J. Seguinot, G. Dissertori, L. Djambazov, W. Lustermann and F. Nessi-Tedaldi, "AX-PET: A novel PET detector concept with full 3D reconstruction," *Nuclear Instruments and Methods in Research A*, vol. 610, pp. 192-195, 2009.
- [8] A. Braem, E. Chesi, C. Joram, J. Seguinot, P. Weilhammer, R. D. Leo and E. Nappi, "High precision axial coordinate readout for an axial 3-D PET detector module using a wave length shifter strip matrix," *Nuclear Instruments and Methods in Physics Research A*, vol. 580, pp. 1513-1521, 2007.
- [9] P. Beltrame, E. Bolle, A. Braem, C. Casella, E. Chesi and N. Clinthorne, "Demonstration of an Axial PET concept for brain and small animal imaging," *Nuclear Instruments and Methods in Research A*, vol. 628, pp. 426-429, 2011.
- [10] E. Bolle, C. Casella, E. Chesi, R. D. Leo, G. Dissertori, V. Fanti, J. Gillam, M. Heller, O. Holme, C. Joram, W. Lustermann, E. Nappi, J. Oliver, F. Pauss, M. Rafecas, U. Ruotsalainen, D. Schinzel and T. Schneider, "Long axial crystals for PET applications: The AX-PET demonstrator and beyond," in *Nuclear Science Symposium and Medical Imaging Conference (NSS/MIC)*, Seoul, 2013.
- [11] E. Brard and D. Brasse, "Axially Oriented Crystal Geometry Applied to Small-Animal PET System: Proof of Concept," *IEEE Transactions on Nuclear Science*, vol. 60, no. 3, pp. 1471-1477, 2013.
- [12] C. Parl, H. Larue, M. Streun, K. Ziemons and S. v. Waasen, "Fast Charge to Pulse Width Converter for Monolith PET Detector," *IEEE Transactions on Nuclear Science*, pp. 1809-1814, 9 October 2012.
- [13] H. Photonics, "MPPC, MPPC Modules," Hamamatsu Photonics Inc., Fukuoka.
- [14] 3M, "Optically Clear Adhesives 8171CL - 8172CL," February 2010. [Online]. Available: <http://solutions.3m.com>. [Accessed 25 August 2013].
- [15] T. Zedda, "Construction and Testing of a Positron Emission Tomography Demonstrator," MSc. Thesis, Tampere University of Technology, Tampere, 2013.
- [16] P. Beltrame, E. Bolle, A. Braem, C. Casella, E. Chesi, N. Clinthorne, R. De Leo, G. Dissertori, L. Djambazov, V. Fanti, C. Joram, H. Kagan, W. Lustermann, F. Meddi, E. Nappi, F. Nessi-Tedaldi, J. Oliver, F. Pauss, M. Rafecas, D. Renke, A. Rudge, D. Schinzel, T. Schenider, J. Seguinot, P. Solevi, S. Stapnes and P. Weilhammer, "First results from the AX-PET demonstrator," in *Nuclear Science Symposium Conference Record (NSS/MIC)*, Florida, 2009.

PUBLICATION

III

Metal Artifact Reduction Based on Automated Sinogram Segmentation and Adaptive Multiresolution MAP Reconstruction Method

D. Us, E. Acar, U. Ruotsalainen

2015 IEEE Nuclear Science Symposium and Medical Imaging Conference Record (NSS/MIC),
pp. 1--5 Nov 2015, San Diego, USA

[10.1109/NSSMIC.2015.7582104](https://doi.org/10.1109/NSSMIC.2015.7582104)

Publication reprinted with the permission of the copyright holders.

© 2015 IEEE

Metal Artifact Reduction Based on Automated Sinogram Segmentation and Adaptive Multiresolution MAP Reconstruction Method

Defne Us*, *Student Member*, Erman Acar*, and Ulla Ruotsalainen, *Member, IEEE*

Abstract: High density objects in the field of view (FOV) cause artifacts in medical imaging. In X-ray computed tomography (CT), there are several ways to eliminate the effects of these artifacts. This paper aims to evaluate the performance of a novel reconstruction algorithm which accurately segments the metallic regions and reconstruct sharp metal/tissue boundaries, while reducing the artifacts around the metallic regions. This algorithm uses a multilevel segmentation algorithm based on Otsu's threshold and adaptive multiresolution maximum a-posteriori expectation maximization (amMAP-EM). The qualities of Gaussian noise contaminated images were evaluated quantitatively using mean squared error and line profile analysis. The reconstructed image were compared with filtered backprojection (FBP) and maximum likelihood expectation maximization (MLEM) methods. According to the results, it is possible to reconstruct the images with more clear and sharper metal/tissue boundaries using amMAP-EM compared to MLEM and FBP, while avoiding the undesired artifacts such as blurring, streak artifacts or ringing.

I. INTRODUCTION

METALS and other high density objects within the human body hinder the underlying anatomical structures due to their high attenuation coefficients, allowing fewer photons to reach the detectors. In computed tomography (CT), this photon starvation corrupts the projection data, leading to streak artifacts over the surrounding hard and soft tissue upon back-projection algorithms. Strength and direction of the streak artifacts are greatly dependent on the shape, size and location of metals. As the number of metals increase, metal projections get rapidly wider, making it more difficult to distinguish metal imprints from each other and to handle the large area of missing data. Inaccurate localization of metallic objects in dental CT can be misleading in clinical applications such as treatment planning and post-therapy evaluation.

Metal artifact reduction (MAR) methods define a group of algorithms that are designed to reduce the artifacts in images by ignoring or replacing the values of highly attenuated regions. The two main MAR methods are sinogram interpolation and iterative reconstruction [1]. Inpainting is one of the most commonly used sinogram interpolation method. However when the metallic regions are replaced with interpolated values from the surrounding pixels, the boundaries between anatomical regions and the high density objects become unclear [2]. Although iterative algorithms are computationally heavier and more time consuming, they cope better with missing data compared to non-iterative algorithms.

The difference in performance becomes clearer as the amount of missing data increases. Currently the benchmarks are considered as filtered backprojection (FBP) among the non-iterative reconstruction algorithms, and maximum likelihood expectation maximization (MLEM) among the iterative reconstruction methods [3].

Aim of this paper is to present a MAR algorithm to reduce the artifacts around the metallic regions in dental CT images and to reconstruct clear and accurate metal/tissue boundaries. This method uses a multilevel segmentation method based on Otsu's threshold, followed by adaptive multiresolution method for adaptive multiresolution maximum a-posteriori expectation maximization (amMAP-EM), which calculates the regularization weights using a pixel-wise approach [4]. amMAP-EM uses the pixel-wise noise contamination to update the regularization weight, eliminating the need for a priori information on the image [4]. The long computation time of iterations is decreased by using multiresolution reconstruction scheme, in which the image is rebinned for from larger to smaller pixel groups. amMAP-EM was initially implemented for missing wedge problem in electron tomography (ET) in which an image can be reconstructed even if 60 degrees out of 180 are missing [5]. Due to its ability to handle large amounts of missing data, amMAP-EM was selected as the reconstruction algorithm in this paper, as the existence of multiple or large metals increase the amount of missing information in the sinogram after segmentation.

II. MATERIALS AND METHODS

4 numerical jaw phantoms¹ were created for the initial evaluation of the algorithm performances. The sinograms were calculated with 256 radial bins over 180 degrees using 288 angular views. Each jaw phantom consisted of different numbers of metals to test the effect of multiple metals with relative sizes compared to the surrounding teeth in segmentation and image reconstruction algorithms.

* Authors have equal contribution to the paper.

This project was supported by The TUT Rector's Graduate School and NOVAC project.

Defne Us, Erman Acar and Ulla Ruotsalainen are with the Department of Signal Processing, Tampere University of Technology, P.O. BOX 533, FIN-33101, BioMediTech, Tampere, Finland (e-mail: firstname.surname@tut.fi).

¹ Oliver Watzke, IMP, Erlangen, Germany
<http://www.imp.uni-erlangen.de/phantoms/jaw/jaw.htm>

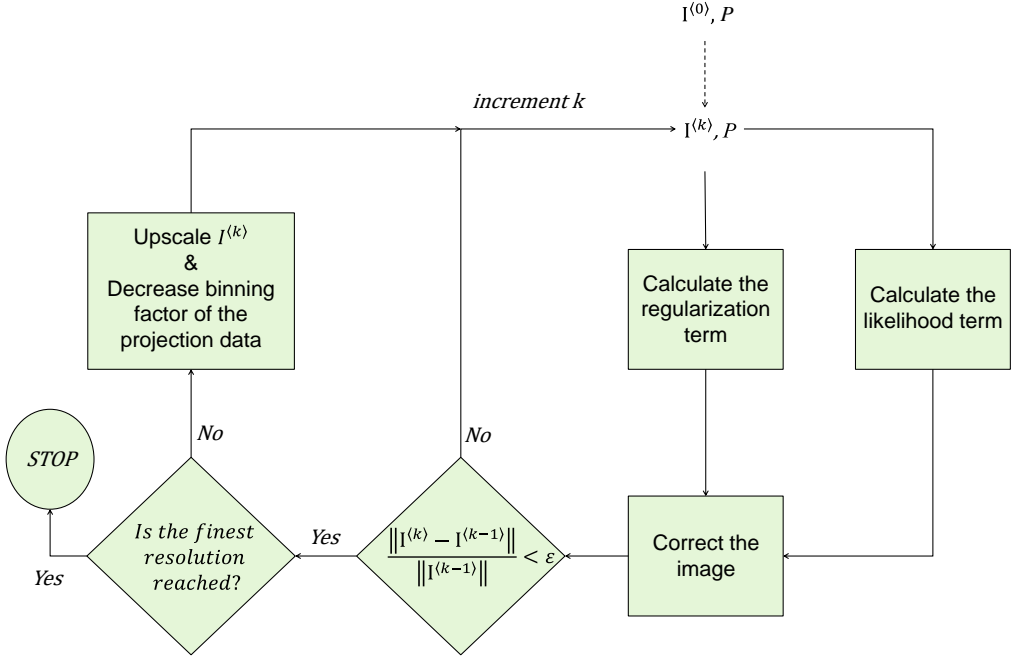


Fig. 1. Block diagram of amMAP-EM reconstruction algorithm [4]. $I^{(0)}$ is the image reconstructed at k th iteration, P is the masked projection data. This method takes the masked sinogram as input, in which metal values are replaced with zeros [block diagram can be enlarged to occupy both columns later like Fig.2.]

Biological structure densities were assigned to be proportional to the values used by Oliver Watzke, within the intensity range of [0, 1]. Metals in these phantoms were assumed to have 10 times higher intensity than the enamel so as to have a realistic relationship between the structure densities in the image. Gaussian noise was added to all phantoms. Different metal placements are shown in Fig. 2.

In order to localize the metals in the projection data, we used an automated multilevel segmentation algorithm that is based on Otsu's thresholding, which aims to minimize the in-class variance within the image [6, 7]. A multilevel segmentation was chosen because Otsu's thresholding method does not work efficiently if two classes are highly different in size, in which case the selected maximum mean value might not be the global maximum, causing the Otsu's threshold to be the valley of the sinogram [8]. As the accurate detection of metallic boundaries is crucial in assessing the image quality at the vicinity of the metals, we focused on the correct segmentation of the metallic region boundaries and reconstruction of the surrounding structures free of artifacts.

The segmentation was carried out in projection domain because segmentation of a continuous metallic imprint would be more accurate than in spatial domain, where even small segmentation errors would have led to a wrong segmentation. The binary images from the segmentation step were used to replace the values of metallic regions in noisy sinograms with zero. This masked sinogram was padded and used as an input for the reconstruction step.

The chosen reconstruction method, the amMAP-EM, maximizes the likelihood of observing the measured projections subject to the prior knowledge. It uses Poisson model for the reconstruction data and median filter to implement local similarity prior. The result of each resolution stage initializes the next one. The binning factor is halved at the end of each resolution stage, automatically decreasing the penalization on the image. For different resolution stages, 10x10, 22x22, 44x44, 90x90, 180x180 and 362x362 images were chosen so that each image size would roughly double the previous one. The image sizes and their intensity ranges are rescaled between the stages. The reconstruction was stopped at a pre-defined normalized mean squared error value between the current and previous reconstruction for all image sizes. Image size was updated once the stopping criterion is reached within the same step. In the last stage, the original projection data is used. The stopping criterion for the iterations was chosen as 10^{-6} for both MLEM and amMAP-EM reconstructions in order to achieve comparable results from different numbers of iterations. The working principle of the algorithm is explained in Fig.1. [4]

In order to keep a clear boundary between metallic and anatomic regions, the segmented metallic regions were not replaced with interpolated values. However, for the FBP reconstruction, the metallic regions were left with their original values, as masking them out would have led to an incomplete dataset and wouldn't have represented the performance of the method accurately. FBP reconstruction was carried out with ramp filter and bicubic interpolation.

In evaluating the image quality quantitatively, firstly percentage normalized mean squared error (NMSE%) was calculated throughout the whole image. In this step, the ground truth image without metals was selected. The NMSE% values were calculated with respect to the ground truth image using the following formula

$$NMSE\%(I_{rec}, I_{gnd}) = \frac{\sum_{x=1}^M \sum_{y=1}^N [I_{rec}(x, y) - I_{gnd}(x, y)]^2}{\sum_{x=1}^M \sum_{y=1}^N [I_{gnd}(x, y)]^2} \times 100\% \quad (2)$$

,where I_{rec} is the reconstructed image and I_{gnd} is the ground truth. The green line in Fig.2 was used for line profile analysis so that it doesn't pass directly through the metallic regions but

it is at close proximity with a high density region, in which one would expect to see artifacts without MAR.

III. RESULTS

In Fig.2, the 256x256 reconstruction results from amMAP-EM, MLEM and FBP are presented. After FBP, the metallic values are saturated, and they cannot be distinguished from the surrounding teeth. MLEM fails to reduce the streak artifacts around the metallic region. amMAP-EM provides sharp edges at the metal/tooth boundaries for all cases presented. The surrounding teeth and tissue are reconstructed with no visible artifacts in almost all the reconstructions with amMAP-EM, except for the 8 metal-case, which presents minor bright and dark streak artifacts around the largest metals.

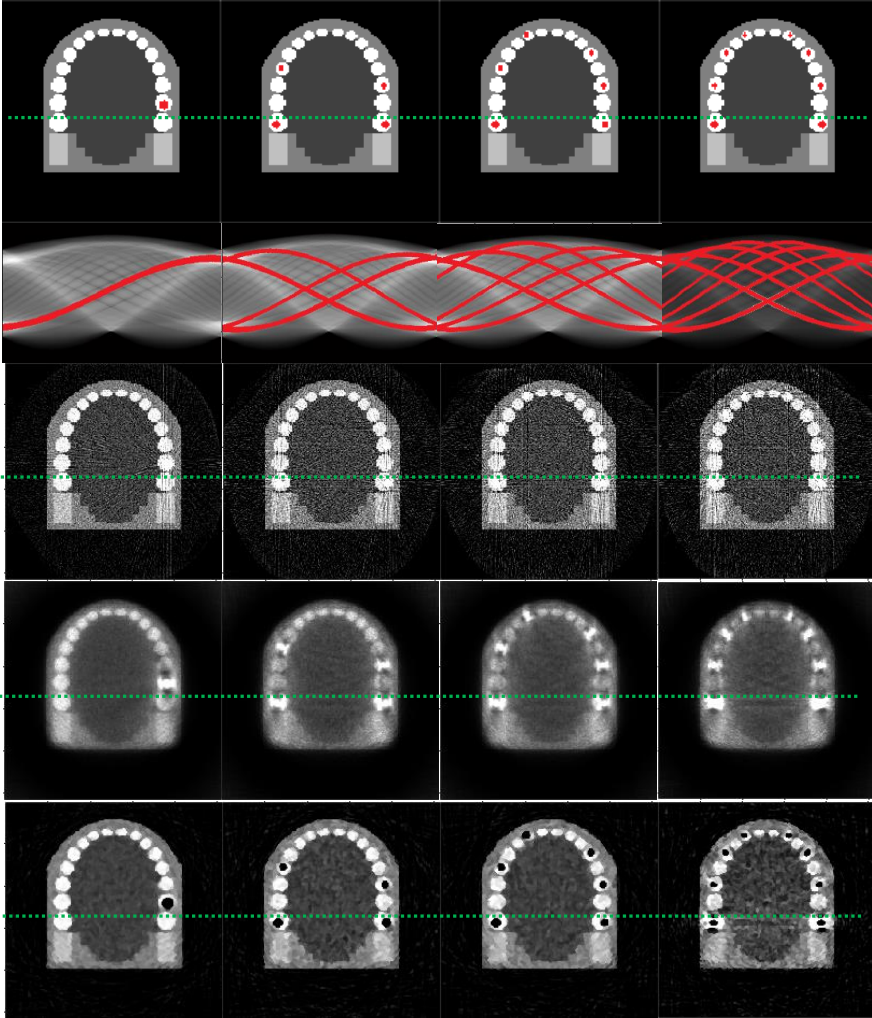


Fig. 2. Rows 1 and 2 represent the jaw phantom with metal implants and their corresponding sinograms contaminated with Gaussian noise. Metallic implant regions are overlaid with red on the images. These phantoms are used for investigating the effects of various sizes and placements of high density objects. Rows 3-5 correspond to the results for BP, MLEM and amMAP-EM reconstructions respectively.

The NMSE% values for the reconstructed images are presented in Table 1. Low levels of noise were achieved by amMAP-EM and MLEM compared to FBP, in which the NMSE% was much higher.

Table 1. NMSE% for MLEM, amMAP-EM and FBP calculated with respect to their respective ground truth images

	NMSE%		
	MLEM	amMAP-EM	FBP
1 metal	0.04	0.01	0.11
4 metals	0.03	0.02	0.21
6 metals	0.03	0.01	0.27
8 metals	0.08	0.05	0.32

The line profile analysis was carried out in order to examine the accuracy of the reconstructed values with respect to the ground truth. The results of the line profile analysis are depicted in Fig. 3. With amMAP-EM reconstruction, all cases, except the 8-metal case, all images showed the same sharp intensity changes as the ground truth at the boundaries.

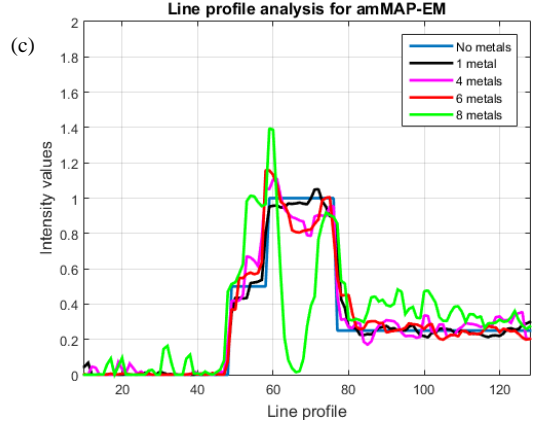
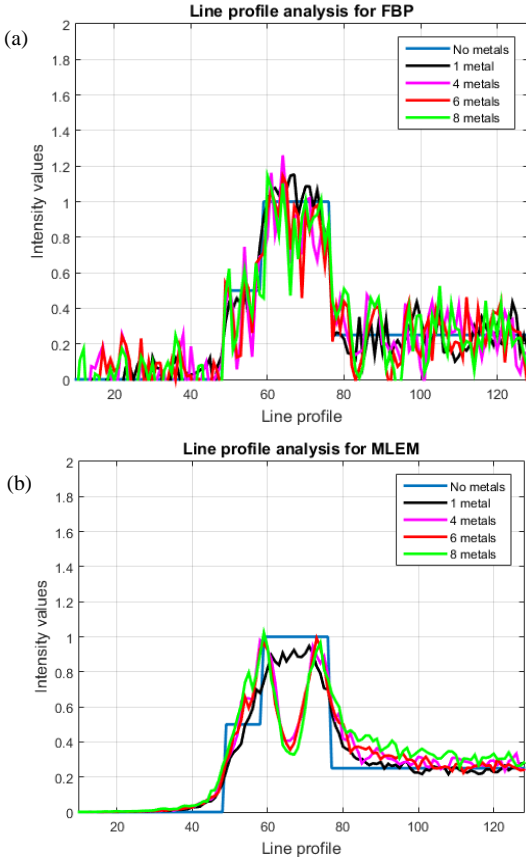


Fig. 3. Line profile analysis for 1, 4, 6 and 8 metal cases on the left half of the noisy numerical jaw phantom. Line profile for the ground truth image is depicted in blue. (a), (b) and (c) depict the results of FBP, MLEM and amMAP-EM reconstructions of the noisy jaw phantom for different amount of metals respectively.

In MLEM, 4, 6 and 8 metal cases failed to reconstruct the values of the enamel due to the generation of dark streak artifacts (See Fig. 3.b.). From the line profile of FBP, it can be seen that even though the boundaries are sharp, high noise in the reconstructed pixels makes it difficult to determine homogenous intensities for the anatomical regions.

IV. DISCUSSION AND CONCLUSION

For the reconstruction process, the focus was put on the reduction of the streak artifacts around the metals rather than replacing the values of metallic regions because the boundary detection and accurate determination of high density object sizes were considered more clinically relevant than the intensity values in the high attenuation regions. Although the input sinogram excluded the metallic regions from MLEM, the interpolated values gradually filled these gaps without regularization, causing dark and bright artifacts around the metal. In amMAP-EM, the metallic regions were not filled in accordance with the initial segmentation results. Streak artifacts were not very strong in FBP due to the chosen ratio of metal/teeth intensity, but this method doesn't allow visual determination of metallic regions. Higher metallic intensity values would immediately increase the streak artifacts in FBP.

As the amount missing data increases in the sinogram, both MLEM and amMAP-EM struggle with handling of limited data and the effect of noise robustness for each algorithm becomes less significant. This is why the NMSE% values of amMAP-EM and MLEM got closer at 8 metal-case, even though visual inspection shows fewer artifacts around the metals for amMAP-EM. Because of the noise amplification of ramp filter in FBP, its NMSE% was approximately 20 times higher than amMAP-EM, which can be seen from the large fluctuations in intensity in Fig. 3.c.

Line profile analysis showed that amMAP-EM results in intensity values closer to ground truth, compared to MLEM and FBP. The amMAP-EM also achieves sharper edges with low noise due to its high number of iterations at different iterations. These properties make the amMAP-EM a promising method for reconstruction when the metal size and shape is important, i.e.

after dental surgeries, in which the adaptation of the metal implant and the surroundings is important to follow.

In overall, the proposed MAR method, which combined a multi-level segmentation with amMAP-EM reconstruction, successfully reconstructed all metal/teeth boundaries in almost all cases. In order to decrease the computational load further, larger penalization steps can be chosen or iterations can be stopped earlier according to the application. For example changing the stopping criteria from 10^{-6} to 10^{-5} can decrease the required iterations by half.

REFERENCES

- Z. Tang, G. Hu and H. Zhang, "Efficient Metal Artifact Reduction Method Based on Improved Total Variation Regularization," *Journal of Medicine and Biological Engineering*, vol. 34, no. 3, pp. 261-268, 2013
- [1] U. Heil, D. Gross, R. Schulze, U. Schwanecke, and E. Schomer, "Metal artifact reduction in X-ray computed tomography: inpainting versus missing value," *Nuclear Science Symposium and Medical Imaging Conference (NSS/MIC), 2011 IEEE*, pp. 2675-2677, 2011.
- [2] J. Dong, Y. Hayakawa, S. Kannenberg, C. Kober, "Metal-induced streak artifact reduction using iterative reconstruction algorithms in x-ray computed tomography image of the dentoalveolar region," in *Oral and maxillofacial radiology*, vol. 115(2), pp. 63-73, 2013
- [3] E. Acar, S. Peltonen and U. Ruotsalainen, "Adaptive Multiresolution Methods for MAP reconstruction in Electron Tomography," *to be submitted*, 2015.
- [4] L. Paavola, E. Acar, U. Tuna, S. Peltonen, T. Moriya, P. Soonsawad, V. Marjomäki, R. H. Cheng and U. Ruotsalainen, "Compensation of Missing Wedge Effects with Sequential Statistical Reconstruction in Electron Tomography," *PLOS ONE*, vol. 9, no. 10, pp. 1-14, 3 October 2014.
- [5] U. Tuna, D. Us and U. Ruotsalainen, "Metal Artifact Reduction Based on Multi-Level Sinogram Segmentation and Sequentially Applied MAP-EM Reconstruction Method," in *Nuclear Science Symposium and Medical Imaging Conference (NSS/MIC)*, Seoul, 2013.
- [6] N. Otsu, "A threshold selection method from gray level histograms," *IEEE Transactions on Systems, Man and Cybernetics*, vol. 9, pp. 62-66, 1979.
- [7] H. Cai et.al, "A New Iterative Triclass Thresholding Technique in Image Segmentation," *IEEE Transactions on Image Processing*, vol. 23, no. 3, pp. 1038-1046, 2014.
- [8]

PUBLICATION IV

Evaluation of Median Root Prior for Robust In-beam PET Reconstruction

D. Us, K. Brzezinski, T. Buitenhuis, P. Dendooven, U. Ruotsalainen

IEEE Transactions on Radiation and Plasma Medical Sciences, vol. 2, no. 5, pp. 1--9, 2018

[10.1109/TRPMS.2018.2854231](https://doi.org/10.1109/TRPMS.2018.2854231)

Publication reprinted with the permission of the copyright holders.

© 2018 IEEE

Evaluation of median root prior for robust in-beam PET reconstruction

Defne Us, *Member, IEEE*, Karol Brzezinski, Tom Buitenhuis, Peter Dendooven, *Member, IEEE*, Ulla Ruotsalainen, *Member, IEEE*

Abstract—Dose delivery verification in proton beam radiotherapy is used to ensure the delivery of the dose to the correct location. A positron emission tomography (PET) scanner can be used to detect the secondary radiation during the treatment, so-called in-beam PET. This is a challenging application for PET due to the low counts and limited angular coverage. We propose a maximum a posteriori (MAP) reconstruction with median root prior (MRP) for the reconstruction of in-beam PET data. The proposed method was compared against MAP with total variation (TV) prior and maximum likelihood expectation maximization (MLEM), which have previously been used for this application. The effects of different ring configurations and time-of-flight (TOF) information were tested with simulations of a geometrical phantom and a realistic patient treatment plan. The results indicate that both MAP methods produced sharper edges than MLEM, allowing more accurate edge localization in the reconstructed images. Even for the partial ring configurations, no elongation was observed with MAP methods. MAP-MRP successfully reduced the noise, whereas MAP-TV resulted in checkerboard artifacts. MAP-MRP was also more stable against the selection of the reconstruction parameters. In conclusion, MAP-MRP offers a simple and robust alternative for the reconstruction of in-beam PET data.

Index Terms— Proton beam radiotherapy, particle beam radiotherapy, partial ring scanner, list-mode PET, time-of-flight (TOF)

I. INTRODUCTION

The beams used in particle beam radiotherapy have a well-defined, finite penetration depth with high dose deposition close to the end of the beam's trajectory, the so-called Bragg peak. This enables treatments in which less healthy tissue is irradiated as compared to irradiation with photons, leading to a reduction in irradiation-induced complications. However, as a result of the Bragg peak, large dose deposition errors can occur if the actual treatment situation is different from the situation assumed during treatment planning. An in-vivo technique to verify the dose delivery is thus essential to fully translate the superior dose deposition of particles into a clinical benefit.

In-vivo dose delivery verification by means of positron emission tomography (PET) created by the particle beam has a long history (see [1]–[3] for some recent reviews) and is in routine use in a few particle therapy centers [4], [5]. The most abundantly produced positron emitters are ^{15}O ($T_{1/2} = 2.0$ min), ^{11}C ($T_{1/2} = 20.0$ min), ^{30}P ($T_{1/2} = 2.5$ min) and ^{38}K ($T_{1/2} = 7.6$ min). Unfortunately, radioactive decay process delays the

information from PET, preventing real-time feedback on the dose delivery. Recent work on the production of very short-lived positron emitters may pave the way to real-time dose delivery information using PET [6], [7].

In-beam PET for in-vivo dose delivery verification is a challenging application for PET for two reasons. The first is the low statistics compared to conventional PET studies. At the end of a proton therapy irradiation, the PET activity is typically of the order of 1 kBq/cm^3 , resulting in a small number of counts; a total of 0.04 M to 0.37 M counts were measured with a limited angle tomograph and a PET acquisition time of 200 s [8]. Such positron emitter activity and number of PET counts are much lower than those typical for diagnostic PET ($10\text{--}100 \text{ kBq/cm}^3$ and $100\text{--}1000 \text{ M}$ counts) and can cause the reconstructed images to very quickly converge to the noise instead of the object's true shape. Secondly, to allow the therapeutic beam to reach the patient unobstructed, generally scanners with limited angular coverage are used [4], [8]–[10]. A notable exception is OpenPET, in which the second generation design with slanted rings allows the beam to pass unobstructed while providing full angular coverage [11]. Partial ring scanner configurations are known to result in elongation artifacts in the direction of the detectors, hindering the accurate estimation of the edges around the irradiated volume [12]. As the accurate determination of the edges is the most important metric for in-vivo dose delivery verification, potential artifacts motivate an application-specific reconstruction method for in-beam PET, which reconstructs sharp edges while reducing the overall noise in the image. The use of time-of-flight (TOF) PET reduces image noise and can mitigate limited angle artifacts, but the degree of improvement by using TOF information depends on the selected reconstruction method [13].

Maximum likelihood expectation maximization (MLEM) with and without subsets has previously been used in reconstruction of PET images acquired during particle therapy [12], [14]–[16]. As the inversion problem is ill-posed in emission tomography, MLEM-like methods can result in the amplification of noise over the iterations, especially with low statistics data. This can be remedied by early stopping or post-smoothing, but the former can result in images that are too close to the given prior image and the latter causes blurring at the edges of the image. Maximum a posteriori (MAP) methods use an additional weighted penalty term in the reconstruction to prevent the amplification of noise. Any knowledge on the nature of the data, which is called a prior, can be incorporated into the MAP reconstruction. The features of the image that

deviate from the prior are penalized in the reconstruction. The selected prior needs to reflect the assumptions on the data. The emission data are assumed to be locally uniform (so-called monotonicity), meaning that the pixel values of the image are approximately constant in a local neighborhood. Thus, any prior for imaging of biological structures with PET needs to allow local smoothness while preserving the edges. The total variation (TV) prior is one such prior [17]. It has earlier been suggested for particle therapy applications [13], [18], [19]. Once optimized, MAP reconstruction with TV prior (MAP-TV) outperforms MLEM. Although no artificial jumps are introduced with MAP-TV, the extremely low counts of in-beam PET data can disrupt the assumption of monotonicity and cause checkerboard artifacts [17].

In this paper, we penalize the noise using the median root prior (MRP) to accommodate the fluctuations in the data, while reducing the noise and preserving the edges [20]. MRP has previously been used for the reconstruction of Poisson-distributed data [21]–[23]. Its ability to accommodate missing detector information was demonstrated in [24]. The penalty term with MRP has not been implemented for the reconstruction of in-beam proton therapy data so far and it is proposed here because of its robustness against missing detectors and the stability of its penalty weight.

We aim to compare the performance of MAP-MRP with MLEM and MAP-TV and to determine the effects of TOF and partial ring configurations on these reconstruction methods.

II. IMAGE RECONSTRUCTION

A. 3D list-mode MAP-EM

In list-mode (LM) reconstruction, events can be processed individually due to the independent nature of forward and backward projection of each line of response (LOR). This allows multiple LORs to be processed in parallel using 3-dimensional (3D) subsets, thus speeding up the reconstruction significantly. In LM reconstruction, no pre-processing is applied, so the data statistics are preserved [25]. Without rebinning, TOF information can be fully exploited to improve the reconstruction of the LORs. In this work, the counts were divided into L subsets ($l = 1, 2, \dots, L$), with each subset containing h LORs. The current image estimate $x_j^{(k)}$ is updated by all L subsets and these update images are summed together to form a correction image. The system matrix calculations for each subset was distributed to multiple nodes via Techila Distributed Computing Engine¹ with MATLAB (MathWorks Inc., MA, USA). An outer-iteration consists of one pass of the current image estimate through L subsets [26]. This subset approach was proposed in [27] and also used in [26], and is referred to as LM-EM-ML due to its convergence to an ML estimate. The posterior estimate of the image with list-mode MAP-EM reconstruction using the one-step-late (OSL) scheme can then be written as

$$x_j^{(k+1)} = \frac{x_j^{(k)}}{\sum_{i=1}^I A_{ij} + \beta \frac{\partial}{\partial x_j} U(x)|_{x_j=x_j^{(k)}}} \sum_{l=1}^L \sum_{h \in S_l} A_{i,h,j} \frac{1}{\sum_{j=1}^J A_{i,h,j} x_j^{(k,l)}} \quad (1)$$

, where $x_j^{(k)}$ is the reconstructed value of the j^{th} voxel in the image at the k^{th} iteration, J is the total number of voxels to be reconstructed and I is the total number of LORs. A_{ij} is the system response matrix, and it denotes the probability of activity in the

j^{th} voxel being detected in the i^{th} LOR. The term $\sum_{i=1}^I A_{ij}$ is the

sensitivity matrix. $U(x)$ is the energy function whose derivative with respect to the current image at iteration k is the penalty function. $U(x)$ determines the degree of smoothing over the voxels. The hyperparameter β determines the weight of the local regularization term. β values were chosen within the range of $[0,1]$ because the positivity constraint of the image values is guaranteed only if the hyperparameter value does not exceed the maximum of the normalized values in the sensitivity image. A large β increases the strength of the regularization. When $\beta=0$, the MAP-EM becomes MLEM. The penalization is applied onto the $x_j^{(k)}$ once iterations of all L subsets within one outer iteration are completed, which prevents any instability due to the very low count statistics within each subset.

1) Median root prior (MRP)

In MRP, the noise penalization is based on the median of the pixel values within a certain neighborhood. Its name comes from the root signal of the median filter, which passes the median filter unchanged [20]. The reconstruction algorithm with MRP assumes local monotonicity of the spatial image and it penalizes any deviation from the median in the neighborhood [28]. This enables the algorithm to preserve the edges of the image, allowing abrupt changes as well as smooth ones. The non-monotonic features smaller than a given limit are considered as noise and are filtered out. The size of the minimum details preserved in the image depend largely on the weight of the penalization (β value) and the window size of the median filter [21]. Note that the MRP penalty term is data-driven, where the value of the median around the j^{th} pixel, M_j , is directly calculated from the data. Therefore, the calculation of the exact derivative of the energy function $U(x)$ in (1) is not possible for MRP. Instead, the difference image between the image from the previous iteration $x_j^{(k)}$ and $M_j = \text{Med}(x^{(k)}; j)$ is used. With these changes, the penalty term in (1) is calculated

as $\frac{x_j^{(k)} - M_j}{M_j}$ [29].

2) Total variation (TV)

The TV prior uses the norm of the image gradient as a criterion for penalization. The gradient of the image results in high values at the object boundaries, where the intensity values can be discontinuous. The TV allows these sharp changes in the image [17]. This is an important property for preservation of the edges during image reconstruction. The elongation of the object in partial ring scanners can also be mitigated via TV prior [13]. The global calculation of the TV norm ensures the smoothness of monotonic regions and reduces the noise. The derivative of the energy function for TV penalty consists of partial

¹ <http://www.techilatechnologies.com/>

derivatives of the image estimate. In this study, the l1 norm was used for the calculation of the TV penalty term. The TV norm of an image A in x , y and z dimensions is calculated by

$$U(A)_{TV} = \sum_{x,y,z} u(x,y,z) \\ = \sum_{x,y,z} \sqrt{(A_{x+1,y,z} - A_{x,y,z})^2 + (A_{x,y+1,z} - A_{x,y,z})^2 + (A_{x,y,z+1} - A_{x,y,z})^2} + \varepsilon \quad (2)$$

, where ε is a small parameter that prevents division by zero and ensures differentiability [17]. The penalty term in (1) is then replaced with

$$\frac{\partial U(A)}{\partial A_{x,y,z}} = \frac{A_{x,y,z} - A_{x-1,y,z}}{u(x-1,y,z)} + \frac{A_{x,y,z} - A_{x,y-1,z}}{u(x,y-1,z)} \\ + \frac{A_{x,y,z} - A_{x,y,z-1}}{u(x,y,z-1)} - \frac{A_{x+1,y,z} + A_{x,y+1,z} + A_{x,y,z+1} - 3A_{x,y,z}}{u(x,y,z)}. \quad (3)$$

3) Implementation

The reconstructions were performed in MATLAB® 2017b with Intel X5660 processors in the Merope and Techila computing clusters of Tampere University of Technology. Monte Carlo simulations for proton therapy were conducted via Geant4 Simulation toolkit [30]. Gate (Geant4 Application in Tomographic Reconstruction, version 7.2, [31]), which is designed for nuclear medicine applications, was used for the simulation of PET system. The components of the object-related A_{ij} were calculated using Siddon's ray tracing algorithm [32]. No normalization or attenuation correction were applied before the image reconstruction in order not to change the Poisson characteristics of the data.

For the geometrical phantom, the sensitivity matrix for the scanner was computed with a separate Gate simulation, in which the field of view of the scanner was defined as vacuum with no object inside the scanner. The detector responses were recorded for a sufficiently large number of events. For the realistic phantom data, the sensitivity was computed analytically by backprojection of one count per LOR. An exact attenuation map was constructed and each LOR in A_{ij} was weighted on-the-fly with its corresponding attenuation correction factor during backprojection. Scatter and randoms corrections were not included in the reconstructions. Scattered events were removed from the data and randoms rate was small enough (~6% of total counts detected) for the correction to be excluded.

For the reconstruction of the geometrical phantom, 4 mm × 4 mm × 4 mm voxel size was used, resulting in image size of 81 × 81 × 45 in x , y and z dimensions. The reconstructed image size for the realistic patient phantom was 125 × 88 × 110 voxels in x , y and z dimensions. The window size for the median filter used in MAP-MRP was selected as [3 3 3] voxels. The reconstructed image was initialized as an array of ones for all reconstruction methods. For the reconstruction, subsets with 8000 counts were used ($h = 8000$). 100 outer iterations were performed on the full data to investigate the convergence of the reconstructions. β values within the range of [0.01, 0.8] were tested. The hyperparameter values and the stopping criterion for the iterations were calculated for the geometrical phantom and

later tested and used for the reconstruction of the realistic patient treatment plan.

The LOR endpoints were chosen to be at a depth of 8 mm in the crystal and in the center of the crystal cross section. Coincidence resolving times (CRT) of 400 ps and 200 ps full-width-half-maximum (FWHM) were selected because 400 ps is currently available in clinical use and the 200 ps has been obtained in small-scale setups and is thus a realistic value for a future generation of scanners [13], [33], [34]. For the reconstruction with different CRTs, the exact TOF information was convolved with a Gaussian function, with a FWHM is equal to the CRT of the system. For the partial ring configurations, the detectors were removed symmetrically from either side of the scanner. The effect of angular coverage on the reconstruction methods was studied for full ring (360 degrees), 2/3 ring (240 degrees) and 1/2 ring (180 degrees) configurations, similar to the setting in [16].

III. SIMULATIONS

1) Geometrical phantom simulation

The geometrical phantom was used to evaluate the performance of the reconstruction methods with low count statistics and limited angular coverage. The effect of TOF information on the reconstruction was also studied. Activity densities in the range of few kBq/cm³ were used. No proton beam was simulated for this phantom. The full-ring PET scanner configuration in the simulation contained 36 detector heads distributed in a ring of diameter 825 mm with an axial FOV of 180 mm. The 4 × 4 × 22 mm³ LSO scintillator crystals were set in an 18 × 45 array for each detector head. The energy resolution was 13% at 511 keV, with lower and higher energy thresholds of 350 keV and 650 keV respectively. The coincidence time window was set to 4.5 ns. Only ¹⁵O production was simulated due to its high activity rate in the beginning of the proton treatment. A 60 second PET measurement with a total activity of 4.06 MBq was simulated. Fig. 1.a. shows the full and partial ring scanner configurations for the geometrical phantom.

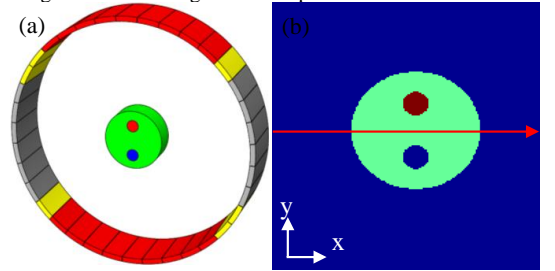


Fig. 1. (a) Scanner configurations for the PET simulation of the geometrical phantom. Gray detector heads are used in the half ring configuration (180 degrees coverage), whereas the gray + yellow blocks indicate the detector heads used for the 2/3 ring (240 degrees coverage). (b) Transverse view of the geometrical phantom. The red solid line in (b) was used to calculate the line profiles.

The 12 cm-long cylindrical polyethylene nonvoxelized phantom (green circle in Fig. 1.b) with 10 cm radius can be seen in Fig. 1.b. The hot cylinder in the phantom (red circle in Fig. 1.b) contains radioactive water with 4 times higher activity

than the background (4 kBq/cm^3 : 1 kBq/cm^3). The cold cylinder (blue circle in Fig. 1.b) was filled with air without activity.

The list of coincidences was recorded with perfect time resolution from the simulation, containing the exact detector coordinates and the TOF information. 300 K true counts were gathered and used to construct the LM input for the reconstructions. For the 2/3 and 1/2 ring configurations, 180 K and 130 K true counts were gathered respectively.

2) Realistic phantom simulation

For a more realistic phantom study, a proton therapy treatment plan of a patient was simulated using Geant4. The patient CT and treatment plan were obtained from the Department of Radiotherapy of the University Medical Centre in Groningen. The production of ^{10}C , ^{11}C , ^{13}N , ^{14}O , ^{15}O , ^{30}P and ^{38}K nuclides during irradiation was simulated. The distribution and decay of these isotopes were included in the Gate simulations of the PET scans. The emission map in Fig. 2.a, representing the distribution of positron emitter decay integrated over the duration of the scan, was used as reference for the evaluation of the reconstructed images. Three proton fields were delivered to the patient, with proton beam angles of +40, 0 and -40 degrees with respect to the y axis. The 3rd irradiation field is shown in Fig. 2.b, as most of the positron annihilations detected by the scanner comes from positron emitters produced during the last field. Biological washout of the PET nuclides was implemented following the procedure of Helmbrecht *et al.*, using one washout component with a half-life of 69 s and a fraction of 0.44 [35]. A 120 second scan was simulated with 60 seconds delay after the delivery of the last field. The PET scanner used in this simulation was based on the Siemens Biograph64 PET/CT with TrueV option (Siemens Molecular Imaging, Knoxville, USA). The energy resolution was set to 13% at 511 keV, with lower and higher energy thresholds of 350 keV and 650 keV respectively. The coincidence time window was set to 4.5 ns. The attenuation map was obtained from the bilinear scaling of the HU values in the CT scan of the patient [36]. The total activity was 5.9 MBq (1 kBq/cm^3) 60 s after the delivery of the last field. The dose delivered at the target area was about 2 Gy in total (similar to the dose delivered in [18]), a typical value for a daily fraction of the irradiation treatment. The full ring scanner simulation included 4.28 M true counts. The 2/3 and 1/2 ring configurations resulted in 3.25 M and 2.35 M true counts respectively.

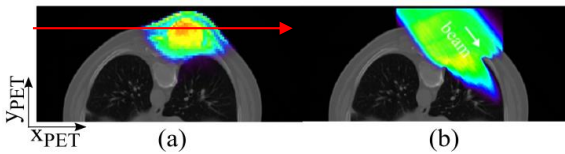


Fig. 2. (a) The realistic patient phantom with emission map overlaid on the CT image. The red arrow was used to calculate the line profiles. (b) The dose map of the 3rd irradiation field overlaid on the CT image.

B. Assessment criteria

The normalized mutual information (NMI) measures the similarity of information between two images, giving the value of 1 if two images are identical [13]. It was used to select the optimal weight of the penalization (β) for TV and MRP as well as the stopping criteria for the MAP methods [13]. The standard

deviation across 2D slices was also calculated as a measure of uncertainty. The NMI is calculated through the Shannon entropy of the images. The Shannon entropy of an image (H) is defined as

$$H = - \sum_i p(i) \log p(i) \quad (4)$$

, where the probability $p(i)$ that the value of the i^{th} voxel occurs is calculated from the histogram of the image. Let the respective entropies of two images A and B be $H(A)$ and $H(B)$. $H(A,B)$ represents the entropy of the joint histogram of two images. The mutual information between A and B , $MI(A, B)$, is then

$$MI(A, B) = H(A) + H(B) - H(A, B) \quad (5)$$

Using $MI(A, B)$, the NMI is calculated as follows:

$$NMI(A, B) = \frac{MI(A, B)}{\sqrt{H(A)H(B)}} \quad (6)$$

Bias between the reconstructed images and the ground truth was used to evaluate the reconstruction accuracy. The bias between the reconstructed image A and the reference image B is calculated as

$$\text{Bias} = \frac{\text{mean}(A) - \text{mean}(B)}{\text{mean}(B)} \times 100 \quad (7)$$

The coefficient of variation (CoV) was used to evaluate the level of noise reduction in the reconstructed images. Each CoV was calculated within a volume of interest (VOI) using

$$\text{CoV} = \frac{\sigma_{\text{VOI}}}{\mu_{\text{VOI}}} \quad (8)$$

, where σ_{VOI} is the standard deviation of the voxels within a VOI, and μ_{VOI} is the mean value of these voxels. A low CoV indicates low noise in the image, whereas a high CoV is a sign of high noise within the VOI.

Sigmoid functions were fitted to the edges of the reconstructed images to calculate and compare their accuracy in determining the edges. The following sigmoid function $\text{sig}(h)$ was used in this work:

$$\text{sig}(h) = \text{base} + \frac{\max}{1 + \exp\left(\frac{h_0 - h}{b}\right)} \quad (9)$$

, where h is the pixel index along the line profile. The “base” is set to zero as there is no activity outside of the phantom. h_0 is the position at which 50% of the $(\max - \text{base})$ value is reached. b is a measure for the steepness of the edge. A smaller b shows a steeper edge and a more accurate determination of the distal edge.

Iso-contour comparison was used for the evaluation of the realistic phantom reconstructions. As the iso-contours are used for dose calculations in clinical practice, they were preferred over the reconstructed images for visual comparison of the realistic phantom images.

IV. RESULTS

A. Results of the geometrical phantom

Before the comparison of reconstruction methods, the optimal penalization weight and number of iterations for the MAP reconstructions were determined. In MAP reconstruction, β determines the strength of penalization. The hyperparameter that maximizes the 3D NMI and stabilizes over iterations was selected as optimal for each prior. Fig. 3 shows the NMI values for several β over 100 iterations for 2/3 ring scanner with 400 ps CRT. The trend of the NMI values obtained from reconstructions with other partial ring configurations and CRT values show a similar pattern.

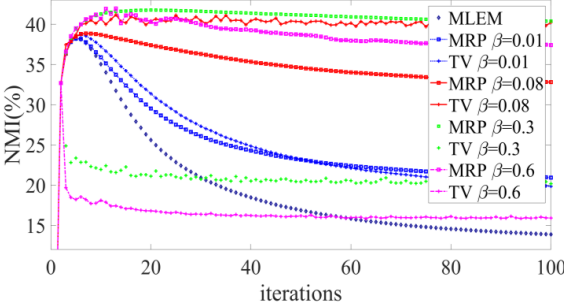


Fig. 3. NMI (%) values for selected β values over 100 iterations. NMI values were calculated over the 3D image volume from the 2/3 ring scanner with 400 ps CRT.

It can be seen from Fig. 3 that a stable maximum NMI is achieved at $\beta = 0.3$ for MRP and $\beta = 0.08$ for TV. For TV, the NMI values rapidly decrease when β is greater than 0.08. The MRP results become stable at $\beta = 0.3$ and, for higher values, image blurring as well as the distortion of the first and last slices in the axial (z) dimension, due to 3D filtering, cause the NMI to decrease over iterations. In the selection of number of iterations, the dominant concern was the stability of the reconstructions, therefore a high number of iterations were selected for MAP methods. It was observed that the NMI values of MAP reconstructions for the selected β values stabilize after 50 iterations (Fig. 3). All MAP reconstructions evaluated from hereon were thus obtained after 50 iterations. As NMI values of MLEM decrease over iterations, 7 iterations were used.

Fig. 4 shows the reconstructed images from the geometrical phantom for both CRT values and all scanner configurations. The summed slices are shown here similar to [37]. The effect of the missing detectors in the partial ring scanners is clearly visible for images reconstructed via MLEM with 400 ps CRT, resulting in the elongation along the direction of the detectors. These effects are reduced by the improved TOF information. Both MAP reconstructions have clear boundaries and less elongation. As the overall reconstruction is already better for MAP methods than MLEM, the effect of improved TOF is less pronounced on MAP than MLEM reconstructions.

Table I gives the mean of bias and CoV as well as the sigmoid fit parameters for the reconstructions. The uncertainty reported

here is the standard deviation across different slices. Bias and CoV values were calculated through the uniform volume in the background cylinder, excluding the areas near the hot and cold volumes to avoid spilling of activity from the high activity regions in case of elongation.

TABLE I

BIAS, CoV AND SIGMOID FIT PARAMETERS FOR THE GEOMETRICAL PHANTOM (TRUE h_0 IS AT PIXEL 65.53, $b=0$)

	Full ring 400ps	Full ring 200ps	2/3 ring 400ps	2/3 ring 200ps	1/2 ring 400ps	1/2 ring 200ps
Bias (%)						
MLEM	-52.5 ± 1.2	-50 ± 1.2	-42.9 ± 1.4	-43.9 ± 1.8	-41.2 ± 5.5	-45.5 ± 3.8
MAP-MRP	-28.6 ± 1.6	-29.6 ± 1.4	-31.2 ± 0.8	-32.2 ± 1.1	-31.6 ± 3.3	-34 ± 3.1
MAP-TV	-28.3 ± 2.1	-31.1 ± 1.8	-32 ± 2.3	-33.2 ± 2	-33.2 ± 7.7	-35.6 ± 5.3
CoV (%)						
MLEM	63.3 ± 7.5	66 ± 7.3	60 ± 5.8	65.7 ± 6.1	64.9 ± 5.9	70 ± 6.5
MAP-MRP	38.6 ± 1.2	38.6 ± 1.2	45.5 ± 1.04	43.8 ± 1.03	52.9 ± 1.9	50.2 ± 1.7
MAP-TV	42.6 ± 6.4	40.6 ± 5.5	46.9 ± 6.5	44.5 ± 5	52.3 ± 5.6	50.5 ± 3.8
h_0						
MLEM	65.5 ± 0.44	65.5 ± 0.46	63.1 ± 0.78	63.4 ± 0.75	63.4 ± 0.75	63.5 ± 0.52
MAP-MRP	65.1 ± 0.16	65.2 ± 0.14	63.2 ± 0.41	64 ± 0.32	62.5 ± 0.41	63.6 ± 0.35
MAP-TV	65.3 ± 0.13	66 ± 0.10	63.2 ± 0.33	64 ± 0.38	63 ± 0.32	64 ± 0.30
b						
MLEM	-0.6 ± 0.37	-0.4 ± 0.36	-2 ± 0.66	-1.2 ± 0.65	-2 ± 0.63	-0.6 ± 0.45
MAP-MRP	-0.3 ± 0.29	-0.3 ± 0.17	-0.9 ± 0.36	-0.9 ± 0.28	-0.5 ± 0.34	-0.4 ± 0.26
MAP-TV	-0.4 ± 0.1	-0.1 ± 0.01	-1.2 ± 0.29	-1.1 ± 0.33	-0.6 ± 0.28	-0.6 ± 0.27

The MAP-MRP reconstructions achieved the best bias and CoV for most of the studied cases, as well as smallest standard deviation across slices. The MAP-TV performs slightly worse than the MAP-MRP for partial rings, but its CoV and bias are still significantly lower than those of MLEM. Better TOF slightly improves the contrast recovery and the fitting of the sigmoid function of MAP methods, particularly in partial ring configurations. Both bias and CoV indicates worse performance for MLEM for 200 ps compared to 400ps.

The accuracy of the reconstructed edges was evaluated by fitting sigmoid functions to the line profiles (see Table I). The sigmoid fit was calculated from the average of the central slice and its two closest neighbors in the axial direction. As the falling edge was used in the calculation of the fit, the slope (b) is negative. When comparing the accuracy of the sigmoid fits, the edge of the ground truth was taken as reference, with h_0 at 65.53 and $b=0$.

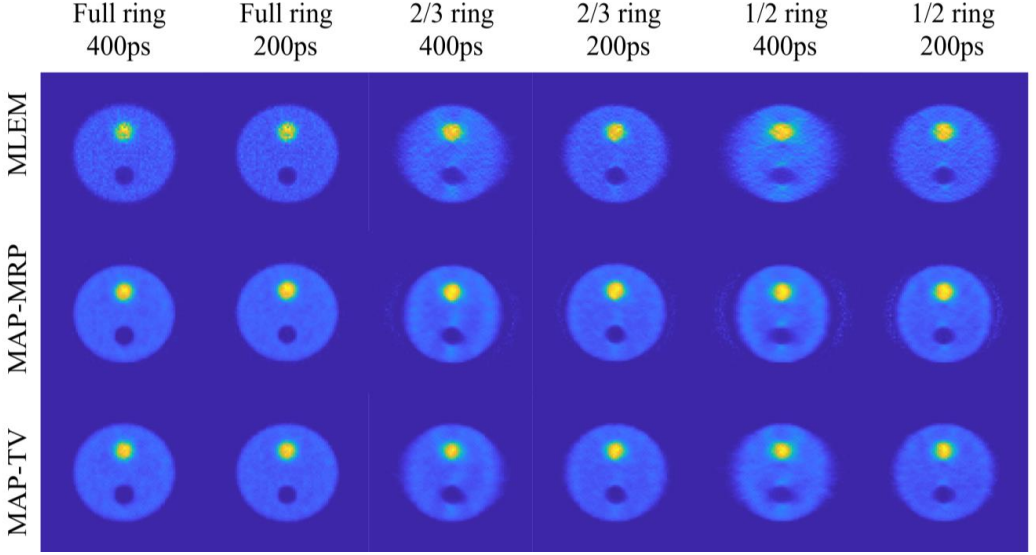


Fig. 4. Reconstructed images from sum of transverse slices. The intensities in each image are normalized within the range of [0,1] after the extreme values are excluded from the image. Rows 1, 2 and 3 depict the MLEM, MAP-MRP and MAP-TV reconstructions respectively. MLEM images were stopped after 7 iterations. The MRP and TV prior reconstructions are presented here with their optimal β values after 50 iterations ($\beta = 0.3$ for MRP and $\beta = 0.08$ for TV). The elongation along the x direction is visible for the partial ring reconstructions for MAP-TV and MLEM.

All sigmoid fits for the full ring configuration indicate high accuracy of results, though the uncertainties on the fit parameters are smaller for MAP. For the partial ring configurations, the MAP methods demonstrated a sharper edge than MLEM for both CRT values. All partial ring reconstructions showed improvement with 200 ps CRT.

B. Results of the realistic patient phantom

Before the evaluation of the reconstructed images, the reconstruction parameters were tested for the realistic patient phantom. According to the NMI values for various β in Fig. 5, optimal β was selected as 0.02 for TV. β was 0.3 for MRP.

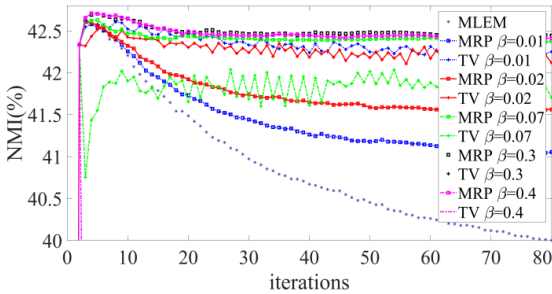


Fig. 5. NMI values for the studied β values for the realistic phantom from the 2/3 ring scanner with 400 ps CRT. NMI values were calculated over the whole image volume.

In proton therapy, the iso-contours are commonly used to evaluate the treatment plan. In this study, they were used as indications of the relative intensities for each reconstructed image to make the differences between the images more visible. The iso-contours of the emission map overlaid on the CT image and the reconstructed images can be seen in Fig. 6. The iso-contours from the MAP reconstructions follow the shape of the contours in the emission activity well, with MRP resulting in better reconstructions of the irregular contours (see the white arrow in Fig. 6. Also, the contours of the high intensity regions (80% of the maximum activity marked in red in Fig. 6) in MAP-MRP reconstructions are visually more similar to the emission map than MLEM and MAP-TV. The MAP-TV reconstructions have poorer performance with low statistics data and they do not recover uniform high intensity areas. This is visible from the red iso-contour areas in Fig. 6 (marking 80% of the maximum activity respectively).

Table II shows the bias and CoV values as well as the sigmoid fit parameters for the reconstructions of the realistic phantom. The bias values were calculated using the normalized reconstructions and emission map. Iso-contour lines were used to create a homogenous VOI for the calculation of the bias and CoV values of the realistic phantom. The red iso-contour line at the center of the emission image (80% of the maximum value within the slice) was used as a threshold to obtain an approximately homogenous volume. The CoV value for the same volume in the emission image was 5.16%.

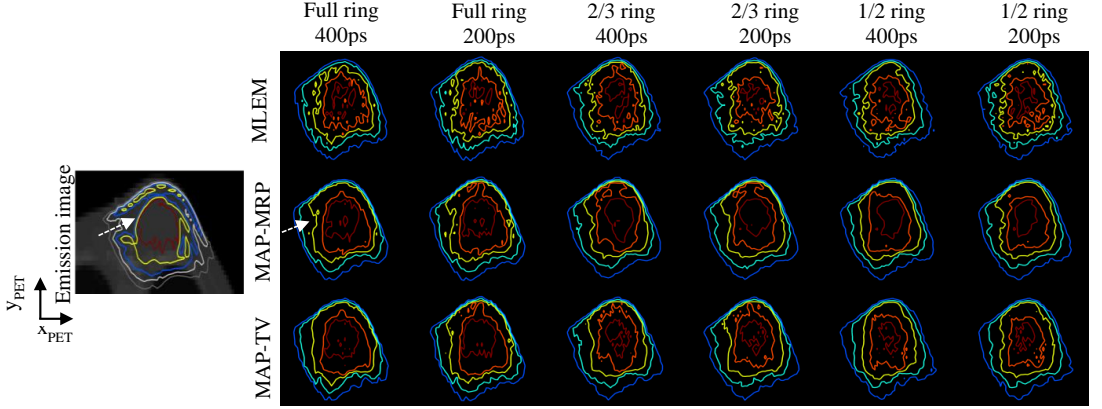


Fig. 6. Transverse view of the reconstructions from the realistic phantom with iso-contours. 50 iterations were used for MAP-MRP and MAP-TV reconstructions ($\beta = 0.3$ for MRP and $\beta = 0.02$ for TV). MLEM reconstructions were stopped after 7 iterations.

The bias and CoV of the partial ring reconstructions were the best for MAP-MRP. The improvement of CRT did not improve the CoV or the bias of MLEM for the partial rings, but the standard deviation was lower with better TOF.

TABLE II

BIAS, CoV VALUES AND SIGMOID FIT PARAMETERS FOR THE REALISTIC PHANTOM. (TRUE h_0 IS AT PIXEL 53.41, $b=0$)

	Full ring 400ps	Full ring 200ps	2/3 ring 400ps	2/3 ring 200ps	1/2 ring 400ps	1/2 ring 200ps
Bias (%)						
MLEM	-16.5 ± 5.3	-17.6 ± 4.8	-19.5 ± 6.9	-21.5 ± 6.9	-22 ± 6.3	-22.1 ± 7.1
MAP-MRP	-6.7 ± 2.6	-6.9 ± 2.7	-8.3 ± 4.8	-9.3 ± 4.5	-10.2 ± 5.7	-9.9 ± 4.8
MAP-TV	-8.64 ± 4.5	8.03 ± 4.02	-14.63 ± 5.3	-14.13 ± 4.4	-15.81 ± 5.7	-14.94 ± 4.4
CoV (%)						
MLEM	12.4 ± 1.9	12.7 ± 1.8	14.9 ± 3.2	15.2 ± 3	15.9 ± 3.2	16.2 ± 3.3
MAP-MRP	9 ± 1.3	8.8 ± 1.3	11.1 ± 3.4	10.97 ± 3	11.7 ± 3	11.4 ± 2.8
MAP-TV	9.22 ± 1.9	9 ± 1.6	13.2 ± 2.9	12.5 ± 2.5	13.2 ± 3.1	12.5 ± 2.9
h_0						
MLEM	54.18 ± 0.09	53.86 ± 0.06	54.24 ± 0.09	53.76 ± 0.06	54.82 ± 0.18	54.08 ± 0.09
MAP-MRP	53.25 ± 0.04	53.30 ± 0.05	53.18 ± 0.1	53.33 ± 0.06	53.01 ± 0.07	53.57 ± 0.09
MAP-TV	53.24 ± 0.05	53.31 ± 0.04	53.21 ± 0.09	53.40 ± 0.07	53.79 ± 0.17	53.67 ± 0.09
b						
MLEM	2.02 ± 0.07	1.63 ± 0.05	2.08 ± 0.06	1.42 ± 0.05	2.73 ± 0.12	1.73 ± 0.07
MAP-MRP	1.13 ± 0.04	1.04 ± 0.04	1.14 ± 0.08	1.15 ± 0.05	1.13 ± 0.07	1.27 ± 0.08
MAP-TV	1.03 ± 0.04	1.02 ± 0.04	1.24 ± 0.08	1.20 ± 0.06	1.81 ± 0.14	1.38 ± 0.08

For the evaluation of the accuracy of reconstructed edges, sigmoid functions were fitted to averaged line profiles from the central slice and its two closest neighbors (along the red line in

Fig. 2). The line profile was not calculated along the proton beam directions (which one needs to do to verify the proton range) because the edge in the PET image shows the edge of the lung in cases where the proton beam is stopped beyond this edge, and not the proton range. The sigmoid fit parameters for the MAP reconstructions are similar, with MRP being slightly better for partial ring configurations. TOF is effective in making the slopes of MLEM fits steeper (smaller b), but its effect on MAP results were minimal.

V. DISCUSSION

In this study, MAP-MRP successfully improved the edge detection and image uniformity via the use of MRP for penalization in MAP reconstruction. The proposed penalty function was robust against the change in partial ring scanner configurations with low count statistics. The observations based on our results are in line with the results from Cabello *et al.* [13], which used the TV prior information for MAP-EM on pencil beam data for hadron therapy. In general, both MAP methods are robust against missing information due to the partial ring scanner configuration. MLEM, on the other hand, cannot compensate for the large gaps in the angular coverage without any regularization or very good TOF information.

The results from [13] indicate that if the MAP penalization parameter for TV is not selected carefully, the algorithm may not lead to a stable solution. This finding was also noted in the work of Teng *et al.*, in which they compared the performances of MLEM with MAP with TV prior on simulated and clinical data [38]. In our work, MAP-MRP was much less sensitive to the choice of the regularization parameter (see Fig. 3 and Fig. 5) than MAP-TV. This was due to the use of a median filter in MRP, which preserves the intensity changes between different structures, while smoothing the intensity changes within the filter window. Stability of MRP against noise makes it possible to have strong penalization without introducing additional artifacts in the reconstructed images. The CoV and bias values are similar for the MAP methods, but a difference between MAP and MLEM reconstructions is visible.

The voxel size of $4 \times 4 \times 4 \text{ mm}^3$ was selected due to the high noise in the data. A smaller voxel size of $2 \times 2 \times 2 \text{ mm}^3$ was

tested, and the line profiles were found too noisy to determine a reliable edge. For higher statistics, as was the case in [16] with coincidence counts from 15 M to 150 M, smaller voxel sizes could be used. But such statistics are not realistic in the proton therapy application considered here.

Previous studies have shown that TOF information generally improves the contrast recovery, increases the convergence speed and is less sensitive to noise and inconsistent data corrections [13], [16], [39]. Both MAP methods prevented the elongation and suppressed the noise efficiently. Therefore, the improvement of TOF did not result in a significant improvement for the images reconstructed with MAP methods. About 400 ps CRT was deemed sufficient to obtain sharp edges with the penalized MAP reconstruction methods. On the other hand, TOF information around 200 ps or better is needed with MLEM to achieve similar results as MAP reconstructions.

The MAP methods used in this work reliably reconstructed clearer edges than MLEM, separating the object from the background. They were also better at reconstructing the images in the presence of missing angles. In addition to the shared advantages of MAP methods, the MAP-MRP approach achieved a better overall image quality without compromising the details in the image compared to MAP-TV. No additional artifacts were introduced by MAP-MRP while this was not the case for MLEM (increased noise throughout iterations) and MAP-TV (checkerboard artifacts). The low statistics limited the performance of MAP-TV, whereas MLEM performance deteriorated with low statistics as well as partial ring configurations. MAP-MRP was also robust in terms of the selection of the penalization weight, making it easy-to-use in clinics. Based on these observations, MRP within MAP method makes a suitable candidate for penalization for the reconstruction of in-beam PET data.

VI. ACKNOWLEDGEMENTS

Authors would like to thank the graduate school of Tampere University of Technology for their financial support. We also thank the Center for Information Technology of the University of Groningen for their support and for providing access to the Peregrine high-performance computing cluster.

REFERENCES

- [1] M. T. Studenski, "Proton therapy dosimetry using positron emission tomography," *World J. Radiol.*, vol. 2, no. 4, p. 135, 2010.
- [2] C. H. Min, X. Zhu, B. A. Winey, K. Grogg, M. Testa, G. El Fakhri, T. R. Bortfeld, H. Paganetti, and H. A. Shih, "Clinical application of in-room positron emission tomography for in vivo treatment monitoring in proton radiation therapy," *Int. J. Radiat. Oncol. Biol. Phys.*, vol. 86, no. 1, pp. 183–189, May 2013.
- [3] K. Parodi, "Vision 20/20: Positron emission tomography in radiation therapy planning, delivery, and monitoring," *Med. Phys.*, vol. 42, no. 12, pp. 7153–7168, Dec. 2015.
- [4] T. Nishio, A. Miyatake, T. Ogino, K. Nakagawa, N. Saijo, and H. Esumi, "The Development and Clinical Use of a Beam ON-LINE PET System Mounted on a Rotating Gantry Port in Proton Therapy," *Int. J. Radiat. Oncol. Biol. Phys.*, vol. 76, no. 1, pp. 277–286, Jan. 2010.
- [5] S. P. Nischwitz, J. Bauer, T. Welzel, H. Rief, O. Jäkel, T. Haberer, K. Frey, J. Debus, K. Parodi, S. E. Combs, and S. Rieken, "Clinical implementation and range evaluation of in vivo PET dosimetry for particle irradiation in patients with primary glioma," *Radiother. Oncol.*, vol. 115, no. 2, pp. 179–185, May 2015.
- [6] P. Dendooven, H. J. T. Buitenhuis, F. Diblen, P. N. Heeres, A. K. Biegun, F. Fiedler, M. J. Van Goethem, E. R. Van Der Graaf, and S. Brandenburg, "Short-lived positron emitters in beam-on PET imaging during proton therapy," *Phys. Med. Biol.*, vol. 60, no. 23, pp. 8923–8947, Dec. 2015.
- [7] H. J. T. Buitenhuis, F. Diblen, K. W. Brzezinski, S. Brandenburg, and P. Dendooven, "Beam-on imaging of short-lived positron emitters during proton therapy," *Phys. Med. Biol.*, vol. 62, no. 12, pp. 4654–4672, Jun. 2017.
- [8] A. Miyatake, T. Nishio, T. Ogino, N. Saijo, H. Esumi, and M. Uesaka, "Measurement and verification of positron emitter nuclei generated at each treatment site by target nuclear fragment reactions in proton therapy," *Med. Phys.*, vol. 37, no. 8, pp. 4445–4455, Jul. 2010.
- [9] S. Surti and J. S. Karp, "Design considerations for a limited angle, dedicated breast, TOF PET scanner," *Phys. Med. Biol.*, vol. 53, no. 11, pp. 2911–2921, Jun. 2008.
- [10] W. Enghardt, P. Crespo, F. Fiedler, R. Hinz, K. Parodi, J. Pawelke, and F. Pönisch, "Charged hadron tumour therapy monitoring by means of PET," in *Nuclear Instruments and Methods in Physics Research, Section A: Accelerators, Spectrometers, Detectors and Associated Equipment*, 2004, vol. 525, no. 1–2, pp. 284–288.
- [11] H. Tashima, E. Yoshida, N. Inadama, F. Nishikido, Y. Nakajima, H. Wakizaka, T. Shinaji, M. Nitta, S. Kinouchi, M. Suga, H. Haneishi, T. Inaniwa, and T. Yamaya, "Development of a small single-ring OpenPET prototype with a novel transformable architecture," *Phys. Med. Biol.*, vol. 61, no. 4, pp. 1795–1809, Feb. 2016.
- [12] P. Crespo, G. Shakin, and W. Enghardt, "On the detector arrangement for in-beam PET for hadron therapy monitoring," *Phys. Med. Biol.*, vol. 51, no. 9, pp. 2143–2163, May 2006.
- [13] J. Cabello, I. Torres-Espallardo, J. E. Gillam, and M. Rafecas, "PET reconstruction from truncated projections using total-variation regularization for hadron therapy monitoring," *IEEE Trans. Nucl. Sci.*, vol. 60, no. 5, pp. 3364–3372, Oct. 2013.
- [14] P. Crespo, G. Shakin, F. Fiedler, W. Enghardt, and A. Wagner, "Direct time-of-flight for quantitative, real-time in-beam PET: A concept and feasibility study," *Phys. Med. Biol.*, vol. 52, no. 23, pp. 6795–6811, Dec. 2007.
- [15] C. Kurz, J. Bauer, M. Conti, L. Guérin, L. Eriksson, and K. Parodi, "Investigating the limits of PET/CT imaging at very low true count rates and high random fractions in ion-beam therapy monitoring," *Med. Phys.*, vol. 42, no. 7, pp. 3979–3991, Jun. 2015.
- [16] S. Surti, W. Zou, M. E. Daube-Witherspoon, J. McDonough, and J. S. Karp, "Design study of an in situ PET scanner for use in proton beam therapy," *Phys. Med. Biol.*, vol. 56, no. 9, pp. 2667–2685, 2011.
- [17] V. Y. Panin, G. L. Zeng, and G. T. Gullberg, "Total variation regulated EM algorithm," *IEEE Trans. Nucl. Sci.*, vol. 46, no. 6, pp. 2202–2210, 1999.
- [18] S. Kinouchi, T. Yamaya, H. Tashima, E. Yoshida, H. Ito, and M. Suga, "Total variation minimization for in-beam PET image reconstruction," in *IEEE Nuclear Science Symposium Conference Record*, 2012, pp. 3412–3414.
- [19] C. Hui, D. Robertson, and S. Beddar, "3D reconstruction of scintillation light emission from proton pencil beams using limited viewing angles - A simulation study," *Phys. Med. Biol.*, vol. 59, no. 16, pp. 4477–4492, Aug. 2014.
- [20] S. Alenius and U. Ruotsalainen, "Bayesian image reconstruction for emission tomography based on median root prior," *Eur. J. Nucl. Med.*, vol. 24, no. 3, pp. 258–265, Mar. 1997.
- [21] S. Alenius, "Using local median as the location of the prior distribution in iterative emission tomography image reconstruction," *IEEE Trans. Nucl. Sci.*, vol. 45, no. 6 PART 2, pp. 3097–3104, 1998.
- [22] A. Seret, "Median root prior and ordered subsets in Bayesian image reconstruction of single-photon emission tomography," *Eur. J. Nucl. Med.*, vol. 25, no. 3, pp. 215–219, Mar. 1998.
- [23] G. Kontaxakis, L. G. Strauss, T. Thireou, M. J. Ledesma-Carbayo, A. Santos, S. A. Pavlopoulos, and A. Dimitrakopoulou-Strauss, "Iterative image reconstruction for clinical PET using ordered subsets, median root prior, and a web-based interface," *Mol. Imaging Biol.*, vol. 4, no. 3, pp. 219–231, Jun. 2002.
- [24] U. Tuna, A. Solhberg, and U. Ruotsalainen, "Can We Reduce SPECT Acquisition Time Using MAP-EM Reconstruction?," *J. Pattern Recognit. Intell. Syst.*, vol. 1, no. 3, pp. 54–63, 2013.
- [25] D. J. Kadmas, "LOR-OSEM: Statistical PET reconstruction from raw line-of-response histograms," *Phys. Med. Biol.*, vol. 49, no. 20, pp. 4731–4744, Oct. 2004.

- [26] A. J. Reader, "List-mode EM algorithms for limited precision high-resolution PET image reconstruction," *Int. J. Imaging Syst. Technol.*, vol. 14, no. 3, pp. 139–145, 2004.
- [27] A. J. Reader, K. Erlandsson, M. A. Flower, and R. J. Ott, "Fast accurate iterative reconstruction for low-statistics positron volume imaging," *Phys. Med. Biol.*, vol. 43, no. 4, pp. 835–846, 1998.
- [28] C. Kato, U. Ruotsalainen, H. Laine, S. Alenius, H. Iida, P. Nuutila, and J. Knuuti, "Iterative reconstruction based on median root prior in quantification of myocardial blood flow and oxygen metabolism," *J. Nucl. Med.*, vol. 40, no. 5, pp. 862–7, 1999.
- [29] S. Alenius and U. Ruotsalainen, "Generalization of median root prior reconstruction," *IEEE Trans. Med. Imaging*, vol. 21, no. 11, pp. 1413–1420, 2002.
- [30] J. Allison, "Geant4 – A Simulation Toolkit," *Nucl. Phys. News*, vol. 17, no. 2, pp. 20–24, Aug. 2007.
- [31] S. Jan, D. Benoit, E. Becheva, T. Carlier, F. Cassol, P. Descourt, T. Frisson, L. Grevillot, L. Guigues, L. Maigne, C. Morel, Y. Perrot, N. Rehfeld, D. Sarrut, D. R. Schaart, S. Stute, U. Pietrzyk, D. Visvikis, N. Zahra, *et al.*, "GATE V6: A major enhancement of the GATE simulation platform enabling modelling of CT and radiotherapy," *Phys. Med. Biol.*, vol. 56, no. 4, pp. 881–901, Feb. 2011.
- [32] R. L. Siddon, "Fast calculation of the exact radiological path for a three dimensional CT array," *Medical Physics*, vol. 12, no. 2, pp. 252–255, 1985.
- [33] H. T. Van Dam, G. Borghi, S. Seifert, and D. R. Schaart, "Sub-200 ps CRT in monolithic scintillator PET detectors using digital SiPM arrays and maximum likelihood interaction time estimation," *Phys. Med. Biol.*, vol. 58, no. 10, pp. 3243–3257, May 2013.
- [34] "Philips Vereos PET/CT," 2014. [Online]. Available: http://incenter.medical.philips.com/doclib/enc/10264938/452296298357_VereosBrochureREV_FNL_HR.pdf?func=doc.Fetch&nodeid=10264938&vernum=1. [Accessed: 30-Mar-2017].
- [35] S. Helmbrecht, W. Enghardt, K. Parodi, B. Didering, J. Debus, D. Kunath, M. Priegnitz, and F. Fiedler, "Analysis of metabolic washout of positron emitters produced during carbon ion head and neck radiotherapy," *Med. Phys.*, vol. 40, no. 9, p. 091918, Sep. 2013.
- [36] C. Burger, G. Goerres, S. Schoenes, A. Buck, A. Lonn, and G. Von Schulthess, "PET attenuation coefficients from CT images: Experimental evaluation of the transformation of CT into PET 511-keV attenuation coefficients," *Eur. J. Nucl. Med.*, vol. 29, no. 7, pp. 922–927, 2002.
- [37] C. Robert, N. Fourrier, D. Sarrut, S. Stute, P. Gueth, L. Grevillot, and I. Buvat, "PET-based dose delivery verification in proton therapy: A GATE based simulation study of five PET system designs in clinical conditions," *Phys. Med. Biol.*, vol. 58, no. 19, pp. 6867–6885, 2013.
- [38] Y. Teng and T. Zhang, "Three penalized EM-type algorithms for PET image reconstruction," *Comput. Biol. Med.*, vol. 42, no. 6, pp. 714–723, 2012.
- [39] M. Conti, "Focus on time-of-flight PET: The benefits of improved time resolution," *Eur. J. Nucl. Med. Mol. Imaging*, vol. 38, no. 6, pp. 1147–1157, Jun. 2011.

PUBLICATION V

**Combining Dual-Tree Complex Wavelets and Multiresolution in Iterative
CBCT reconstruction with Application to Metal Artifact Reduction**

D. Us, U. Ruotsalainen, S. Pursiainen

submitted to BMC Biomedical Engineering Online, July 2018

Publication reprinted with the permission of the copyright holders.

RESEARCH

Combining Dual-Tree Complex Wavelets and Multiresolution in Iterative CBCT reconstruction with Application to Metal Artifact Reduction

Defne Us^{1,2*}, Ulla Ruotsalainen² and Sampsa Pursiainen¹

*Correspondence: defne.us@tut.fi

¹Laboratory of Mathematics,
Tampere University of Technology,
Korkeakoulunkatu 3, 33720
Tampere, Finland

Full list of author information is
available at the end of the article

Abstract

This paper investigates the benefits of data filtering via complex dual wavelet transform for metal artifact reduction (MAR). The advantage of using complex dual wavelet basis for MAR was studied on simulated dental computed tomography (CT) data for its efficiency in terms of noise reduction and removal of secondary artifacts. Dual-tree complex wavelet transform (DT-CWT) was selected due to its enhanced directional analysis of image details compared to the ordinary wavelet transform. DT-CWT was used for multiresolution decomposition within a modified total variation (TV) regularized inversion algorithm. The DT-CWT We have tested the multiresolution TV (MRTV) approach with DT-CWT on a 2D polychromatic jaw phantom model with Gaussian and Poisson noise. High noise and sparse measurement settings were used to assess the performance of DT-CWT. The results were compared to the outcome of the single-resolution reconstruction and filtered back projection (FBP) techniques as well as reconstructions with Haar wavelet basis. The results indicate that filtering of wavelet coefficients with DT-CWT effectively removes the noise without introducing new artifacts after inpainting. The multiresolution reconstruction with DT-CWT is also more robust when reconstructing the data with sparse projections compared to the single resolution approach and Haar wavelets.

Keywords: cone beam computed tomography (CBCT); dual tree complex wavelet transform; iterative reconstruction; metal artifact reduction; multiresolution

Introduction

Cone beam computed tomography (CBCT) has been increasingly used over the past decade as it provides information on bone size, presence of foreign materials, surrounding anatomical structures such as nerves and sinuses, precise localization of implant placement sites, and surgical planning decisions [1, 2]. With the increased acceptance, affordability and accessibility of metallic restorations in forms of dental implants, fillings, crowns, screws, nails, prosthesis and plates in dentistry, and the increasing popularity of CBCT in image-guided therapy, dental CT specific metal artifact reduction (MAR) algorithms became one of the focus areas in the scientific research [3]. The attenuation of high density objects such as stainless steel, gold alloys, silver amalgam, platinum, lead, tin and aluminum, can corrupt the images of the underlying anatomical structures in dental CT, allowing fewer photons to reach detectors. This photon starvation corrupts the projection data, leading to streak artifacts over the surrounding tissue upon back-projection. These artifacts

can reduce the applicability of dental CT by hindering the underlying anatomical structures [4].

The aim of MAR methods is to limit the possible artifacts in the vicinity of the metals. MAR methods can be generally divided into two main categories: (1) interpolation/completion of projection data and (2) iterative reconstruction methods. The former approach is not sufficient in complicated cases such as multiple metals [5]. The combination of these two categories is also possible and it can further improve the reconstruction quality. An overview of these methods is provided in [6].

Inpainting is one of the most commonly used projection completion methods due to its high computational efficiency [5]. It is an interpolation based method for filling the missing information in an image by interpolating the information surrounding it. Inpainting was introduced in signal processing by [7] and it has been widely used in MAR in projection domain [5, 8] and wavelet domain [9]. In practice, inpainting replaces the gaps in the data with NaNs and then fill them by interpolating the intensity values surrounding the NaNs. The inpainting methods in this work was implemented via the MATLAB code of John D’Errico ^[1] [10]. Although inpainting fills the gaps in an image efficiently, it can lead to secondary artifacts during analytic reconstruction due to discontinuities at the boundary pixels, e.g., at the metal-tissue boundary. In order to prevent such artifacts, we propose filtering the projection data in dual complex wavelet basis within a multiresolution framework, which combines inpainting [10] and iterative total variation (TV) reconstruction. The multiresolution iterative total variation (MRTV) is an extension of the classical single-resolution TV iteration [11, 12, 13]. It utilizes a coarse-to-fine approach, in which the coarse image details are reconstructed before the finer ones to enhance the regularity, suppress the noise, and avoid the secondary artifacts after inpainting [14, 15, 16].

The multiresolution decomposition needed in MRTV can be obtained using wavelets, which have been successfully applied in MAR to resolve some of the issues with poor performance, instability and computational complexity of existing methods [4, 16, 8]. The authors in [16] implemented a wavelet-based filtering for MAR in CT data with hip joint prosthesis, and it was found to be effective in reducing the artifacts from beam hardening and photon starvation. Following a similar reasoning, we chose to use wavelet coefficients to distinguish different frequency components and filter the high frequency artifacts caused by metals and noise without disturbing the edges of the object. For achieving the best possible performance, we apply the dual-tree complex wavelet transform (DT-CWT) [17, 18, 19]. The DT-CWT is based on two real discrete wavelet transforms (DWTs), which give the real and imaginary parts of the DT-CWT separately. As a directionally accurate transform, 2D DT-CWT can recognize the orientation of the image fluctuations, making it considerably less sensitive to the artifacts related to alteration or compression of the coefficients as compared to the classical wavelets, e.g., Daubechies or biorthogonal wavelets used in [16]. The complex wavelet transform (CWT) also achieves perfect reconstruction and the dual tree approach ensures this when decomposition level is greater than one [20]. In contrast to the ordinary 2D wavelet transform, which includes vertical, horizontal and diagonal direction modes, DT-CWT oversamples the

^[1]<https://se.mathworks.com/matlabcentral/fileexchange/4551-inpaint-nans>

target image with a doubled directional selectivity. Consequently, it distinguishes both ascending and descending curves in the image, whereas DWT does not. This is essential for preserving the reconstruction quality as good as possible. The advantages of DT-CWT was utilized within the multiresolution framework in order to achieve good noise filtering without filtering out the details in the image. In this study, our goal is to find out, how MRTV approach performs compared to the ordinary single resolution TV (SRTV) regularization and also to the classical filtered backprojection (FBP) technique.

The influence of angular density on the reconstructions was studied by using different number of projections. The results with sparse projections would be relevant with respect to lowering the total radiation dose [21, 22]. Additionally, the stability of the algorithm against the total number of projections could make it applicable for various CBCTs available on the market. For instance, in 2013, the number of projections acquired ranged from 180 to 1024. The Kodak CS 9300C CBCT device utilizes 180 projections for a total rotation angle of 180 degrees, while most devices deliver 360 projections per full angle rotation [23].

Materials and Methods

Dataset preparation

As the simulation dataset, we used the density map of a 2D jaw phantom (1024×1024). This dataset was based on the FORBILD jaw phantom (<http://www.imp.uni-erlangen.de/forbild/english/results/index.htm>). Metal (golden crown), teeth, jaw bone (cortical), soft tissue (modeled as water) and air gap inside the mouth were modeled with density values of 19.32, 2.99 (enamel), 1.92, 1 and 0, respectively. The locations for metallic implants in the image and projection domains can be seen in Fig. 1 as well as regions-of-interest (ROIs). In order to avoid committing "inverse crime" during the reconstruction, the sinogram was constructed on a fine grid of 1024 pixels, then reconstructed on a 512-pixel grid, similar to the approach of Nuyts *et al.* [24]. The projection data consisted of 768 radial bins and 256 angular views, covering 180 degrees.

The energy dependent mass attenuation coefficients (with coherent scattering) of gold, bone, hard tissue and soft tissue were obtained from the National Institute of Standards and Technology (NIST) database^[2]. The mass attenuation coefficient for the tooth was approximated using the material composition of enamel from [25] and NIST database^[3]. For modeling the beam hardening, the 80 kVp spectrum was used with 1 mm Al filtration from Fessler's IRT toolbox [26]. A parallel beam structure was assumed for the construction of the system matrix. Both Poisson and Gaussian noise were modeled in the sinogram construction, following the description of [27], which was also used in TIGRE Toolbox. For Poisson noise, the total emitted photon count (I_0) was taken as 10^5 and a zero mean additive Gaussian noise was used with standard deviation of 10.

Three different measurement settings were used to evaluate the algorithm's performance against noise and sparsity of measurements. In the first one (Configuration I), the number of projections was 256 with Poisson and Gaussian noise. In

^[2]<https://physics.nist.gov/PhysRefData/XrayMassCoef/tab4.html>

^[3]<https://physics.nist.gov/PhysRefData/Xcom/html/xcom1.html>

Configuration II, a sparse pattern of 128 projections in addition to the noise. In Configuration III, the data consisted of 256 projections without Gaussian noise to assess the performance of the single and multiresolution methods under more ideal conditions without changing the count statistics.

The metals were extracted by global thresholding from the projection data. For the sake of simplicity in evaluating the performance of the suggested methods, perfect segmentation of the metals was assumed. The gaps left on the sinogram after metal extraction were filled via inpainting.

Wavelets

The ordinary real (orthogonal) DWT [28, 29] is based on a low- and high-pass filter function $\phi : \mathbb{R} \rightarrow \mathbb{R}$ and $\psi : \mathbb{R} \rightarrow \mathbb{R}$ which together enable decomposing a given signal $f(t)$ as given by

$$f(t) = \sum_{k=-\infty}^{\infty} \alpha_k \phi(t-k) + \sum_{\ell=0}^{\infty} \sum_{k=-\infty}^{\infty} \beta_{k,\ell} 2^{\ell/2} \psi(2^\ell t - k). \quad (1)$$

The filter functions are orthogonal and normalized to one, i.e., the product between two different filter functions integrated over the real line is zero and $\int_{-\infty}^{\infty} \phi(t-k)^2 dt = \int_{-\infty}^{\infty} 2^\ell \psi(2^\ell t - k)^2 dt = 1$. Consequently, the coefficients α_k and $\beta_{k,\ell}$ can be obtained via the following integrals:

$$\alpha_k = \int_{-\infty}^{\infty} f(t) \phi(t-k) dt \quad (2)$$

$$\beta_{k,\ell} = \int_{-\infty}^{\infty} f(t) 2^{\ell/2} \psi(2^\ell t - k) dt. \quad (3)$$

Furthermore, the DWT conserves signal energy, meaning that the Parseval's identity holds:

$$\int_{-\infty}^{\infty} f(t)^2 dt = \sum_{k=-\infty}^{\infty} \alpha_k^2 + \sum_{\ell=0}^{\infty} \sum_{k=-\infty}^{\infty} \beta_{k,\ell}^2. \quad (4)$$

Together the coefficients can be organized into a tree-structured hierarchy of multiple resolution levels: each level has two branches, one for low- and one for high-pass filter coefficients.

The two-dimensional filter functions can be obtained as separable products between their one-dimensional counterparts, i.e., $\phi(x, y) = \phi(x)\phi(y)$, $\psi_H(x, y) = \phi(x)\psi(y)$, $\psi_V(x, y) = \psi(x)\phi(y)$, and $\psi_D(x, y) = \psi(x)\psi(y)$. The high-pass filters $\psi_H(x, y)$, $\psi_V(x, y)$, and $\psi_D(x, y)$ correspond to a horizontal, vertical and diagonal directional mode, respectively. Characteristic to the 2D DWT is that, due to their symmetry in the Fourier domain, these modes do not distinguish between upward and downward slopes in the image [19]. Consequently, DWT easily produces checkerboard-like dense and non-directional artifacts around edges, if the coefficients are altered or compressed. The lowest-order case of the DWT is constituted by the piecewise constant Haar wavelets which have been previously used together with TV in reconstruction [9, 30]. Therefore, it was also used here for comparison.

In DT-CWT, the low- and high-pass filter function is assumed to be of the form

$$\phi(t) = \phi_h(t) + j\phi_g(t) \quad \text{and} \quad \psi(t) = \psi_h(t) + j\psi_g(t), \quad (5)$$

where $\phi_h(t)$, $\phi_g(t)$, $\psi_h(t)$, and $\psi_g(t)$ are real functions. The dual-tree structure follows as each of the pairs $\phi_h(t)$, $\psi_h(t)$ and $\phi_g(t)$, $\psi_g(t)$ forms a real-valued and orthogonal wavelet-tree.

In two dimensions, the high-pass filters of the DT-CWT have altogether six directional modes [19], corresponding to the real part of the separable products $\phi(x)\psi(y)$, $\phi(x)\psi(y)$, $\psi(x)\phi(y)$, $\psi(x)\phi(y)$, $\psi(x)\psi(y)$, and $\psi(x)\psi(y)$ and the angular orientations of -63, 63, -27, 27, -45, and 45 degrees with respect to the x-axis, respectively. Of these, the first two are nearly horizontal, 3rd and 4th one nearly vertical and the last two diagonal modes.

As the 2D DT-CWT can recognize the orientation of the image fluctuations, it is considerably less sensitive to the artifacts related to alteration or compression of the coefficients as compared to the DWT. In particular, it does not produce the checkerboard pattern in the vicinity of edges.

Total Variation Regularization

The goal of any image reconstruction in a linear system is to invert the equation

$$\mathbf{y} = \mathbf{L}\mathbf{x} + \mathbf{n}, \quad (6)$$

where \mathbf{x} is the image to be reconstructed, the vector \mathbf{y} contains the measurement (projection) data, the matrix \mathbf{L} is a discretized Radon transform (Radon matrix), and \mathbf{n} is a measurement noise term. A regularized solution of (6) can be obtained through the following:

$$\mathbf{x}_{\ell+1} = (\mathbf{L}^T\mathbf{L} + \mathbf{D}\mathbf{\Gamma}_\ell\mathbf{D})^{-1}\mathbf{L}^T\mathbf{y}, \quad (7)$$

where $\mathbf{\Gamma}_\ell$ is a weighting matrix that satisfies $\mathbf{\Gamma}_0 = \mathbf{I}$ and $\mathbf{\Gamma}_\ell = \text{diag}(|\mathbf{D}\mathbf{x}_\ell| + \gamma\mathbf{I})^{-1}$ for $\ell \geq 1$ with a suitably chosen regularization parameter $\gamma \geq 0$. \mathbf{D} is the regularization matrix given by

$$D_{i,j} = \frac{\alpha(2\delta_{i,j} - 1) \int_{P_i \cap P_j} ds}{\max_{i,j} \int_{P_i \cap P_j} ds} + \beta\delta_{i,j}, \quad \text{with} \quad \delta_{i,j} = \begin{cases} 1, & \text{if } j = i, \\ 0, & \text{otherwise,} \end{cases} \quad (8)$$

with P_i and P_j denoting the boundary of the i^{th} and j^{th} pixel, respectively. Their intersection coincides with the edges shared by these pixels. The governing regularization parameter determining the strength of the TV regularization is α . The role of β and γ is mainly to ensure the invertibility of the matrices \mathbf{D} and $\mathbf{\Gamma}_\ell$

so that the TV iteration does not diverge. The first term in (8) penalizes the jumps over the pixel edges and the second one corresponds to the norm of \mathbf{x} . In this work, β was fixed at 10^{-8} . The conjugate gradient method was applied for matrix inversion with the number of steps fixed to 100. If this iteration converges, it minimizes the regularized objective function $F(\mathbf{x}) = \|\mathbf{L}\mathbf{x} - \mathbf{y}\|_2^2 + 2\|\mathbf{D}\mathbf{x}\|_1$ in which the latter norm is the total variation of \mathbf{x} , if $\beta = 0$ [31]. Consequently, the reconstructed image is likely to have large connected subsets close to constant, which helps to reduce noise, while preserving the edges. In this study, we call (7) the single resolution TV (SRTV) approach. The SRTV-H refers to the stronger penalization of TV with a larger α value.

Multiresolution TV Regularization

We propose approaching MAR via a multiresolution TV (MRTV) technique, that is, a coarse-to-fine extension (see Appendix) of the algorithm (7). To explain this idea, we introduce the following definition of the numerical null-space [32, 15]:

$$S_\varepsilon^- = \{x \mid \|\mathbf{L}\mathbf{x}\| \leq \varepsilon\|\mathbf{x}\|\}. \quad (9)$$

Here ε denotes the floating-point accuracy, which is mainly concentrated on the fine image fluctuations. We assume that the target spaces of the wavelet low- and high-pass filter pair provide approximations of the space of strongly suppressed image details S_ε^- and that of the well-detectable details $S_\varepsilon^+ = \{0\} \cup \{x \mid \|\mathbf{L}\mathbf{x}\| > \varepsilon\|\mathbf{x}\|\}$, respectively. These spaces decompose the candidate solution space as given by $\mathbb{R}^n = S_\varepsilon^+ \oplus S_\varepsilon^-$. The aim of the coarse-to-fine approach is to separate S_ε^+ and S_ε^- in the reconstruction process in order to maximize the distinguishability of the details belonging to S_ε^- . Processing the coarse details before the finer ones can approximately separate the strongly suppressed fluctuations of S_ε^- from the well-detectable ones belonging to the space $S_\varepsilon^+ = \{0\} \cup \{x \mid \|\mathbf{L}\mathbf{x}\| > \varepsilon\|\mathbf{x}\|\}$. The low- and high-pass wavelet filters can be obtained via a wavelet decomposition by zeroing all the high-pass and low-pass coefficients, respectively. In other words, the reconstruction of each wavelet level can help separating the fine image details from the undesired components of the image such as noise and artifacts.

Numerical Experiments

The present reconstruction approach was validated in numerical experiments using the jaw phantom described earlier. The reconstruction procedure included the following four stages:

- 1 detecting the metals in the sinogram via global thresholding,
- 2 Laplacian smoothed inpainting of the metals using the algorithm in [10],
- 3 DT-CWT denoising with a given hard threshold percent (0 % or 80 %), and
- 4 inversion of the data via the MRTV, MRTV-F, SRTV, SRTV-H, or FBP technique.

The hard threshold refers to the percentage of the smallest wavelet coefficients which are set to zero. It aims to further reduce the noise in the sinogram before reconstruction. In MRTV-F, with 80 % threshold, only the largest 20 % of the wavelet coefficients were used in the reconstruction. The DT-CWT was used in the inversion stage (4) to obtain the multiresolution decomposition for MRTV.

The regularization parameter values were chosen empirically. MRTV, MRTV-F and SRTV were optimized for Configuration III. The minimal level of regularization sufficient to suppress any staircase patterns was sought for SRTV. The regularization strength applied in the case of MRTV was matched roughly with that of SRTV. In SRTV-H, slightly higher value of α was used for an enhanced noise tolerance. For SRTV and SRTV-H, it was necessary to choose $\gamma > 0$, and it was set to $\gamma = 10^{-2}$. For MRTV, the optimal performance was obtained with $\gamma = 0$. The number of MRTV and SRTV iteration steps taken in computing a single reconstruction was set to be three.

The number of nested resolution levels used in MRTV computations and denoising was set to be four. The multiresolution inverse estimates computed without and with DT-CWT denoising are referred to as MRTV and MRTV-F, respectively. The regularization parameter α was chosen empirically as 4. MRTV results were compared with FBP and single resolution estimates SRTV and SRTV-H corresponding to $\alpha = 15$ and $\alpha = 20$, respectively. In FBP, the Hamming filter with a high-frequency cut-off of 1 was used in order to decrease high frequency artifacts. Although all configurations that were implemented for DT-CWT were also implemented with Haar wavelets, the best overall performing reconstruction with Haar wavelets is depicted in the results, which was found to be filtered multiresolution approach, denoted with Haar-MRTV-F. The details for MRTV, MRTV-F, SRTV, SRTV-H, FBP and Haar-MRTV-F have been included in Table 1.

Table 1 Details for the reconstructions computed in the numerical experiments.

Name	Levels	Filter	Used wavelet coefficients (%)	α
MRTV	4	-	100	4
MRTV-F	4	DT-CWT	20	4
SRTV	1	-	100	15
SRTV-H	1	-	100	20
FBP	1	Hamming	-	-
Haar-MRTV	4	Haar	100	4

The performance of denoising of the reconstruction methods were analyzed via the root mean squared error (RMSE), in which the jaw phantom without metals was taken as the ground truth. At the locations of the metal implants, the intensity values of the ground truth vector was set to be equal to the intensity value of the teeth. Structural similarity index (SSIM) was used to evaluate the overall similarity of the reconstructed images to the ground truth [33]. The SSIM is 1 when the reference image is identical to the image to be evaluated. As the similarity between images decrease, so does the SSIM value. The SSIM values were calculated for all ROIs as well as the full image. RMSE and SSIM values were evaluated for the full image and the ROIs 1–3 (see Fig. 1). ROI 1 corresponds to the soft tissue surrounding the teeth and ROIs 2 and 3 include a single tooth with gold implant.

All the scripts were written using MATLAB version R2016b. To run the computations, we used a high-end Lenovo P510 workstation equipped with two Intel Xeon E5-2620v4 processors and 192 GB RAM. The projection matrices for the multiresolution transform were stored as sparse arrays.

Results

The reconstructed images are presented in Fig. 2. The secondary artifacts in FBP around ROI 2 are slightly less pronounced with the DT-CWT filtering step. These

artifacts are almost completely vanished once multiresolution approach is combined with DT-CWT. The images reconstructed with Haar wavelets are so pixelized that it is not possible to evaluate the secondary artifacts. When images with the tooth within ROI 3 are visually assessed, the observations for the ROI 2 still apply. Additionally, in SRTV, artifacts caused by single-resolution filtering are visible, but these artifacts are decreased by the increased penalty weight in SRTV-H. The contrast difference between the tooth and the inpainted metal is pronounced in the single resolution images and the FBP, whereas this difference is significantly less with MRTV and MRTV-H.

The RMSE and SSIM results are shown in Fig. 3. For Configurations I (noisy) and II (noisy and sparse), the multiresolution approach with DT-CWT fared better with high SSIM and lower RMSE compared to single resolution approaches. FBP after inpainting had the lowest RMSE among all reconstructions in Configuration I, but the RMSE rapidly increased with sparse measurements in Configuration II. In general, the filtering of wavelet coefficients improved the RMSE and SSIM values for Configuration II. In Configuration I, however, the filtering deteriorated all RMSE values despite the marginal improvement in SSIM. Increasing the penalty weight in SRTV improved the overall SSIM and RMSE values for Configurations I and II. The exception was the slight increase in RMSE in ROIs 2 and 3 for Configuration I. Due to the pixelization in reconstruction with Haar wavelets, its RMSE was higher than other methods even in the noiseless measurements. In the case of Configuration III (noiseless data), all the methods with DT-CWT achieved similar RMSE and SSIM due to the preliminary stage optimization of reconstruction parameters (Section 1). For dense projection data in Configuration I, the multiresolution with wavelets (both Haar and DT-CWT) performed better than single-resolution approaches in ROI 1. For the sparse projections in Configuration II, MRTV with DT-CWT outperformed the Haar wavelets.

The line profiles in Fig. 4 were calculated along the red line in Fig. 1. Based on these line profiles, it can be seen that the MRTV with wavelet filtering suppresses the noise better than SRTV with a high penalty (SRTV-H). The pixelization of the Haar wavelet reconstruction is also visible in the line profile. The distortions in the line profiles of SRTV-H and Haar-MRTV-F near the metallic region become more apparent in Configuration II, while MRTV profile is closer to the ground truth.

Discussion

This study focused on enhancing the reconstruction quality of iterative regularization via the dual-tree complex wavelet transform (DT-CWT) [17, 18, 19] in dental CT, combined with multiresolution. Although FBP resulted in comparable values of RMSE and SSIM with complete data and low noise scenarios, the difference of the proposed method became apparent with sparse data. The central finding of this study was that the DT-CWT equipped MRTV inversion technique was more robust in terms of noise reduction and artifact reduction for sparse data. This observation was supported by the numeric evaluation and also by visual comparison. Although part of this robustness of the reconstruction compared to FBP can be attributed to TV penalization, the difference in error and similarity measures of Haar and DT-CWT point at the importance in selection of the coefficients to be filtered.

Based on our results, DT-CWT provided virtually an artifact-free multiresolution basis, which can be observed based on the nearly identical outcome of MRTV and SRTV in the case of the noiseless data (Configuration III). The conventional wavelets used in the preliminary tests, in particular, the Haar basis [28], led to pixelization of the final reconstruction. That is, the correction steps for the finer resolutions did not match accurately enough with the coarse level estimate. Hence, DT-CWT was found to be vital for the appropriate function of MRTV. Some ringing effects were observed for the individual resolution levels, but, the final estimate did not suffer from ringing. Other potential multiresolution bases for MRTV are provided by ridgelets and curvelets [34, 35, 36] which similarly to DT-CWT cover an extended set of orientations compared to the classical wavelets.

Sinogram denoising with a 80 % hard threshold (MRTV-F) improved the RMSE values with sparse projections (Configuration II). However, the RMSE results of the dense projections with filtering were inferior to the outcome obtained with MRTV despite the improvement in SSIM, suggesting that some details were lost in the thresholding process along with some noise reduction. This suggests that additional denoising in single resolution is a not as effective technique recovery of the intensity values as employing a multiresolution decomposition in iterative reconstruction. We emphasize that present hard threshold filter in MRTV-F can be improved, e.g., via a soft threshold and regional adaptivity, especially, regarding the metal implants.

Using multiple resolution levels was also found to be preferable compared to controlling the regularization strength. With sparse projection data used in Configuration II, the SRTV-H performed equally well compared to MRTV in terms of RMSE, possibly due to the strong penalization of the noise. With SRTV-H, the overall image quality could be improved with respect to the artifacts by increasing the level of the regularization, but, with the cost of decreased image sharpness. The line profiles, however, showed a high positive bias for the tooth around the metal and lower intensity values for the metallic implant. In contrast, MRTV achieved an enhanced accuracy for the coarse details while maintaining the sharpness at the level of SRTV. Another important observation was that MRTV successfully reconstructed both 256 and 128 projection angles utilized in Configuration I and II, respectively. In general, the coarse-to-fine reconstruction approach seems to be advantageous regarding MAR, where reconstructing the implanted teeth accurately can be difficult due to the inpainted sinogram regions and, thereby, the incompleteness of the data. As suggested by the present study, recovering the coarse level fluctuations before the finer ones can result in a more accurate tooth boundaries than, if the whole image is reconstructed at once. This can be understood, since for the present inverse problem the numerical null space S_{ϵ}^{-} [15, 32] is non-trivial and there is infinitely many candidate solutions which fit the incomplete data. Hence, in addition to TV, a multiresolution setting akin to the present one might work also with other reconstruction approaches. Note that it is possible to change the multiresolution levels depending on the spatial resolution of the image. For instance, for a 256×256 image, the resolution level would be 3, while 5 levels could be chosen for a 1024×1024 image.

An important future work direction is to validate the present DT-CWT based MRTV approach in 3-dimensional clinical dental CT data. For that purpose, the

current implementation of MRTV needs to be sped up. An obvious solution would be to employ a graphics processing unit (GPU) for the inverse computations instead of a standard processor. The denoising technique used in MRTV-F can also be improved in order to achieve optimal imaging results. In addition to the sinogram, also the reconstruction can be filtered using DT-CWT. This approach was omitted in this study, as it did not enhance the RMSE compared to MRTV in the preliminary tests.

Conclusion

In this work, we showed how DT-CWT can be applied in the tomographic reconstruction process via a multiresolution (coarse-to-fine) version of a classical TV regularization algorithm. The numerical experiments were aimed at minimizing the reconstruction errors due to the inpainting of metallic regions in the projection data. The multiresolution technique (MRTV) was compared to the single-resolution TV approach, for which a lower and higher regularization strength (SRTV and SRTV-H) was used. The results were also compared with reconstructions using Haar wavelet basis. Qualitative and quantitative results showed that data filtering with DT-CWT combined with multiresolution reconstruction is beneficial for recovering the details of images while reducing the noise with filtering at each resolution level. The robustness of the reconstruction with sparse projections using DT-CWT indicates the feasibility of these wavelets especially for sparse measurements. This could potentially help decreasing the radiation dose by reconstructing high quality images from sparse projection angles.

Competing interests

The authors declare that they have no competing interests.

Author's contributions

DU has constructed the phantom, reconstructed the images and wrote the article. SP has written the code for the basis of reconstruction and supervised DU in preparation of the contents of the manuscript. UR has advised on the preparation of the work and commented on the writing of the article.

Acknowledgements

DU and SP were supported by the Academy of Finland Key Project 305055 and the AoF Centre of Excellence in Inverse Problems. We also thank the graduate school of Tampere University of Technology for their financial support.

Author details

¹Laboratory of Mathematics, Tampere University of Technology, Korkeakoulunkatu 3, 33720 Tampere, Finland.

²Laboratory of Signal Processing, Tampere University of Technology, Korkeakoulunkatu 1, 33720 Tampere, Finland.

References

1. Scarfe, W.C., Farman, A.G., Sukovic, P., *et al.*: Clinical applications of cone-beam computed tomography in dental practice. *Journal-Canadian Dental Association* **72**(1), 75 (2006)
2. De Vos, W., Casselman, J., Swennen, G.: Cone-beam computerized tomography (cbct) imaging of the oral and maxillofacial region: a systematic review of the literature. *International journal of oral and maxillofacial surgery* **38**(6), 609–625 (2009)
3. Ibraheem, I.: Reduction of artifacts in dental cone beam ct images to improve the three dimensional image reconstruction. *Journal of Biomedical Science and Engineering* **5**(1), 409–415 (2012)
4. Mehranian, A., Ay, M.R., Rahmim, A., Zaidi, H.: X-ray CT Metal Artifact Reduction Using Wavelet Domain L_0 Sparse Regularization. *IEEE Transactions on Medical Imaging* **32**(9), 1707–1722 (2013)
5. Duan, X., Zhang, L., Xiao, Y., Cheng, J., Chen, Z., Xing, Y.: Metal artifact reduction in ct images sinogram tv inpainting. In: *IEEE Nuclear Science Symposium Conference Record*, pp. 4175–4177. IEEE, ??? (2008). doi:10.1109/NSSMIC.2008.4774201
6. Tang, Z., Hu, G., Zhang, H.: Efficient metal artifact reduction method based on improved total variation regularization. *Journal of Medical and Biological Engineering* **34**(3), 261–268 (2013). doi:10.5405/jmbe.1358
7. Bertalmio, M., Sapiro, G., Caselles, V., Ballester, C.: Image inpainting. In: *Proceedings of the 27th Annual Conference on Computer Graphics and Interactive Techniques. SIGGRAPH '00*, pp. 417–424. ACM Press/Addison-Wesley Publishing Co., New York, NY, USA (2000). doi:10.1145/344779.344972. <http://dx.doi.org/10.1145/344779.344972>

8. Mehranian, A., Ay, M.R., Rahmim, A., Zaidi, H.: Sparsity constrained sinogram inpainting for metal artifact reduction in x-ray computed tomography. In: 2011 IEEE Nuclear Science Symposium Conference Record, pp. 3694–3699. IEEE, ??? (2011). doi:10.1109/NSSMIC.2011.6153697. <http://ieeexplore.ieee.org/document/6153697/>
9. Chan, T.F., Zhou, H.-M.: Total variation wavelet thresholding. *Journal of Scientific Computing* **32**(2), 315–341 (2007). doi:10.1007/s10915-007-9133-0
10. D'Errico, J.: Inpaint nans. MATLAB Central File Exchange (2004)
11. Sidky, E.Y., Pan, X.: Image reconstruction in circular cone-beam computed tomography by constrained, total-variation minimization. *Physics in medicine and biology* **53**(17), 4777 (2008)
12. Vogel, C.R., Oman, M.E.: Iterative methods for total variation denoising. *SIAM Journal on Scientific Computing* **17**(1), 227–238 (1996)
13. Chambolle, A.: An algorithm for total variation minimization and applications. *Journal of Mathematical imaging and vision* **20**(1), 89–97 (2004)
14. Oh, S., Milstein, A.B., Bouman, C.A., Webb, K.J.: A general framework for nonlinear multigrid inversion. *IEEE Transactions on image Processing* **14**(1), 125–140 (2005)
15. Pursiainen, S.: Coarse-to-fine reconstruction in linear inverse problems with application to limited-angle computerized tomography. *Journal of Inverse and Ill-posed Problems* **16**(9), 873–886 (2008)
16. Zhao, S., Robelston, D., Wang, G., Whiting, B., Bae, K.T.: X-ray ct metal artifact reduction using wavelets: an application for imaging total hip prostheses. *IEEE transactions on medical imaging* **19**(12), 1238–1247 (2000)
17. Kingsbury, N.G.: The dual-tree complex wavelet transform: a new technique for shift invariance and directional filters. In: *Proc. 8th IEEE DSP Workshop*, vol. 8, p. 86 (1998). Utah
18. Kingsbury, N.: Image processing with complex wavelets. *Philosophical Transactions of the Royal Society of London A: Mathematical, Physical and Engineering Sciences* **357**(1760), 2543–2560 (1999)
19. Selesnick, I.W., Baraniuk, R.G., Kingsbury, N.C.: The dual-tree complex wavelet transform. *IEEE signal processing magazine* **22**(6), 123–151 (2005)
20. Thavavel, V., Murugesan, R.: Regularized computed tomography using complex wavelets. *International Journal of Magnetic Resonance Imaging* **1**(01), 027–032 (2007)
21. Pauwels, R., Araki, K., Siewersden, J., Thongvitmanee, S.: Technical aspects of dental cbct: state of the art. *Dentomaxillofacial Radiology* **44**(1), 20140224 (2014)
22. Pauwels, R., Beinsberger, J., Collaert, B., Theodorakou, C., Rogers, J., Walker, A., Cockmartin, L., Bosmans, H., Jacobs, R., Bogaerts, R., et al.: Effective dose range for dental cone beam computed tomography scanners. *European journal of radiology* **81**(2), 267–271 (2012)
23. Nemtoi, A., Czink, C., Haba, D., Gahléitner, A.: Cone beam ct: a current overview of devices. *Dentomaxillofacial Radiology* **42**(8), 20120443 (2013)
24. Nuyts, J., De Man, B., Fessler, J.A., Zbijewski, W., Beekman, F.J.: Modelling the physics in the iterative reconstruction for transmission computed tomography **58**(12), 63–96 (2013). doi:10.1088/0031-9155/58/12/R63
25. Zenóbio, M.A.F., Zenóbio, E.G., Silva, T.A., Nogueira, M.S.: Mass attenuation coefficients of x-rays in biological materials. In: *International Conference on Medical Physics and Biomedical Engineering*, Paris (2011)
26. Fessler, J.A.: Michigan Image Reconstruction Toolbox. <https://web.eecs.umich.edu/texttildelowlfessler/irt/irt/> Accessed 2018-04-24
27. Liu, Y., Ma, J., Fan, Y., Liang, Z.: Adaptive-weighted total variation minimization for sparse data toward low-dose x-ray computed tomography image reconstruction. *Physics in Medicine and Biology* **57**(23), 7923–7956 (2012). doi:10.1088/0031-9155/57/23/7923
28. Daubechies, I.: Ten Lectures on Wavelets. SIAM, ??? (1992)
29. Haar, A.: Zur theorie der orthogonalen funktionensysteme. *Mathematische Annalen* **69**(3), 331–371 (1910)
30. Du, L., Wen, Y., Ma, J.: Dual tree complex wavelet transform and bayesian estimation based denoising of poisson-corrupted x-ray images. In: *Proceedings of the 2013 International Conference on Intelligent Control and Information Processing*, ICICIP 2013, pp. 598–603. IEEE, ??? (2013). doi:10.1109/ICICIP.2013.6568145
31. Chan, T.F., Shen, J.: Image Processing and Analysis - Variational, PDE, Wavelet, and Stochastic Methods. SIAM, ??? (2005). doi:10.1137/1.9780898717877. <https://doi.org/10.1137/1.9780898717877>
32. Piana, M., Bertero, M.: Projected landweber method and preconditioning. *Inverse problems* **13**(2), 441 (1997)
33. Wang, Z., Bovik, A.C., Sheikh, H.R., Simoncelli, E.P.: Image Quality Assessment: From Error Visibility to Structural Similarity. *IEEE Transactions on Image Processing* **13**(4), 600–612 (2004). doi:10.1109/TIP.2003.819861
34. Fadili, J., Starck, J.-L.: Curvelets and ridgelets. In: *Computational Complexity*, pp. 754–773. Springer, ??? (2012)
35. Candes, E.J.: Ridgelets: theory and applications. PhD thesis, Stanford University Stanford (1998)
36. Starck, J.-L., Candes, E.J., Donoho, D.L.: The curvelet transform for image denoising. *IEEE Transactions on image processing* **11**(6), 670–684 (2002)

@settingslabel, options="nameyear"

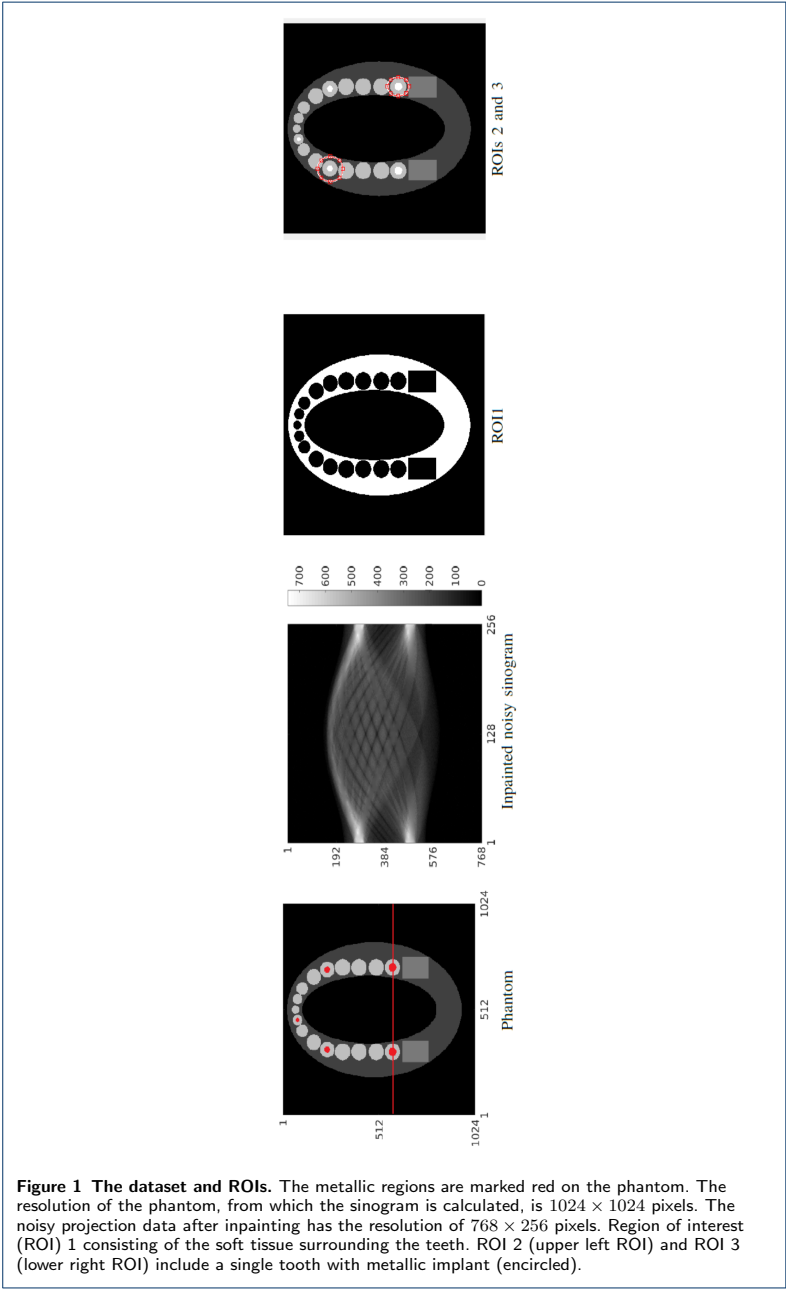
Figures

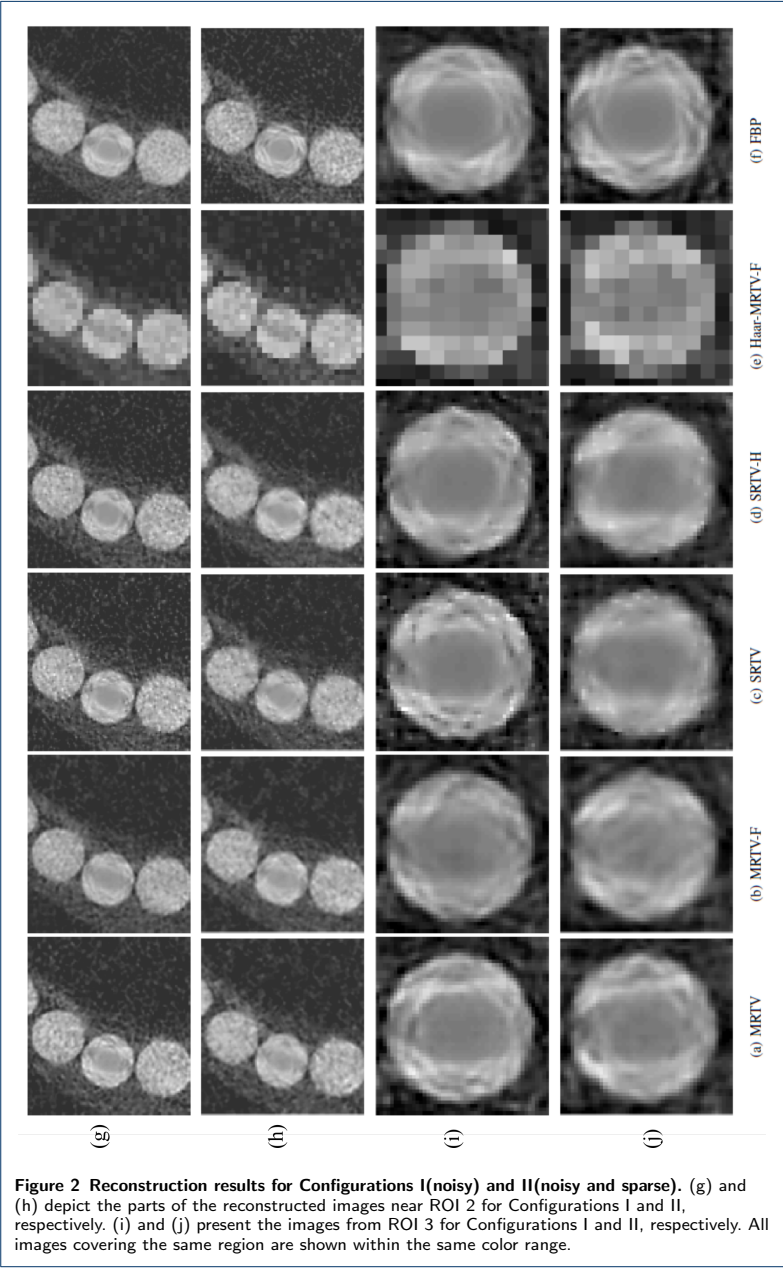
Additional Files

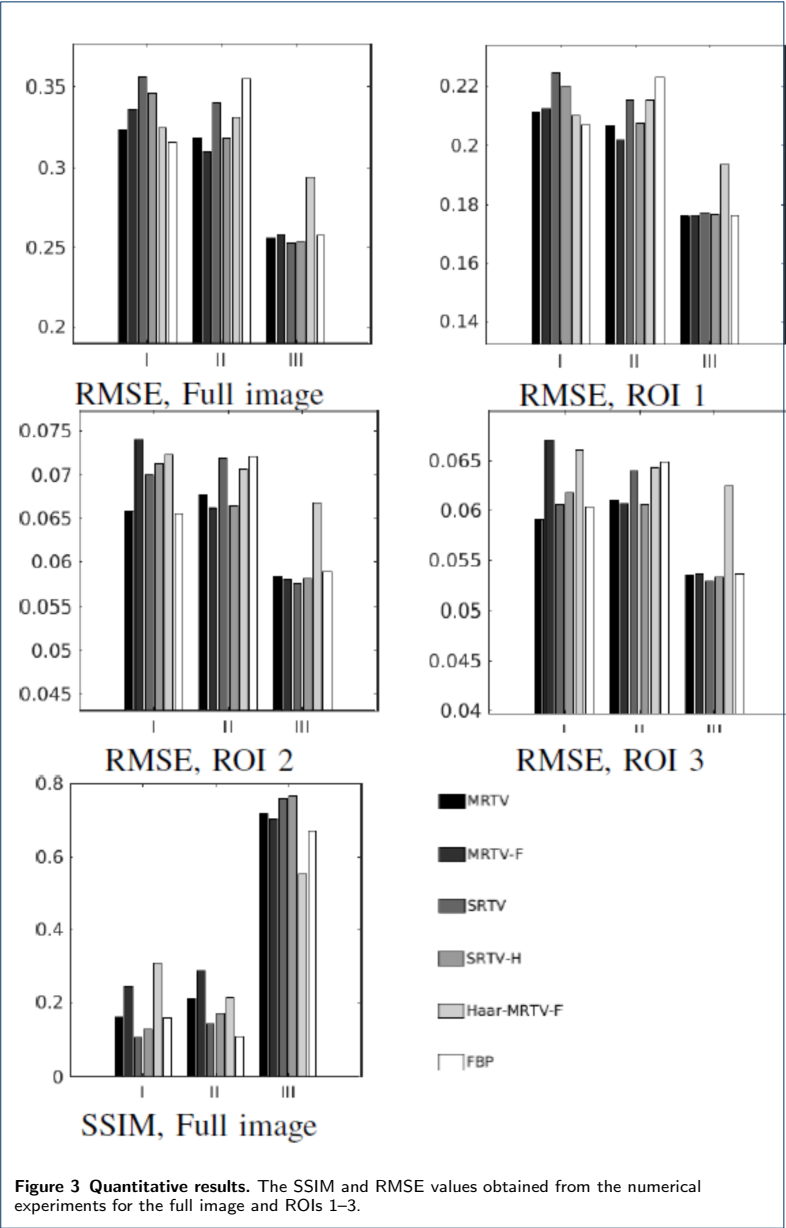
Additional file 1 — Multiresolution (Coarse-to-fine) Approach

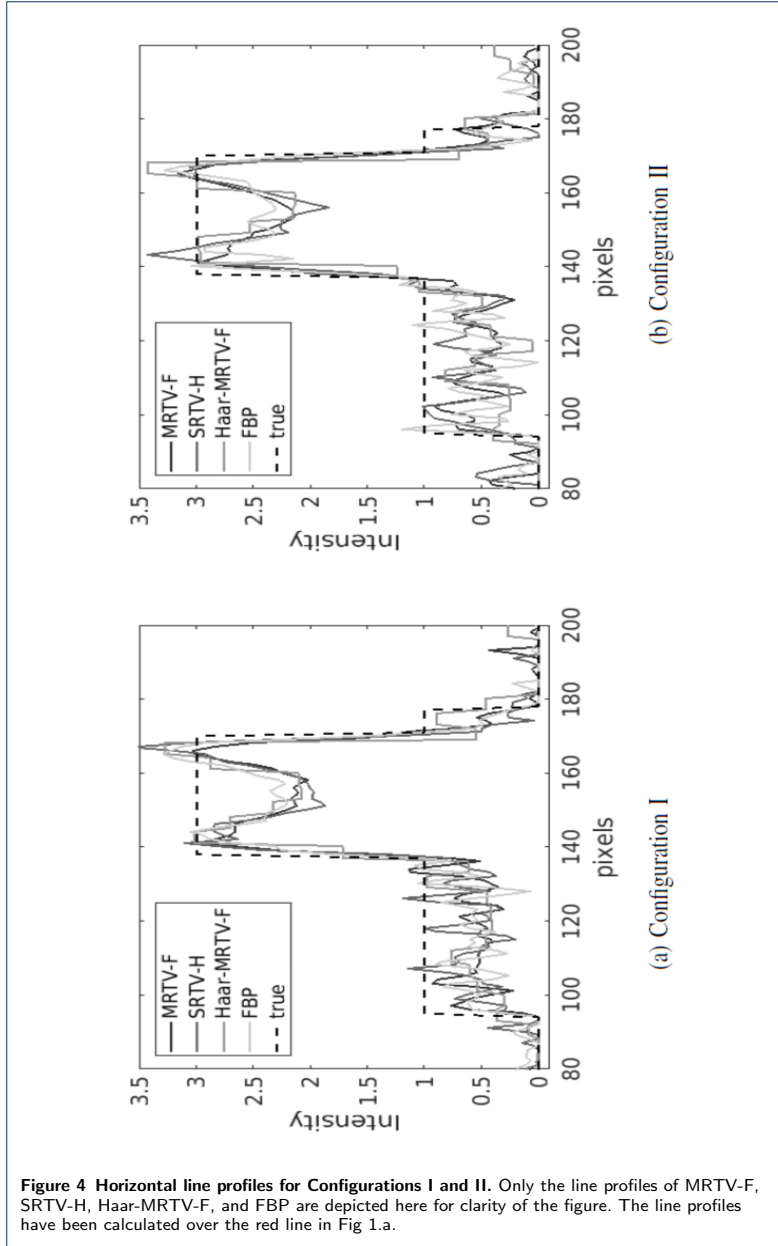
In the present multiresolution version of the TV regularization (see 7) the coarse details are reconstructed before the finer ones. We utilize the DT-CWT in this procedure via the projection matrices \mathcal{P}_ϕ and \mathcal{P}_ψ which multiplied with an image vector \mathbf{x} yield a coefficient vector for the low- and high-pass filter at a given resolution level. Furthermore, we define a filtered Radon matrix for the coarse and fine level as $\mathbf{L}_\phi = \mathbf{L}\mathcal{P}_\phi$ and $\mathbf{L}_\psi = \mathbf{L}\mathcal{P}_\psi$. Denoting $\mathbf{G}_\phi = (\mathbf{L}_\phi^T \mathbf{L}_\phi + \mathbf{D}_\phi \mathbf{\Gamma}_n \mathbf{D}_\phi)$ and $\mathbf{G}_\psi = (\mathbf{L}_\psi^T \mathbf{L}_\psi + \mathbf{D}_\psi \mathbf{\Gamma}_n \mathbf{D}_\psi)$, the inversion routine can be written as follows:

(1) Set the initial guess $\mathbf{x}_0 = (0, 0, \dots, 0)$.









(2) Find a coarse resolution estimate through

$$\mathbf{x}_{n+1}^{(\phi)} = \mathbf{G}_{\phi}^{-1} \mathbf{L}_{\phi}^T \mathbf{y} \quad (10)$$

with $\mathbf{\Gamma}_n = \text{diag}(|\mathbf{D}_\phi \mathbf{x}^{(\phi)}|)^{-1}$.

(3) Find a correction vector belonging to the finer resolution level as

$$\mathbf{x}_{n+1}^{(\psi)} = \mathbf{G}_\psi^{-1} \mathbf{L}_\psi^T (\mathbf{y} - \mathbf{L}_\phi \mathbf{x}_{n+1}^{(\phi)}) \quad (11)$$

with $\mathbf{\Gamma}_n = \text{diag}(|\mathbf{D}_\psi \mathbf{x}_n^{(\psi)}|)^{-1}$.

(4) Set $\mathbf{x}_{n+1} = \mathbf{x}_{n+1}^{(\phi)} + \mathbf{x}_{n+1}^{(\psi)}$ and $n \rightarrow n + 1$.

(5) If n is smaller than the desired number of iterations, then repeat the steps (2)–(5).

If more than two nested meshes are used, then the correction step (2) can go through multiple resolution levels

$\psi_1, \psi_2, \dots, \psi_{n_f}$ via the recursive process:

$$\begin{aligned} \mathbf{x}_{n+1}^{(\psi_i)} &= \mathbf{G}_{\psi_i}^{-1} \mathbf{L}_{\psi_i}^T (\mathbf{y} - \mathbf{L}_c \mathbf{x}_{n+1}^{(c)} \\ &\quad - \sum_{k=1}^{i-1} \mathbf{L}_{\psi_k} \mathbf{x}_{n+1}^{(\psi_k)}) \end{aligned} \quad (12)$$

with $\mathbf{\Gamma}_n = \text{diag}(|\mathbf{D}_{\psi_i} \mathbf{x}_n^{(\psi_i)}|)^{-1}$ for $i = 1, 2, \dots, n_f$.

